

Old Dominion University

**ODU Digital Commons**

---

Biomedical Engineering Theses & Dissertations

Biomedical Engineering

---

Fall 2023

# Investigation of Nanosecond Pulsed Electric Fields (nsPEF) Induced Anti-Cancer Mechanism and Enhanced B16f10 Melanoma Cancer Treatment

Kamal Asadipour

*Old Dominion University, [kasad001@odu.edu](mailto:kasad001@odu.edu)*

Follow this and additional works at: [https://digitalcommons.odu.edu/biomedengineering\\_etds](https://digitalcommons.odu.edu/biomedengineering_etds)



Part of the [Biomedical Engineering and Bioengineering Commons](#), [Nanoscience and Nanotechnology Commons](#), and the [Oncology Commons](#)

---

## Recommended Citation

Asadipour, Kamal. "Investigation of Nanosecond Pulsed Electric Fields (nsPEF) Induced Anti-Cancer Mechanism and Enhanced B16f10 Melanoma Cancer Treatment" (2023). Doctor of Philosophy (PhD), Dissertation, Electrical & Computer Engineering, Old Dominion University, DOI: 10.25777/4pkt-x643 [https://digitalcommons.odu.edu/biomedengineering\\_etds/28](https://digitalcommons.odu.edu/biomedengineering_etds/28)

This Dissertation is brought to you for free and open access by the Biomedical Engineering at ODU Digital Commons. It has been accepted for inclusion in Biomedical Engineering Theses & Dissertations by an authorized administrator of ODU Digital Commons. For more information, please contact [digitalcommons@odu.edu](mailto:digitalcommons@odu.edu).

**INVESTIGATION OF NANOSECOND PULSED ELECTRIC FIELDS (NSPEF)  
INDUCED ANTI-CANCER MECHANISM AND ENHANCED B16F10 MELANOMA  
CANCER TREATMENT**

by

Kamal Asadipour B.S. May 2013, Islamic Azad University  
M.S. May 2016, Semnan University

A Dissertation Submitted to the Faculty of  
Old Dominion University in Partial Fulfillment of the  
Requirements for the Degree of

**DOCTOR OF PHILOSOPHY**

**BIOMEDICAL ENGINEERING**

**OLD DOMINION UNIVERSITY**  
December 2023

Approved by:

Shu Xiao (Director)

Stephen J. Beebe (Member)

P Thomas Vernier (Member)

Chunqi Jiang (Member)

Siqi Guo (Member)

## ABSTRACT

### INVESTIGATION OF NANOSECOND PULSED ELECTRIC FIELDS (NSPEF) INDUCED ANTI-CANCER MECHANISM AND ENHANCED B16F10 MELANOMA CANCER TREATMENT

Kamal Asadipour, Old Dominion University, 2023 Director: Dr. Shu Xiao

The use of nanosecond pulsed electric fields (nsPEF) has emerged as a promising area of research with vast implications across various scientific disciplines. The ability to generate ultra-short, high-voltage electric pulses has paved the way for numerous applications, ranging from fundamental investigations of biological phenomena to the development of innovative medical therapies. The aim of this thesis is to highlight the importance of nsPEF in two critical areas: 1) Understanding the impact of subtle postpulse waveforms through a comprehensive analysis of two common pulse generators and 2) using this knowledge to advance melanoma treatment by enhancing the therapeutic effect of nsPEF with the addition of carbon nanotubes (CNTs).

The first part of our study concentrates on comprehending the nuances and differences between two widely utilized pulser generators: the Blumlein line (BL) and the Pulse Forming Line (PFL). Through the investigation of the pulse waveform via the adjustment of the primary pulses in these pulse generators, it was revealed that the post-pulse waveforms possess the capacity to modify cellular reactions and, in some cases, induce distinct cellular responses due to variations in post-pulse characteristics between the two designs. The post-pulse of the BL design exhibited a relatively extended duration, approximately 50  $\mu\text{s}$  (for 40 kV/cm, 100 ns), and had an opposite polarity compared to the main pulse. Conversely, the PFL's post-pulse was considerably shorter, around 2  $\mu\text{s}$ , and shared the same polarity as the main pulse. For the PFL, the LD50 and the thresholds for the dissipation of mitochondrial membrane potential, and an increase in plasma membrane PI permeability and a decrease in trans plasma membrane electron transport (tPMET)

were observed at lower pulse numbers compared to the BL design. Furthermore, only the PFL induced an increase in tPMET, thus producing a biphasic effect. However, both pulser designs exhibited similar pulse numbers for generating of mitochondrial reactive oxygen species (ROS). Notably, the PFL reduced spare respiratory capacity (SRC) significantly, while the BL increased SRC. These findings represent a pioneering revelation that the conditions resulting from low-intensity post-pulse charging have a substantial impact on cellular responses, with the potential to selectively induce specific cellular responses. It also underscores the importance of considering these post-pulse factors when comparing results obtained from other pulse waveforms.

However, while the PFL exhibits more robust responses than the BL generator, it is important to acknowledge a limitation in applying of the PFL pulse generator for *in vivo* studies, as it necessitates higher voltage levels when compared to the BL pulse generator. This increased voltage requirement raises clinical concerns that warrant careful clinical consideration. The second part of this thesis is dedicated to take advantage of multi-walled carbon nanotubes (MWCNT) to enhance the tumor ablation *in vivo*. MWCNT significantly reduced the necessary pulse conditions for *in vitro* tumor ablation, lowering it from 0.009 Vs/cm to 0.005 Vs/cm. *In vivo*, the required pulses were reduced from 1000 to 500, marking at least a twofold improvement. The combined impact of MWCNT to nsPEF treatment for melanoma, using the B16f10 melanoma cell line as an *in vitro* and *in vivo* model, has the potential to expand the applications of the PFL pulser in future *in vivo* studies focused on melanoma immune therapy, with the goal of achieving tumor ablation with *in-situ* vaccination (ISV) against the threatened cancer. Ultimately, this study may pave the way for the translation of this combination approach

into preclinical and clinical settings, potentially revolutionizing the management of this devastating disease.

Copyright, 2023, by Kamal Asadipour, All Rights Reserved.

I dedicate this dissertation to all those with a passion for the field of bioelectrics and to those who aspire to make a difference through their knowledge and curiosity. May this work inspire and provide valuable insights, lighting the way for future scholars and enthusiasts on their own journeys of discovery.

## ACKNOWLEDGMENTS

I wish to extend my sincere gratitude to the committee members who have played an integral role in the successful completion of this dissertation. I am deeply appreciative of my advisors, Dr. Stephen Beebe and Dr. Shu Xiao, for their unwavering support, expert guidance, and invaluable insights that have guided me throughout this research journey. Special thanks are also due to Dr. Vernier and Dr. Guo for their generous assistance and encouragement. Additionally, I would like to express my thanks to my colleagues, Carol Zhou and Vincent Yi, for their collaboration and willingness to share their experiences and insights, which greatly enriched the depth of this work. This dissertation is the result of collective efforts, and I am genuinely thankful for the assistance and motivation I received along the way.

**NOMENCLATURE**

|            |  |
|------------|--|
| ANOVA      | Analysis of Variance                                 |
| <i>ATP</i> | Adenosine Triphosphate                               |
| BL         | Blumlein   |
| BMDC       | Bone Marrow-derived DCs                              |
| CCK-8      | Cell Counting Kit 8                                  |
| CNT        | Carbon Nanotube                                      |
| COOH       | Carboxylic Acid                                      |
| DC         | Dendritic Cell                                       |
| DMEM       | Dulbecco's Modified Eagle Medium                     |
| DNA        | Deoxyribonucleic Acid                                |
| DPBS       | Dulbecco's Phosphate-Buffered Saline                 |
| E          | Electric Field                                       |
| EDTA       | Ethylenediaminetetraacetic Acid                      |
| EF         | Electric Field                                       |
| EP         | Electroporation                                      |
| ET         | Electron Transport                                   |
| ETC        | Electron Transport Chain                             |
| FBS        | Fetal Bovine Serum                                   |
| FC         | Flow Cytometry                                       |
| FCCP       | Carbonyl Cyanide p-trifluoro-methoxyphenyl Hydrazone |
| FITC       | Fluorescein Isothiocyanate                           |

|        |   |
|--------|---|
| IACUC  | Institutional Animal Care & Use Committee         |
| IC50   | Half-maximal Inhibitory Concentration             |
| ICD    | Induced Cell Death                                |
| IFN    | Interferon  |
| IL     | Interleukin                                       |
| IMM    | Inner Mitochondrial Membrane                      |
| IMP    | Integral Membrane Proteins                        |
| ISV    | In-Situ Vaccination                               |
| L      | Length  |
| MHC    | Major Histocompatibility Complex                  |
| MOSFET | Metal-Oxide-Semiconductor Field-Effect Transistor |
| MSOX   | Mitochondrial Superoxide Indicators               |
| MWCNT  | Multi-walled Carbon Nanotube                      |
| NAD    | Nicotinamide Adenine Dinucleotide                 |
| NADP   | Nicotinamide Adenine Dinucleotide phosphate       |
| NPS    | Nano Pulse Stimulation                            |
| nsPEFs | Nanosecond pulsed electric fields                 |
| OCR    | Oxygen Consumption Rate                           |
| OMP    | Outer Membrane Proteins                           |
| PBS    | Phosphate Buffered Saline                         |
| PEF    | Pulse Electric Field                              |
| PEG    | Polyethylene Glycol                               |
| PFL    | Pulse Forming Line                                |

|                |  |
|----------------|--|
| PI             | Propidium Iodide                               |
| PM             | Plasma Membrane                                |
| PMET           | Plasma Membrane Electron Transport             |
| PMRS           | Plasma Membrane Redox System                   |
| PTP            | Mitochondrial Permeability Transition Pore     |
| RCF            | Relative Centrifugal Field                     |
| RNA            | Ribonucleic Acid                               |
| ROS            | Reactive Oxygen Species                        |
| SEM            | Scanning Electron Microscope                   |
| SRC            | Spare Respiratory Capacity                     |
| SWCNT          | Single-walled Carbon Nanotube                  |
| TEM            | Transmission Electron Microscope               |
| TGA            | Thermogravimetric Analysis                     |
| TMRE           | Tetramethylrhodamine, Ethyl Ester, Perchlorate |
| UV             | Ultraviolet                                    |
| WST            | Water-Soluble Tetrazolium Salt                 |
| Z0             | impedance                                      |
| $\Delta\Psi_m$ | Mitochondrial Membrane Potential               |

## TABLE OF CONTENTS

|   |     |
|---|-----|
| LIST OF FIGURES .....   | XII |
| LIST OF TABLES .....  | XIV |
| LIST OF EQUATIONS .....   | XV  |
| CHAPTER 1 : INTRODUCTION .....  | 1   |
| 1.1 In vitro studies of cell responses to nanosecond pulsed electric fields .....                                       | 1   |
| 1.2 In vivo studies with nanosecond pulsed electric fields .....  | 4   |
| CHAPTER 2 : ULTRA-LOW INTENSITY POST-PULSE AFFECTS CELLULAR<br>RESPONSES CAUSED BY NANOSECOND PULSED ELECTRIC FIELDS .. | 8   |
| 2.1 Introduction .....  | 8   |
| 2.2 Background and Significance.....  | 9   |
| 2.2.1 The Use of Electrical Pulses in Medicine .....  | 9   |
| 2.2.2 Nano Pulse Electrical Treatment.....  | 10  |
| 2.2.3 Electrical Pulsing Parameters .....   | 11  |
| 2.2.4 Rise–fall Times .....   | 12  |
| 2.2.5 Monopolar and Bipolar Pulses .....  | 14  |
| 2.2.6 Significance .....  | 15  |
| 2.3 Material and Methods.....   | 16  |
| 2.3.1 Pulse Generators and Cell Exposure System .....   | 16  |
| 2.3.2 Cell Culture .....  | 17  |
| 2.3.3 tPMET Rate Determination.....   | 17  |

|        |  |    |
|--------|--|----|
| 2.3.4  | Cell Viability Analysis .....  | 18 |
| 2.3.5  | Live Cell Imaging.....   | 18 |
| 2.3.6  | Flow Cytometry.....  | 18 |
| 2.3.7  | Seahorse Assay.....  | 19 |
| 2.3.8  | Statistics Analysis .....  | 20 |
| 2.4    | Results .....  | 20 |
| 2.4.1  | Two pulse generators with the same 100 ns primary pulse result in low-intensity post-pulses with the BL waveform longer and with opposite polarity to the primary pulse and the PFL waveform shorter and with the same polarity to the primary pulse ..... | 20 |
| 2.4.2  | PFL Pulses Extended the Duration of OMP and Posed Less Change on IMP than BL Pulses .....  | 26 |
| 2.4.3  | Effects of PFL and BL Pulsers on Cellular Plasma Membrane Responses ..   | 28 |
| 2.4.4  | <i>PFL has a lower IC 50 for cell death induction than BL</i> .....  | 30 |
| 2.4.5  | Biphasic effects of nsPEFs on tPMET in cancerous and non-cancerous cells   | 31 |
| 2.4.6  | PFL induce different effects on tPMET activity and cell viability in cancerous and non-cancerous cells.....  | 33 |
| 2.4.7  | Determining best timing after nsPEF to measure $\Delta\Psi_m$ and ROS production   | 35 |
| 2.4.8  | Differential loss of $\Delta\Psi_m$ with increases in mROS production with the PFL and the BL pulsers .....  | 37 |
| 2.4.9  | PFL but Not BL Caused a Decrease in Maximal OCR and Spare Respiratory Capacity (SRC).....  | 38 |
| 2.4.10 | Effect of an antioxidant Trolox on nsPEFs-induced loss of $\Delta\Psi_m$ and increases in ROS .....  | 40 |

|   |  |           |
|---|--|-----------|
| 2.4.11  | NsPEFs and Rotenone act synergistically for ROS production indicating distinct sites of action in the ETC..... | 42        |
| 2.5   | Discussion .....   | 44        |
| 2.6   | Conclusions .....  | 53        |
| <b>CHAPTER 3 : ENHANCEMENT OF NANO-SECOND PULSE ELECTRIC FIELDS</b> |  |           |
| <b>(NSPEFS) ON TREATMENT OF MURINE MELANOMA WITH MULTIWALLED</b>    |  |           |
| <b>CARBON NANOTUBES (CNTS).....</b>                                 |  |           |
|   |  | <b>55</b> |
| 3.1   | Introduction .....   | 55        |
| 3.2   | Backgrounds and significance.....  | 58        |
| 3.2.1   | Carbon nanotubes (CNTs).....   | 58        |
| 3.2.2   | Cellular Uptake Mechanisms of CNTs .....   | 59        |
| 3.2.3   | Effect of chemical functionalization on CNTs.....  | 61        |
| 3.2.4   | Biocompatibility of CNTs with immune cells .....   | 63        |
| 3.2.5   | CNTs' biodistribution .....  | 65        |
| 3.2.6   | Significance.....  | 67        |
| 3.3   | Materials and Methods .....  | 68        |
| 3.3.1   | SEM and TEM .....  | 68        |
| 3.3.2   | Thermogravimetric Analysis (TGA).....  | 68        |
| 3.3.3   | Cell culture .....   | 69        |
| 3.3.4   | Pulsed electric field exposure methods .....   | 69        |
| 3.3.5   | Determination of Toxicity of MWCNTs.....   | 70        |
| 3.3.6   | Cell viability analysis .....  | 70        |
| 3.3.7   | Apoptosis.....   | 71        |

|        |   |     |
|--------|---|-----|
| 3.3.8  | Conductivity .....  | 71  |
| 3.3.9  | Murine tumor model and treatment procedure.....   | 71  |
| 3.3.10 | Statistics analysis.....  | 72  |
| 3.4    | Results and Discussion .....  | 74  |
| 3.4.1  | Material Characterization .....   | 74  |
| 3.4.2  | In Vitro .....  | 78  |
| 3.4.3  | <i>Dose-dependent relationship between the concentration of MWCNT and viability</i><br>78                     |     |
| 3.4.4  | Enhancement of nsPEF in combination with MWCNT on Cell Viability ....   | 80  |
| 3.4.5  | MWCNT increased the conductivity.....   | 81  |
| 3.4.6  | Lack of Apoptotic Induction on B16F10 Cells by MWCNT, nsPEFs, or Their<br>Combination .....                   | 85  |
| 3.4.7  | In Vivo.....  | 86  |
| 3.4.8  | MWCNTs Demonstrate No Impact on Tumor Growth Rate .....   | 86  |
| 3.4.9  | Efficient Pulsing with MWCNT: Achieving a 50% Reduction in Pulsing<br>Requirements for Tumor Elimination..... | 87  |
| 3.4.10 | Lacking ISV after challenge.....  | 89  |
| 3.5    | Conclusion.....   | 91  |
|        | CHAPTER 4 : DISCUSSIONS .....   | 92  |
| 4.1    | In vitro studies of cell responses to nanosecond pulsed electric fields .....                                 | 92  |
| 4.2    | In vivo studies with nanosecond pulsed electric fields .....  | 94  |
|        | CHAPTER 5 : CONCLUSIONS .....   | 100 |
|        | REFERENCES .....  | 102 |

APPENDIX..... 111

## LIST OF FIGURES

|  |    |
|--|----|
| Figure 1. The waveforms were generated using two pulse generators. ....  | 22 |
| Figure 2. The pulse waveforms were analyzed in both the time and frequency domains. ....   | 24 |
| Figure 3. The spectrums of the pulses over time were calculated for the PFL and BL waveforms<br>using STFT performed on the data shown in Figure 1b. ....                    | 25 |
| Figure 4. The potential drops were simulated using a linear equivalent cell model by applying a<br>clean pulse (CP), a PFL pulse, and a BL pulse at 1 $\mu$ s. ....          | 27 |
| Figure 5. nsPEF effects of BL and PFL pulsers on tPMET and PI uptake. ....   | 29 |
| Figure 6. nsPEF effects of BL and PFL pulsers cell viability. ....   | 30 |
| Figure 7. tPMET rates of H9c2 non-cancer cardiac myoblasts and 4T1-luc mammary cancer<br>cells. ....   | 32 |
| Figure 8. Relationships between H9c2 cells and 4T1-luc cells among tPMET rates, and viability.<br>.....  | 34 |
| Figure 9. A 20-minute interval is an appropriate duration for capturing alterations in<br>mitochondrial membrane potential and the presence of reactive oxygen species. .... | 36 |
| Figure 10. nsPEF effects of BL and PFL pulsers on the reactive oxygen species and mitochondria<br>membrane potential at 20 min after pulsing. ....                           | 38 |
| Figure 11. nsPEF effects of BL and PFL pulsers on mitochondrial oxidative metabolism in<br>B16F10 melanoma cell lines. ....  | 39 |
| Figure 12. The independence of mitochondrial membrane potential and ROS dynamics in<br>response to nsPEF exposure. ....  | 41 |
| Figure 13. Synergistic ROS Generation by Rotenone and nsPEFs Reveals Distinct Sites of<br>Action in Mitochondrial Electron Transport Chain Complex I. ....                   | 43 |

|   |    |
|---|----|
| Figure 14. The timeline of the cell responses to PFL and BL pulses at different time intervals:<br>10-50 mins, 15 hours, and 24 hours after pulsing ..... | 45 |
| Figure 15. SEM images of the surface morphology of MWCNT which poured on carbon tape.<br>.....  | 75 |
| Figure 16. MTEM images of the MWCNT on grid with formvar film. ....   | 76 |
| Figure 17. Thermogravimetric analysis (TGA) of MWCNT from room temperature to 800 °C<br>with a heating rate of 5 °C/min. ....                             | 77 |
| Figure 18. Effects of different concentrations of MWCNTs on cell viability test (CCK-8 assay)<br>after 24 hours. ....                                     | 79 |
| Figure 19. Effects of different electric fields in present and absent of MWCNTs (200 µg/ml) on<br>cell viability test (CCK-8 assay) after 24 hours. ....  | 80 |
| Figure 20. Conductivity of cell culture media before and after adding different concentration of<br>MWCNT. ....   | 82 |
| Figure 21. MWCNT effect on cell viability (CCK-8 assay) after 24 hours, when added before<br>and after pulsing. ....                                      | 84 |
| Figure 22. nsPEF not triggers apoptotic cell death in B16F10 cells in present or absence of<br>MWCNT. ....  | 85 |
| Figure 23. A) Schematic of in vivo experiment. ....   | 86 |
| Figure 24. B16-F10 model primary tumor growth curves for nsPEF groups. ....   | 88 |
| Figure 25. B16-F10 model challenged tumor growth curves for nsPEF groups. ....  | 90 |

**LIST OF TABLES**

|   |    |
|---|----|
| Table 1. Calculated nsPEFs, IC-50 in present (Right) and absent (Left) of MWCNT. .... | 81 |
|---|----|

**LIST OF EQUATIONS**

|  |    |
|--|----|
| Equation 1: Charging Effect .....                                  | 69 |
| Equation 2: The electric field strength at the tip of the CNT..... | 82 |

## CHAPTER 1:

### Introduction

#### 1.1 In vitro studies of cell responses to nanosecond pulsed electric fields

The application of nanosecond pulsed electric fields (nsPEFs) in biological and medical contexts relies on pulsed power technology. Pulsed power involves the gathering and retention of electrical energy, followed by its swift discharge in brief intervals. This process enhances instantaneous high power without inducing heat. Pulsed power technology has a longstanding history in engineering applications, including high-power lasers, particle accelerators, radar and communication systems, and high-voltage and power electronics [1]. The utilization of pulsed power extends beyond traditional physics, opening up novel possibilities for its application in the realms of biology and medicine [2]. The uniqueness of pulsed power in the nanosecond domain became clear when it was shown that these ultra-short pulses can have effects on the cell interior, which is absent with microsecond pulses [3] such that microsecond pulses go around the cell and nanosecond pulses go through the cell [4].

In recent years, there have been noteworthy advancements in the field of bioelectrics, particularly in the exploration of nanosecond pulsed power technology and its impacts on cellular responses [5-7]. High-intensity nanosecond pulses have demonstrated the ability to elicit a wide range of biological responses, including unique plasma membrane permeabilization [8], dissipation of the mitochondrial membrane potential ( $\Delta\Psi_m$ ) [9, 10], DNA damage [11], and the activation of signaling pathways [12, 13]. NsPEFs have emerged as a promising tool with

numerous applications in the field of biomedicine. These applications encompass tissue treatment [14, 15], atrium ablation for heart defibrillation [16, 17], and stimulating immune responses for cancer treatment [18-21].

For a clearer grasp of pulsed power, envision a joule of energy being accumulated and discharged within brief time intervals. When a joule of energy is stored and released over one second, it yields 1 watt of power. However, if this energy is released within a microsecond, it generates a megawatt of power, and if released within a nanosecond, it results in a gigawatt of power. In our investigations, nanosecond pulses typically last around 100 ns, delivering approximately 10 megawatts per pulse [2].

The impact of the electrical pulse shape or waveform has been the subject of numerous studies [22-25], which can categorize these studies into three distinct groups. **(1) Electrical pulsing parameters:** These studies investigate the effects of main parameters, including the pulsed electric field (E), pulse duration ( $\tau$ ), and pulse number (n). These studies suggest that the crucial determinant for nanosecond pulse effects is the total number of ions that traverse the cell membrane. In simpler terms, the magnitude of biological effects depends on the product of current density (which, in the case of constant conductivity, is directly proportional to electric field intensity as per Ohm's law) and the pulse duration [5]. **(2) Rise-fall times:** Previous studies assumed that the pulse shape has an ideal rectangular form, however, there are subtleties in pulse waveforms, including features like rise time and fall time, which also play a role [9, 26]. The significance of the rise and fall times in nsPEF was demonstrated by comparing 600 nanosecond pulses with fast rise and fall times (15 ns) to those with slow rise and fall times (150 ns). The faster rise and fall times had more pronounced effects in dissipating the mitochondrial membrane potential ( $\Delta\Psi_m$ ) and inducing cell death (CD) compared to the slower rise and fall times [9, 27].

**(3) Monopolar and Bipolar Pulses:** Bipolar pulses, which have an additional pulse with an opposite polarity, have been investigated as a method to improve permeabilization of the cell membrane by efficiently porating both sides of the cell in microsecond pulsing duration. However, research involving much shorter pulses (300 and 600 ns) found that bipolar pulses were less effective at electro-permeabilization [28, 29]. They were also not as proficient at increasing intracellular calcium concentration. This was described as nanosecond bipolar cancellation (NBC) which can disrupt the charging of cell membranes by the opposite current before any damage to the cell occurs. However, this is just one possible hypothesis, and other mechanisms might also be valid [28].

It's important to note that most of these studies primarily focused on the main pulse and often overlooked observations during the interpulse interval. due to an oscilloscope small scale which adjusted for the main pulse. This oversight was attributed to the small scale of the oscilloscope, primarily adjusted for the main pulse. We call that post-pulse and typically generates a voltage across the tissue or cell medium that is approximately ten times weaker than the main pulse. Nevertheless, biological responses are often attributed solely to the main pulse.

Chapter One introduces a pioneering investigation into the impact of post-pulses on biological responses triggered by nanosecond pulses, representing the first-ever examination of this subject as our best knowledge. Two common pulse generators We employed based on transmission lines, specifically a pulse forming line (PFL) and a Blumlein line (BL), to illustrate the distinct characteristics of these post-pulses while maintaining nearly identical frequencies and voltages. It's noteworthy that PFL and BL continue to be robust pulse generators for in vitro applications that demand high current, low impedance, and short pulse durations (less than or equal to 100 nanoseconds), despite the increasing use of solid-state pulse generators [30].

Understanding how nsPEFs interact with ultra-low-intensity post-pulses is critical for advancing the applications of pulse power technologies across various fields. These findings could have implications for enhancing therapeutic strategies, such as tumor ablation, atrium ablation for heart defibrillation, and for eliciting immune responses in cancer treatment. Furthermore, delving into the underlying mechanisms can provide valuable insights into the fundamental principles governing cellular responses to pulsed electric fields. The studies herein underscore the importance of characterizing and reporting pulse waveforms to enhance the reproducibility and comparability of results among different research groups employing diverse generators. In addition, given that nsPEFs have been shown to modulate electron transport [31], it is important to explore the possibilities for less well characterized non-lethal effects that mimic physiological and pathological mechanisms for cell signaling with oxidants such as reactive oxygen species (ROS), which are natural intracellular physiological signaling molecules [32].

## **1.2 In vivo studies with nanosecond pulsed electric fields**

In the second chapter, efforts are made to address a limitation in translating the in vitro results from the first chapter to an in vivo context. In the conclusion of the first chapter, cells exhibited greater sensitivity to the PFL than the BL pulser with lower pulse numbers or electric field intensities of 40 kV/cm for inducing cell membrane permeability (Figure 5), dissipation of  $\Delta\Psi_m$  (Figure 10), a decrease in mitochondrial SRC (Figure 11), a biphasic effect on tPMET (Figure 5, and Figure 7), and eventual cell death (Figure 6). These distinct post-pulse waveforms were determined from their primary waveforms, which PFL has a post-pulse waveform with the same polarity as the primary pulse and the BL pulses has a post-pulse waveform with an opposite polarity as the primary pulse. The outcomes establish the PFL pulser as a more promising

candidate for in vivo cancer ablation, with might enhance the potential to achieve in situ vaccination.

In studies conducted by Lassiter et al [33] on an orthotopic rat liver cancer model and by Guo et al [34] and Beebe et al [35] on an orthotopic mouse breast cancer model, rodents that remained tumor-free exhibited a vaccine effect akin to in situ vaccination following nsPEF treatment. This effect was evidenced when, 7 weeks after nsPEF treatment, the rodents were re-challenged with tumor cell injections, resulting in the rejection of tumor cells and the absence of tumor growth. The specific immune phenotypes conducive to these in situ vaccinations were identified in both models. Generally, the immunosuppressive tumor environment (TME) was eradicated, leading to the presence of active CD8+ and CD4+ effector memory and central memory T-cells [36-38], as well as natural killer cells (NKs) in the liver model, although to a lesser extent in the breast cancer model. However, not all nsPEF-treated cancer models demonstrated this in situ vaccination response. For instance, in the ectopic mouse melanoma model studied by Rossi et al [39], only a few animals exhibited tumor rejection as a vaccine effect. A notable challenge identified in these cases was the persistent or return of the presence of immunosuppression in the TME [38], as highlighted by Guo et al. in the ectopic pancreatic model [36].

It seems that there are two distinct thresholds or types of targets that need activation to achieve tumor-free animals on one hand and tumor-free animals with an in situ vaccination effect on the other. The hypothesis suggests that the vaccine effect is attributed to an "optimal" form of nanosecond pulsed electric field (nsPEF)-induced regulated cell death (RCD), specifically one that is considered immunogenic. It is important to note that the RCD mechanisms for both in situ vaccination models are unknown, except that they do not involve apoptosis. This type of RCD

allows dendritic cells (DCs) to effectively detect cancer antigens and present them to T-cells through cross-presentation, as proposed by Galluzzi et al [40]. Given our demonstration of the PFL's ability to induce distinct cellular responses, exploring its potential for in vivo studies becomes a valuable avenue for further investigation. In most of our in vivo studies, nanosecond pulses include around 100 ns durations, 1000 pulses at 50 kV/cm, can be safely eliminated a tumor. These conditions render the PFL less practical due to its half-charging voltage output, thereby raising safety concerns. Consequently, to overcome this limitation, we opted for an alternative pulser (BL), and integrated it with carbon nanotubes (CNTs). This combination assumed to enhances the nanosecond pulsed electric field (nsPEF) and offers potential benefits for future studies by enabling the use of lower nsPEF conditions while harnessing the advantages of the PFL pulser.

Multi-walled carbon nanotubes (MWCNTs), a novel type of carbon material, have demonstrated field emission capabilities, which have opened up a wide range of potential applications due to their high aspect ratio and excellent conductivity [41]. Due to the high aspect ratio and excellent electrical conductivity of CNTs [38], they can enhance the local field strength (Figure 19) [42]. When a CNTs are inserted into a region of uniform electric field, it generates a phenomenon known as the "lightning rod" effect, where an intensified electric field is formed at the tip of the CNT which is proportional to the CNT aspect ratio [43]. Additionally, the ability of CNTs to penetrate the cell membrane, resembling nano-needles, could be explained by a theoretical nanosyringe mechanism simulated by Lopez et al. for nanotube insertion into the lipid bilayer [44]. Molecular dynamics studies by Lopez and colleagues demonstrated that a hydrophobic nanotube with hydrophilic tips initially adsorbs horizontally onto a model membrane. Subsequently, the nanotube spontaneously changes its orientation from horizontal to

vertical alignment, forming a transmembrane pore-like orientation through the bilayer. This hypothesis suggests that it may also enhance the poration of the cell membrane followed by nsPEF.

Given these promising properties, MWCNTs were employed to enhance the effects of nsPEF in a B16F10 melanoma cancer model. The objective of this study was to investigate the combined effects of MWCNT when used in conjunction with nsPEF treatment for melanoma. The study employed the B16F10 melanoma cell line as an in vitro and in vivo model. The ultimate goal is to expand the scope of these findings and create potential applications for the PFL pulse generator in future in vivo studies. The aim is to reduce the required electric field strength through the incorporation of MWCNTs and develop innovative and effective strategies for melanoma immune therapy, with the ultimate objective of in-situ vaccination (ISV). Ultimately, this research may pave the way for the translation of this combined approach into preclinical and clinical settings, potentially revolutionizing the management of this devastating disease.

## CHAPTER 2:

# Ultra-Low Intensity Post-Pulse Affects Cellular Responses Caused by Nanosecond Pulsed Electric Fields <sup>1</sup>

## 2.1 Introduction

In recent years, there have been noteworthy advancements in the field of bioelectrics, particularly in the exploration of nanosecond pulsed power technology and its impacts on cellular responses [5-7]. High-intensity nanosecond pulses have demonstrated the ability to elicit a wide range of biological responses, including membrane permeabilization [8], DNA damage, and the activation of signaling pathways [12, 13]. NsPEFs have emerged as a promising tool with numerous applications in the field of biomedicine. These applications encompass tissue treatment [14, 15], atrium ablation for heart defibrillation [16, 17], and stimulating immune responses for cancer treatment [18-21].

Nevertheless, different research groups have used custom-designed and custom-manufactured pulse generators, resulting in varying pulse conditions [46-57]. This situation can pose a complex and challenging scenario when comparing and making sense of experimental outcomes. Experiments involving intense nanosecond pulses typically report key parameters like electric field strength, pulse duration, and pulse count. However, there are subtleties in pulse waveforms, including features like rise time, pulse plateau, and fall time, which also play a role [9, 26]. Even the pulse plateau isn't perfectly flat and may exhibit some degree of rise or fall between the rise and fall times. Regrettably, these waveform characteristics are often

---

<sup>1</sup> Asadipour, K., Zhou, C., Yi, V., Beebe, S. J., & Xiao, S. (2023). Ultra-Low Intensity Post-Pulse Affects Cellular Responses Caused by Nanosecond Pulsed Electric Fields. *Bioengineering*, 10(9), 1069.

inadequately characterized and left unreported. For instance, the rise time and fall time of a pulse have been shown to impact mitochondrial membrane potential and cell viability. The assumption was that a pulse with a faster rise time can more effectively penetrate the cell interior, bypassing the capacitive barrier of the cell membrane when compare to a slower-rising pulse [9]. In the case of nanosecond bipolar cancellation (NBC), when an additional pulse with an opposite polarity is applied, it results in weaker responses than a unipolar pulse condition where no such cancellation occurs [29, 58, 59]. It is possible to explain this difference in results by disrupting the charging of cell membranes by the opposite current before any damage to the cell is occurred. However, this is just one possible hypothesis, and other mechanisms might also be valid. Another overlooked aspect is the possibility that the charging current of a pulse generator (in the form of a post-pulse) could influence biological responses, even though it's often disregarded after the main pulse due to its low intensity. The post-pulse typically generates a voltage across the tissue or cell medium that is approximately ten times smaller or less than the main pulse and often doesn't register on an oscilloscope due to its small scale. Nevertheless, biological responses are frequently attributed solely to the main pulse.

## **2.2 Background and Significance**

### **2.2.1 The Use of Electrical Pulses in Medicine**

Electric stimulation has long been a valuable tool in various medical applications such as promoting fracture healing, nerve and muscle stimulation, and more. This is because electrical fields of different types and strengths can interact with cells, ions in bodily fluids, and other biochemical factors to modulate various physiological processes [60, 61]. Physiological electric fields (EFs) are essential for controlling and regulating cellular and tissue balance. Different

parts of the human body naturally generates a different biological EF [62]. These electric fields play a crucial role in processes like wound healing, tissue regeneration, and various other physiological functions. For external stimulation, researchers have conducted studies involving the placement of electrodes around affected areas to provide this stimulation [63].

Each type of electrical stimulation serves a distinct purpose within the body. Importantly, the use of different magnitudes of electrical fields has been found to achieve various biomedical objectives. For instance, low-voltage electric fields (10–100 mV) can stimulate cell proliferation, migration, and tissue regeneration [64-66]. On the other hand, higher voltage electric fields (above 1 kV) can be used to induce electroporation, apoptosis, and other processes to target and eliminate diseased tissues, such as in tumors [67]. Thus, by adjusting both the strength and the specific application, electrical stimulation can be employed in a wide range of medical contexts [68].

### **2.2.2 Nano Pulse Electrical Treatment**

Pulsed powered technology has been instrumental in enabling the study of the effects of nanosecond and even shorter pulses on biological cells and tissues. This technology focuses on the physics and applications of high-voltage pulse generators, originally developed for military purposes. The application of pulse generators to bioelectric research gained momentum in the 1990s [69]. Many of the nanosecond pulse generators used in biological research are referred to as line-type pulse generators [70]. These devices allow the generation of square-wave electrical pulses with voltages in the tens of kilovolts range and pulse durations as short as single-digit nanoseconds. The fundamental principle behind these pulse generators involves the use of transmission lines, like coaxial cables or strip-lines, with two parallel conductors separated by a dielectric layer. These lossless transmission lines can be viewed as a series of capacitors (C') and

inductors ( $L'$ ) per unit length, with an impedance ( $Z_0$ ) typically around  $50 \Omega$  for cables. Strip-lines can achieve lower impedances, around  $10 \Omega$  or less [5].

In a basic circuit of a high-power monopolar pulse generator, the transmission line is charged to the desired voltage and then discharged into the load ( $R_L$ ) using a fast-closing switch. The switch's closing time is very short compared to the pulse duration, resulting in the generation of a square wave pulse across a matched load, meaning a load with resistance equal to the transmission line impedance. The pulse duration is twice the time it takes for the pulse to complete a round trip along the transmission line. For instance, a one-meter-long coaxial cable with a relative permittivity of about 2 in the dielectric material between the conductors produces a pulse with a duration of 10 nanoseconds. Altering the cable length allows for adjustments in pulse duration. In this circuit, the voltage across the load is half of the applied voltage [5].

It's worth noting that by modifying the circuit into a "Blumlein" configuration, it's possible to generate ultrashort electrical pulses with the same amplitude as the applied voltage, rather than just half of it [70]. In studies from the Frank Reidy Research Center for Bioelectricity Blumlein pulse generators have commonly been used in most in vivo bioelectric studies while PFL have been used in most in vitro studies. However, different research groups have employed custom-designed and custom-manufactured pulse generators, resulting in variations in pulse conditions [5, 46-57] and the post pulse effects have not been analyzed.

### **2.2.3 Electrical Pulsing Parameters**

Studies investigating the effects of nanosecond pulses often vary three key parameters: the pulsed electric field ( $E$ ), pulse duration ( $\tau$ ), and pulse number ( $n$ ). These studies suggest that the crucial determinant for nanosecond pulse effects is the total number of ions that traverse the cell membrane. In simpler terms, the magnitude of biological effects depends on the product of

current density (which, in the case of constant conductivity, is directly proportional to electric field intensity as per Ohm's law) and the pulse duration [5].

For example, Nuccitelli and colleagues conducted a study in 2017, examining the effects of nanosecond pulsed electric fields (NPS, 100 ns pulses) at different voltages ranging from 12 to 30 kV/cm on three distinct cancer cell lines: MCA205 (mouse fibrosarcoma cells), McA-RH7777 (rat hepatocellular carcinoma), and Jurkat E6-1 (human leukemia cells) [71]. Their findings indicate that the induction of cell death or apoptosis in cultured cells is most pronounced at 15 kV/cm and requires a current density of 50 A/cm<sup>2</sup>, signifying that this specific magnitude of electric field is particularly effective in triggering the self-destruction of tumor cells. However, in vitro nsPEF conditions are not readily translatable in vivo. For example, Chen et al [72], treated mouse hepatocellular tumors in C57BL6 mice using 30 and 100ns pulses at 33, 50, or 68 kV/cm with one 1000 pulse treatment or three 300 pulses treatments on alternate days using needle or ring electrodes. Seventy five percent of primary hepatocellular carcinoma tumors were eradicated with 900 hundred pulses at 100 ns pulses at 68kV/cm in a single treatment or in three treatment sessions without recurrence within 9 months using a 5-needle electrode array. The ring electrode was less effective at every condition tested.

#### **2.2.4 Rise-fall Times**

The significance of the rise and fall times in nanopulse stimulation (NPS) was demonstrated by comparing 600 nanosecond pulses with fast rise and fall times (15 ns) to those with slow rise and fall times (150 ns). The faster rise and fall times had more pronounced effects in dissipating the mitochondrial membrane potential ( $\Delta\Psi_m$ ) and inducing cell death (CD) compared to the slower rise and fall times [9, 27]. Notably, these rises and fall times did not affect the influx of calcium ions (Ca<sup>2+</sup>) through the plasma membrane, indicating that these

effects were selective for intracellular structures, as previously hypothesized. The loss of  $\Delta\Psi_m$  was closely associated with a decrease in cell viability. When the pulse waveforms induced  $\text{Ca}^{2+}$  influx without affecting  $\Delta\Psi_m$ , there were no consequences for cell viability, suggesting a link between the loss of  $\Delta\Psi_m$  and loss of cell viability [9, 73]. However, the influx of  $\text{Ca}^{2+}$  during nanoporation is required for loss of  $\Delta\Psi_m$ ; the  $\text{Ca}^{2+}$  is necessary but not sufficient for cell death. Consequently, these intracellular effects have functional implications. It was also observed that the high-frequency components of the fast rise and fall times influenced  $\Delta\Psi_m$  in a manner enhanced by the presence of  $\text{Ca}^{2+}$ .

In other studies examining  $\text{Ca}^{2+}$  mobilization, it was found that pulses with shorter durations, which include higher-frequency components, had more substantial effects on the release of  $\text{Ca}^{2+}$  from intracellular stores than longer pulses (10 nanoseconds, corresponding to 100 MHz > 60 nanoseconds, corresponding to 16.7 MHz > 300 nanoseconds, corresponding to 3.3 MHz) [23]. This suggests that NPS-induced intracellular effects specifically involve intracellular calcium stores, likely the endoplasmic reticulum (ER). This hints at potential roles for NPS in stimulating intracellular  $\text{Ca}^{2+}$  signaling by affecting the ER through poration, yet most  $\text{Ca}^{2+}$  comes from outside through plasma membrane nanopores.

While not fully explored, it is likely that NPS conditions with pulse durations featuring fast rise and fall times, particularly close to the plasma membrane's charging time constant, have specific effects on mitochondria, the ER, and/or the nucleus, with physiological and pathological consequences depending on the strength of the stimulus. Therefore, it is not surprising that fast rise and fall times under intense NPS conditions can induce the translocation of calreticulin from the ER to the plasma membrane, affect nuclear substructures containing HMGB1, and impact  $\Delta\Psi_m$

by crating conditions that lead to the opening of mitochondrial permeability transition pore (mPTP), leading to ICD [35].

### **2.2.5 Monopolar and Bipolar Pulses**

The impact of the electrical pulse shape on the permeabilization of biological cell membranes has been a subject of numerous studies, although most of them have primarily concentrated on millisecond pulses [22-25]. Many of these earlier investigations suggested that bipolar pulses had a more substantial effect on electro-permeabilization when compared to monopolar pulses. The rationale behind this was that bipolar pulses compensated for the asymmetry caused by the resting transmembrane voltage at the poles of the cell during permeabilization. However, recent research involving much shorter pulses (300 and 600 ns) applied to Chinese Hamster Ovary cells found that bipolar pulses were less effective at electro-permeabilization [28, 29]. They were also not as proficient at increasing intracellular calcium concentration. Traditionally, cell permeabilization was achieved through the use of micro- and millisecond monopolar electric pulses [24, 74]. However, in the context of such monopolar electrical excitation, the application of 100-microsecond monopolar pulses at 1 Hz was reported to induce pain, discomfort, and muscle contractions, necessitating the use of muscle relaxants and anesthesia [75-77]. These issues can be mitigated, for instance, by applying pulses at higher frequencies [78], using specialized electrode designs [79, 80], or delivering bursts of short, high-frequency bipolar pulses [81, 82].

Short-duration pulses help reduce muscle contractions and are thus a valuable modality for ablative treatments of solid tumors [83]. This approach enhances patient safety by eliminating or greatly reducing the need for neuromuscular-blocking drugs to inhibit muscle contractions.

Short-duration pulses also minimize localized thermal heating [84] and reduce the potential for side effects such as hyperthermia or cell damage.

It's important to note that all of t of these studies focused on the main pulse and overlooked the post-pulse due to its lower intensity. The post-pulse typically generates a voltage across the tissue or cell medium that is approximately ten times weaker than the main pulse, and it often goes unnoticed on an oscilloscope due to its small scale. Nevertheless, biological responses are often attributed solely to the main pulse.

### **2.2.6 Significance**

Our represents the first investigation into the impact of post-pulses on biological responses triggered by nanosecond pulses. Two pulse generators were employed based on transmission lines, specifically a PFL and a BL, to illustrate the distinct characteristics of these post-pulses while maintaining nearly identical main pulse frequency and voltage distributions It's noteworthy that PFL and BL continue to be robust pulse generators for in vitro applications that demand high current, low impedance, and short pulse durations (less than or equal to 100 nanoseconds), despite the increasing use of solid-state pulse generators [30].

Understanding how nanosecond pulsed electric fields (nsPEFs) interact with ultra-low-intensity post-pulses is critical for advancing the applications of pulse power technologies across various fields. These findings could have implications for enhancing therapeutic strategies, such as tumor ablation, atrium ablation for heart defibrillation, and for eliciting immune responses in cancer treatment. Furthermore, delving into the underlying mechanisms can provide valuable insights into the fundamental principles governing pulse waveforms and cellular responses to nsPEFs. Our study underscores the importance of characterizing and reporting pulse waveforms

to enhance the selectivity, reproducibility, and comparability of results among different research groups employing different generators.

## **2.3 Material and Methods**

### **2.3.1 Pulse Generators and Cell Exposure System**

Two pulse generators were utilized in the experiments. The first generator employed a PFL comprised of five 50  $\Omega$  cables (RG-8) to generate 100 ns pulses. The second generator utilized a BL constructed with ten 50  $\Omega$  cables (RG-58), also producing 100 ns pulses (see details in chs. 15 & 16 in [1]). For both pulse generators, the lengths of the cables were determined based on a propagation length of 5 ns/m. Under ideally matched conditions, both loads required a resistance of 10  $\Omega$ . The switches for these generators were atmospheric pressure spark gaps. These spark gaps consisted of polished, plane-plane brass electrodes and would self-close once the voltage exceeded the breakdown threshold. During the experiment, the breakdown voltages of the two pulse generators were regulated by adjusting the gap distances of the corresponding spark switches. Both generators were powered by the same high voltage supply (Glassman, series EH, 60 kV). No extra charging resistor was employed throughout the experiments. The pulse repetition rate was set at 1 Hz, controlled by the current setting on the power supply. Standard electroporation cuvettes with a 1-mm gap distance were used for the experiments. The solution contained within the cuvettes resulted in a resistance that was close to 10  $\Omega$ , eliminating the need for additional resistance for impedance matching. The pulse waveforms were measured with a custom-made, calibrated, high precision resistor divider (1000:1).

### **2.3.2 Cell Culture**

The murine melanoma cell line B16F10 (ATCC® CRL-6475TM) was used in this study. The cells were grown in a humidified incubator at 37 °C with 5% CO<sub>2</sub> in the Dulbecco's Modified Eagle Medium (DMEM) produced by ATCC (30-2002), supplemented with 10% fetal bovine serum (FBS) (ATCC, 30-2020) and 1% of penicillin-streptomycin (Sigma-Aldrich). B16F10 cells were harvested with 0.25% (*w/v*) Trypsin- 0.1% EDTA solution (Corning, MT25053CI). The cells were passaged no more than 20 times. Initial cell counts and viability were determined using a 0.4% trypan blue exclusion viability assay (Corning, 25900CI). Cells with greater than 95% viability were washed with PBS, centrifuged at 300 RCF for 5 min at room temperature, and resuspended at a concentration of  $1 \times 10^5$  cells/ 100  $\mu$ L for nsPEF treatments. In all experiments, cell suspensions were added to 100  $\mu$ L cuvettes (1-mm gap sterile electroporation cuvette, BioSmith, U-72001) and treated with a BL or PFL pulser in the culture medium with the conductivity of 1.18 S/m.

### **2.3.3 tPMET Rate Determination**

The Cell Counting Kit-8 (CCK-8/WST-8-reducing NADH oxidoreductase activity, Dojindo, CK04-11) was used here to measure the trans-PM electron transport (t-PMET) of the plasma membrane redox system (PMRS). The quantification of the final electron acceptor (WST-8 reduction) was based on the change in absorption at 450 nm per minute of incubation. Cell suspensions with a concentration of  $4 \times 10^5$  cells/100  $\mu$ L were added to cuvettes for treatment with different pulsers and varying numbers of pulses. Following the nsPEF treatment, the CCK-8 reagent was added (at a 1:1 volume ratio) and mixed immediately, and the cells were transferred to 384-well plates (Greiner Bio-One CELLSTAR plate, with cover, from VWR, 50051816) with 30  $\mu$ L per well. Microplate readers (Spectra Max i3) were used to measure the

absorbance at 450 nm at 37 °C for 0–90 min. The tPMET rates were determined based on linear time courses between 10 and 35 min, as specified in the statistics analysis section.

#### **2.3.4 Cell Viability Analysis**

The Cell Counting Kit 8 (CCK-8, Dojindo, Kumamoto, Japan) was used to measure cell viability. B16F10 cells were grown to 80% confluency, and then the cell concentration was adjusted to  $1 \times 10^6$  cells/mL for nsPEF treatment. Following the pulsing, 15,000 cells were seeded into 96-well plates (Corning Incorporated, Corning, NY, USA). The cells were cultured for 24 h, after which 10  $\mu$ L of CCK-8 solution (1:10 v/v) was added to each well. Following an additional 1.5 h incubation, the optical density was measured at an absorbent of 450 nm using a microplate reader (ELx800; BioTek Instruments, Inc., VT, USA). The OD value was divided by the control value to calculate the relative cell survival rate (background values were subtracted).

#### **2.3.5 Live Cell Imaging**

Using confocal scanning imaging with a Leica TCS SP8 microscope, cells which were seeded on 8 well plate for 24 hours later, were stained to assess mitochondrial membrane potential (0.5  $\mu$ M TMRE), and cytosolic ROS levels (10  $\mu$ M H<sub>2</sub>DCFDA (Invitrogen)), immediately after exposed to nsPEF (10 pulses, 200 ns, 20 kV/cm, 1 Hz). Pre-incubation of cells for 10 minutes prior to nsPEF exposure ensured uniform conditions.

#### **2.3.6 Flow Cytometry**

$\Delta\Psi_m$  was detected using tetramethylrhodamine ethyl ester, perchlorate (TMRE; Immunochemistry Technologies LLC, Bloomington, MN, USA). B16F10 cells were harvested, counted, and resuspended following the previously described method. The samples were then treated with the BL and PFL pulsers, and TMRE was added to the cells at a concentration of 0.3

$\mu\text{M}$ . The cells were incubated for 20 min, protected from light. Cells were not subjected to pre-incubation prior to pulsing, as we observed that this could adversely impact cell viability [54]. The optimal approach is to introduce the dye immediately after pulsing and incubate it for precisely 20 min.

The same procedure was employed to detect ROS using MitoSOX-Red (MSOX; Invitrogen, Molecular Probes, Inc., Eugene, OR, USA), albeit with a final concentration of 2  $\mu\text{M}$ . Red fluorescence from TMRE and ROS was detected in separate experiments using the PE channel on a Miltenyi MacsQuant Analyzer 10 flow cytometer, as both molecules share the same excitation/emission characteristics.

To detect cell permeabilization, cells were exposed to nsPEFs, and Propidium Iodide (PI; Invitrogen, P3566) was added to a final concentration of 10  $\mu\text{g}/\text{mL}$  immediately after pulsing. Cells were then analyzed by flow cytometry 10 min after nsPEF treatment using the FITC channel [27]. Untreated and/or unstained samples were used as negative controls for treatment and fluorescence, respectively, in all experimental groups. Data analysis was conducted using FlowJo™ Software (Windows) Version 10 (Ashland, OR: Becton, Dickinson, and Company; 2019).

### **2.3.7 Seahorse Assay**

The OCR (oxygen consumption rate) was measured using an XF HS Mini Analyzer (Seahorse Bioscience). Following the pulsing treatment, B16F10 cells were seeded into XFp cell culture 8-well mini plates in duplicate at a density of  $3 \times 10^3$  cells/well. The cells were then cultured under standard conditions for 15 h. Before measurement, the medium was replaced with Seahorse XF Assay Media (Agilent, Santa Clara, CA, USA) with a pH of 7.4. The assay media was supplemented with 10-mM glucose, 2-mM L-glutamine, and 1-mM pyruvate. For the

mitochondrial stress test, the following inhibitors were used at the indicated final concentrations: 1.5- $\mu$ M oligomycin, 1- $\mu$ M FCCP, and 0.5- $\mu$ M rotenone–antimycin A. Two wells without cells were included to assess non-cellular oxygen consumption, and the value of non-cellular oxygen consumption was subtracted from the cellular OCR value. After completing the experiment, the OCR data were normalized to the number of cells.

### **2.3.8 Statistics Analysis**

The tPMET data obtained from the 10–30-min time period was subjected to linear regression analysis using GraphPad Prism version 9 (GraphPad Software, San Diego, CA, USA). Statistical analyses comparing the tPMET rates of the samples to the control were conducted using one-way ANOVA. For the Seahorse data obtained from the XF HS Mini, analysis and normalization of the number of cells were performed using Agilent Seahorse Wave Desktop software (Agilent Technologies, USA). Flow cytometry analysis was carried out using FlowJo™ Software Version 10 (Ashland, OR: Becton, Dickinson, and Company; 2019). All experiments were conducted at least three times, and the data were expressed as Mean  $\pm$  Standard Error of the Mean (S.E.M.). Statistical analyses such as one-way or two-way ANOVA were performed using GraphPad Prism, with a significance level of  $p < 0.05$ .

## **2.4 Results**

### **2.4.1 Two pulse generators with the same 100 ns primary pulse result in low-intensity post-pulses with the BL waveform longer and with opposite polarity to the primary**

**pulse and the PFL waveform shorter and with the same polarity to the primary pulse**

The 100 ns pulses generated by PFL and BL are shown in Fig. 1. These waveforms were obtained for the cuvettes with a resistance of approximately 10  $\Omega$ , which was needed to match PFL and BL. Five voltages (1.5, 2, 3, 4, and 5 kV) and ten waveforms are shown, with each representing the average waveform over 30 pulses. For a given voltage, the rise times for both PFL and BL were about the same, but the pulse duration for BL was slightly longer than that of PFL. The fall times of the PFL pulses were slightly shorter than those of the BL pulses. The charges flowing through the load were calculated as the time integral of the voltage divided by the resistance,  $\int V/R dt$ , where  $R = 10 \Omega$  (Figure 1c). The charge for BL was always slightly higher than or equal to that of PFL. Also shown in the figure (Figure 1d) is the energy calculated by the integral of the power,  $\int V^2/R dt$ . As the voltage increased, the difference in energy deposited in the load resistance between PFL and BL became larger. However, the energy for BL was always larger than that of PFL.

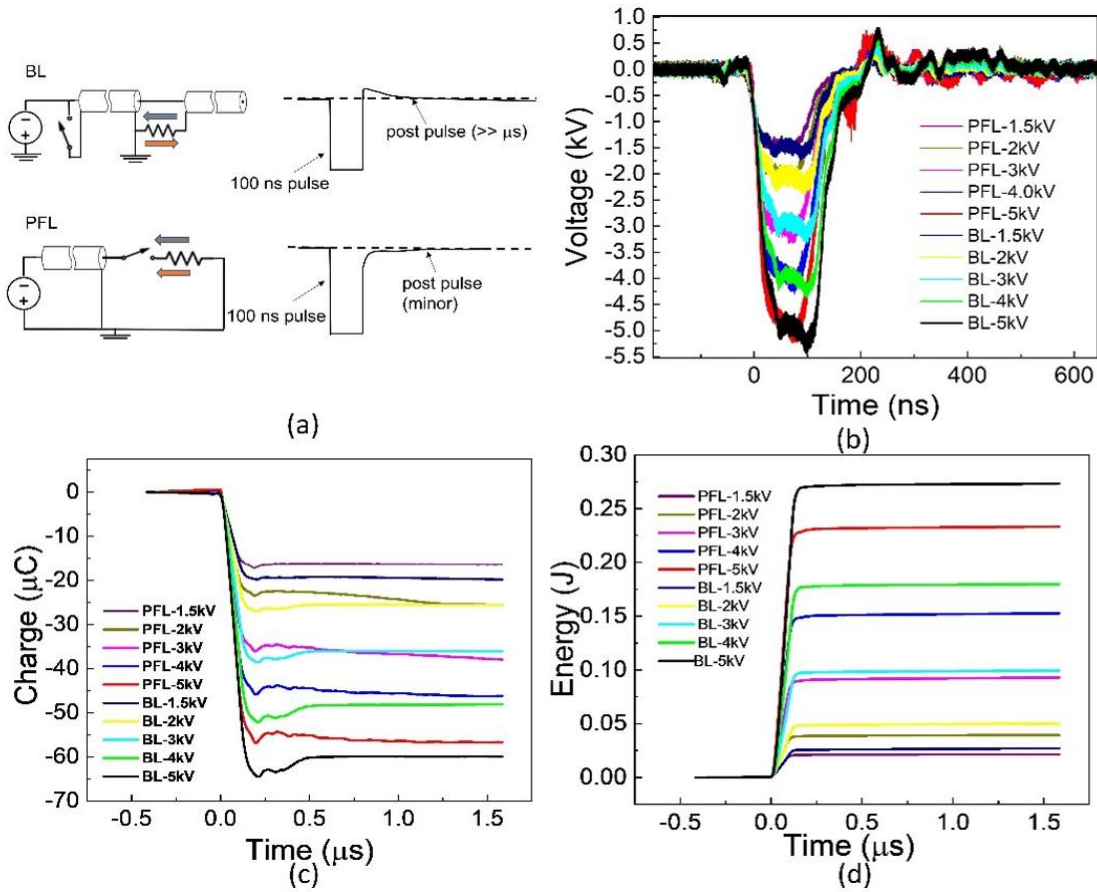


**Figure 1.** The waveforms were generated using two pulse generators. The Blumlein line (BL) and the pulse forming line (PFL). (a): The BL exhibits an opposite polarity post-pulse compared to the main pulse, whereas the PFL has a post-pulse with the same polarity. In the figure, the BL pulse is intentionally inverted to match the text, although it should be positive due to the negative charging power supply concerning the ground. The grey arrow is pulse current; The orange arrow is post pulse current. (b): The waveforms display a voltage increase from  $-1.5$  kV to  $-5$  kV. Each waveform represents the average of 30 consecutive waveforms. (c): The charges delivered to the load are calculated by integrating the current over time. In this case, the load was a cuvette. (d): The energy deposited into the load [45].

To examine the difference in the spectrum of the PFL and BL pulses, Fourier transform (FT) was performed on the 4 kV data (both PFL and BL) over three time-intervals: the prepulse (-450 ns to -100 ns), the main pulse (-100 ns to 500 ns), and the post pulse (500 ns to 1600 ns) (Figure 2a-d). In the prepulse, only a very low-intensity DC signal ( $<10$  arbitrary units) was observed (Figure 2b), which was introduced due to the abrupt signal appearance at -450 ns. In the main pulse phase, the BL spectrum almost overlapped with that of the PFL, although it appeared slightly higher in the near DC frequency (Figure 2c). In the post pulse phase, the PFL spectrum appeared higher than the BL one near the low frequencies (up to  $2.5 \times 10^7$  Hz). Additionally, the post pulse difference between the PFL and BL waveforms for all voltages can be seen in Figure 3, which were obtained using STFT (short-time Fourier Transform). The PFL post-pulses consistently exhibited a more extended signal spread than the BL pulses, despite mostly being low intensity.

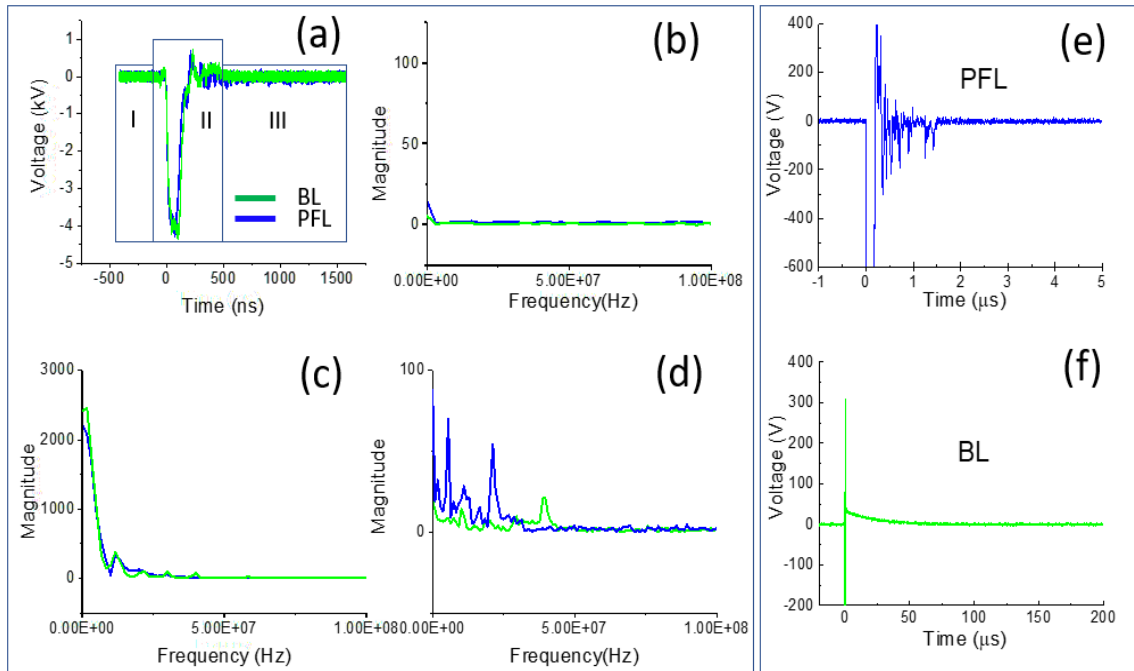


**Figure 2.** The pulse waveforms were analyzed in both the time and frequency domains. (a) The intervals of interest in the waveform, including the prepulse ( $-450$  ns to  $-100$  ns), main pulse ( $-100$  ns to  $500$  ns), and post-pulse ( $500$  ns to  $1600$  ns); the spectrum of the pulses was calculated for each interval using FFT: (b) the prepulse; (c) the main pulse; and (d) the post-pulse; (e,f) zoomed-in views of the post-pulses for both PFL and BL on a smaller voltage and longer time scale [45].

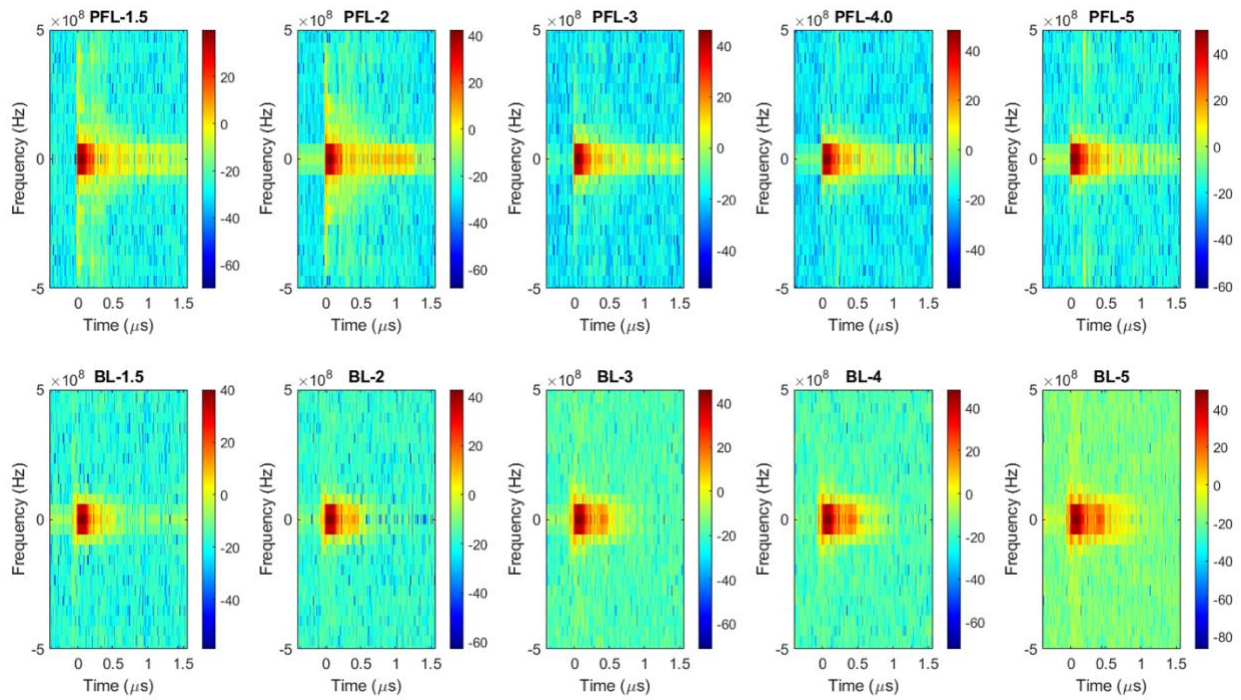


**Figure 3.** The spectrums of the pulses over time were calculated for the PFL and BL waveforms using STFT performed on the data shown in Figure 1b. Top row: the PFL voltages ( $-1.5$  kV to  $-5$  kV); bottom row: the BL voltages ( $-1.5$  kV to  $-5$  kV). The color bars show the magnitude of the spectrum [45].

Such a large difference led us to examine the post-pulse phases in the time domain again.

However, this was done at a much smaller voltage scale with a longer time. Figure 2e and Figure 2f shows the post pulses for both PFL and BL. The main pulses were both  $-4$  kV but were cutoff to show the difference. For PFL, the post pulse had the same polarity as the main pulse and only lasted less than  $2 \mu\text{s}$ . For BL, the post pulse had the opposite polarity to the main pulse and lasted much longer ( $50 \mu\text{s}$ ). But it is noted that both BL and PFL's post-pulses contained two components: the charging voltage and a mismatched component due to the impedance mismatching between the transmission line and the cuvette. Comparing the duration, the

charging pulses extended much longer, although their magnitudes were small and decaying: the PFL's was (5%) of the main pulse, whereas the BL's was (1-2%) of the main pulse.

#### **2.4.2 PFL Pulses Extended the Duration of OMP and Posed Less Change on IMP than BL Pulses**

Using a linear cell model comprising of resistances and capacitances corresponding to the cell structure [85], potential drops across the outer membrane and intracellular organelle membrane were obtained for three cases: the clean pulse, the PFL pulse, and the BL pulse. There was no difference among all pulse conditions during the 100 ns main pulse for the OMP. The pulses in all cases caused the IMP to increase by approximately threefold as compared to the OMP, suggesting that nanosecond pulses generally bypass the outer membrane and penetrate to the cytoplasm for intracellular manipulation (Figure 4a). After the main pulse (>100 ns), the IMPs reversed their polarity and swung in the opposite direction, with the magnitude being 13.3% of that during the main pulse for the CP and BL pulses. Conversely, the PFL post-pulse caused a smaller change in the IMP, reducing it to only 8% of its value during the main pulse. Additionally, the PL post-pulse sustained the OMP longer than the CP and BL pulses. The BL pulse dissipated the OMP rather rapidly (<4  $\mu$ s) and led to a reversed OMP.

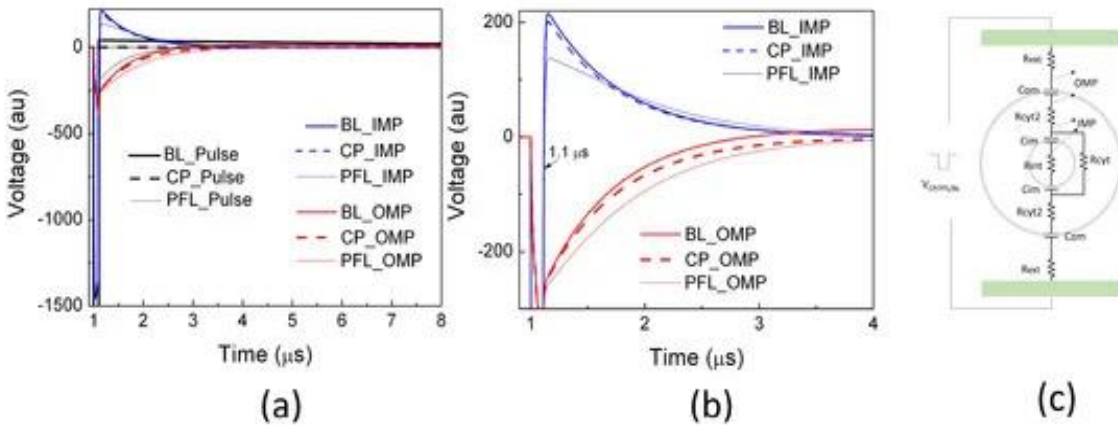


**Figure 4.** The potential drops were simulated using a linear equivalent cell model by applying a clean pulse (CP), a PFL pulse, and a BL pulse at 1  $\mu\text{s}$  [45]. The potential between the outer membrane (OMP) and the potential between an intracellular organelle (e.g., mitochondrion) (IMP) are shown in (a) on a larger scale (both in voltage and time) and (b) on a smaller scale. (c) The equivalent cell model in Pspice (Version 9.1) along with the parameters ( $R_{\text{ext}}= 1 \text{ k}\Omega$ ,  $C_{\text{om}} = 100 \text{ pF}$ ,  $R_{\text{cyt}2} = 100 \text{ }\Omega$ ,  $C_{\text{im}} = 10 \text{ pF}$ ,  $R_{\text{cyt}} = 10 \text{ k}\Omega$  [85].

The ability of the BL post pulse to reverse the OMP is significant because of its much longer duration ( $>100 \text{ ns}$ ) despite staying at a low voltage. In general, the PFL post pulse of the same polarity as the main pulse extended the duration of OMP, while the BL post pulse shortened the duration of OMP and even reversed it. Additionally, the PFL post pulse caused less change in the IMP than the BL post pulses. These two observations indicate that the PFL pulse can preserve the membrane potential changes of both IMP and OMP longer than the BL pulse and therefore is predicted to be more potent. However, we note that this model has limitations in that it assumes the cell membranes stay intact, and the resistances remain the same without the influences from factors such as electroporation, shapes, orientations, etc. It is a qualitative

analysis useful only for predicting the general trend of the potential change resulting from the electric pulses and does not reflect the absolute membrane potential change.

### **2.4.3 Effects of PFL and BL Pulsers on Cellular Plasma Membrane Responses**

Plasma membranes (PMs) are best known as physical barriers that define the cell and maintain ion transport across the membrane as a means of excitability and homeostatic maintenance. The PM also exhibits an electron transport (ET) mechanism carried out by plasma membrane redox systems (PMRSs). These ET systems transfer electrons from either intra- or extracellular donors to extracellular acceptors [86, 87]. They regulate cellular redox homeostasis by maintaining a higher NAD(P)<sup>+</sup>/NAD(P)H ratios to support glycolysis and attenuate oxidative stress acting as a compensatory mechanism during the stress, and the aging process [88]. Given the known effects of electric fields to electroporate the PM, it was of interest to see if the PFL and BL pulsers had different effects on PM permeabilization as propidium iodide uptake and effects on trans plasma membrane electron transport (tPMET).

Figure 5 shows two distinct responses from the plasma membrane for the PMRS regulating tPMET rates and plasma membrane permeability to propidium iodide (PI) in response to the PFL and BL pulsers. The linear tPMET velocity rates were measured in the 10-35 minute range, which serves to measure the tPMET activity of the PMRS in B16F10 cells after pulsing with the BL or PFL pulser. The PFL pulser showed biphasic tPMET rates across different ranges of nsPEF pulsing. Under lower pulsing conditions ( $\leq 5$  pulses), nsPEFs increased tPMET rates above the control rates while there was no increase in PI influx. However, under higher pulsing conditions ( $\geq 10$  pulses), tPMET rates decreased below the control rates as there were increases in PI influx coincident with the decrease in tPMET. The maximum dimension of the PI molecule is typically 1.4 nm. Therefore, the absence of PI uptake does not definitively prove that the cell

membrane is completely electroporation pore-free, as nsPEFs have been observed to create smaller nanopores that can cause Ca<sup>2+</sup> influx [89]. In contrast, the BL pulser at low pulsing conditions ( $\leq 5$  pulses) showed the same level of tPMET activity as the control. However, as the pulse number was increased to  $\geq 20$ , a significant pulse number-dependent reduction in tPMET activity was observed coincident with a pulse number-dependent increase in PI influx. In general, for both the decrease in tPMET and the increase in PI influx, the PFL has a lower threshold or is more sensitive for determining these changes in cell responses. Thus, the PFL pulses can elicit a biphasic response, stimulating tPMET activity with a low number of pulses, but inhibiting it with a high number of pulses. In contrast, the BL pulses did not induce such a biphasic response and only inhibited tPMET.

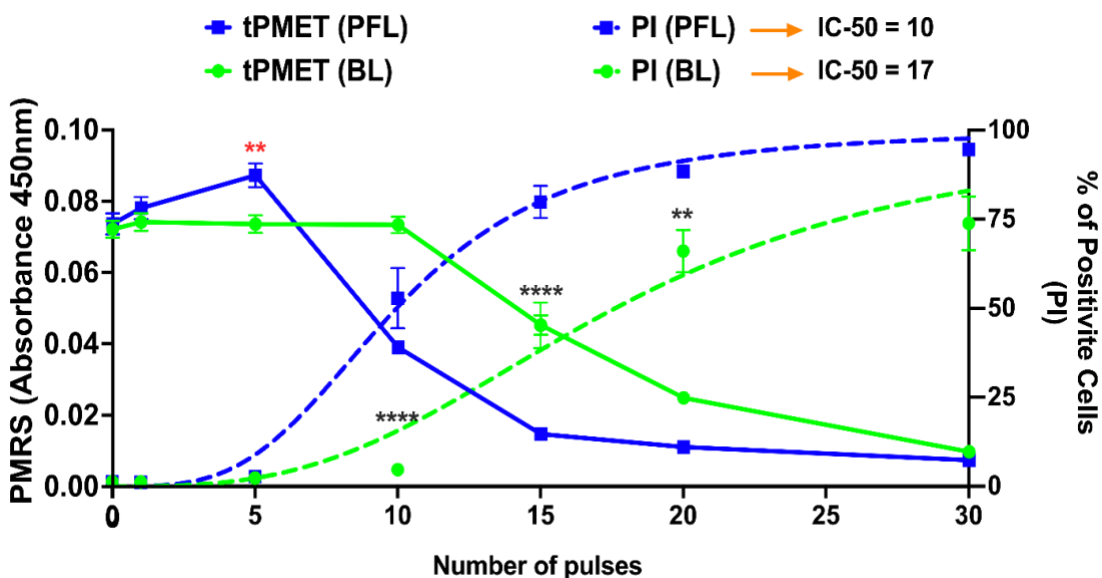


**Figure 5.** nsPEF effects of BL and PFL pulsers on tPMET and PI uptake. The tPMET rates defined as the rate of increase in WST-8 absorbance per min of reaction (left axis, solid lines), and PI fluorescence (Right axis, dotted lines) were determined by plate reader (10–35 min) and flow cytometry (5 min) respectively in a different assay. B16F10 cells were exposed to different pulsing

numbers with BL or PFL (green and blue color code respectively) with a fixed electric field of 40 kV/cm. BL pulser showed the inhibitory effect on tPMET (significant decrease start at 20 pulses compared to control) while the PFL showed the biphasic effect on tPMET with a significant increase at fewer pulsing numbers (5 pulses, showed by red \*\*) and then decrease for high pulsing number (significant decrease at 10 pulses). Significant differences were observed between these two pulsers regarding an increase in PI uptake (at 10, 15, 20, and 30 Pulses), indicated by the (\*\*\*\*). (n = 3) \*\* p < 0.05 and \*\*\*\* p < 0.0001 [45].

#### 2.4.4 PFL has a lower IC 50 for cell death induction than BL

Figure 6a shows the effects on cell viability 24 hours after PFL and BL pulsing (100ns, 40 kV/cm) with different pulsing numbers. Viability was found to be dependent on the number of pulses, such that the PFL IC50 value was 9 pulses and the BL IC50 value was 14 pulses. For 100 ns and 40 kV/cm, the decrease in cell viability from 95% to 25% occurred between 5 and 15 pulses for the PFL pulser and between 10 and 20 pulses for the BL pulser.

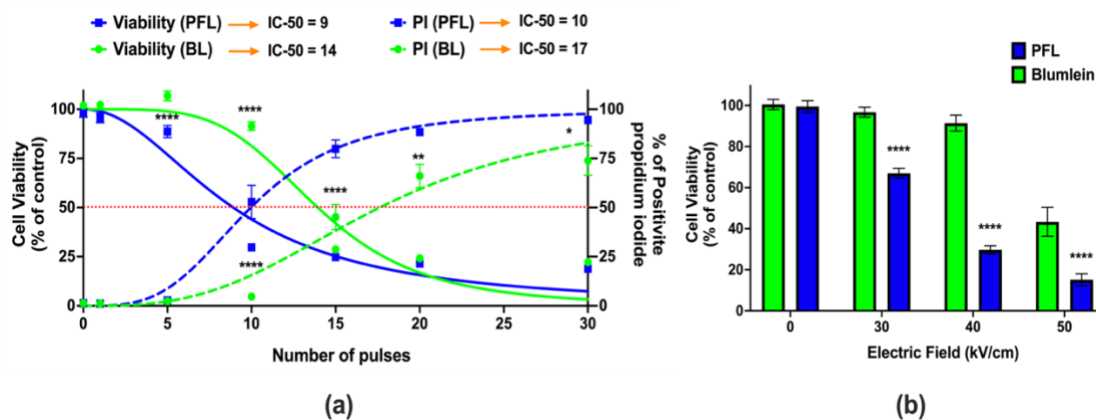


**Figure 6.** nsPEF effects of BL and PFL pulsers cell viability. Cell viability of B16F10 cells was determined using a plate reader after 24 h for (a) various pulsing numbers with a fixed electric field of 40 kV/cm, or (b) different electric fields (0, 30, 40, and 50 kV/cm) of 10 pulses, with BL

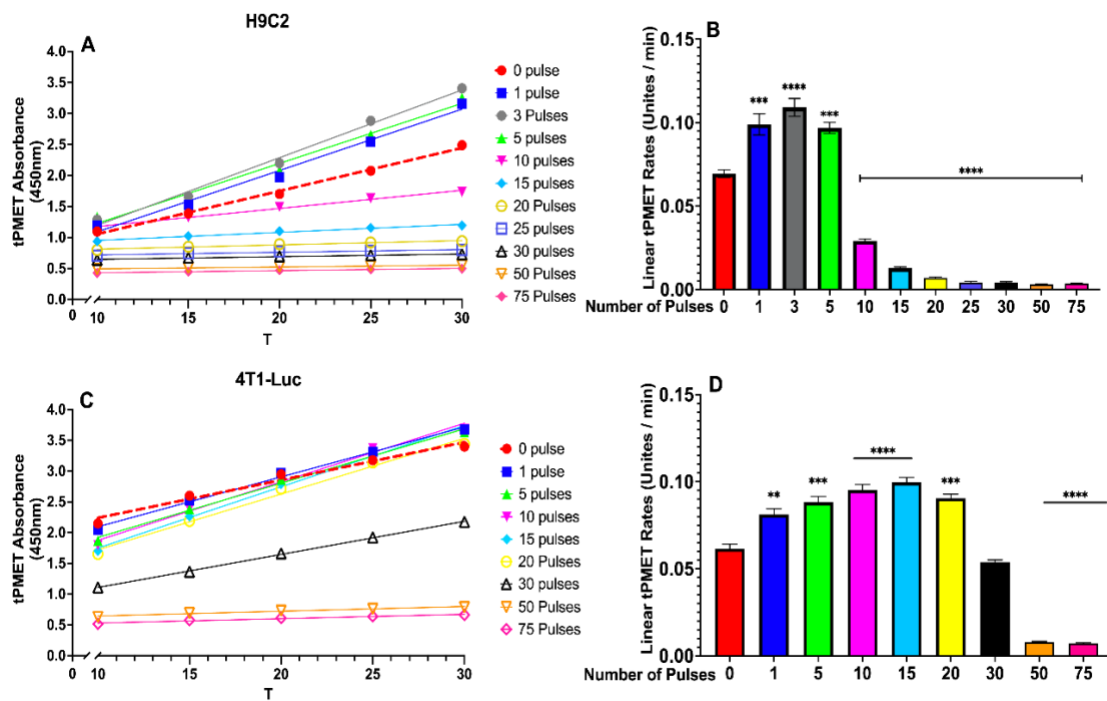
(green) or PFL (blue) pulsers. In (a), significant differences were observed between these two pulsers, particularly at 5 and 10 pulses. In (b), the viability did not show a significant decrease compared to the control at 30 and 40 kV/cm with BL pulsing, whereas with PFL pulsing, a significant decrease in viability was observed (\*\*\*\*  $p < 0.0001$ ) [45].

Figure 6b considers the electric field decreases in cell viability with the 100 ns pulses at 10 pulses. For PFL pulses, cell viability began to decrease at a threshold of 30 kV/cm. On the other hand, a significant decrease in viability for BL pulses was observed only when the electric field was raised to 50 kV/cm, with a slight decrease noticeable at 40 kV/cm.

#### **2.4.5 Biphasic effects of nsPEFs on tPMET in cancerous and non-cancerous cells**

To find the effects of PFL pulser on tPMET activity in H9c2 cardiac myoblast and 4T1-luc mammary cancer cells, we used the same method as described. Figure 7 show linear velocity rates in the 10-30 min range as measures of tPMET activity in H9c2 and 4T1-luc, respectively. Control (non-pulsed) rates are shown in red dotted lines and rates are similar for H9c2 and 4T1-luc cells (0.06-0.07 Units/min). Both cell lines show biphasic tPMET rates over different ranges of nsPEF charging conditions with PFL generator. At lower charger conditions, nsPEFs increase tPMET rates above control rates while at higher charging conditions, the tPMET rates decrease below control rates. For both cell lines, the increases in tPMET activity rates were similar with about 0.1 Units/min. However, the increases in pulse number required to express this maximum increase in tPMET were considerably higher for 4T1-luc (15 pulses) than for H9c2 cells (3 pulses). Above these pulsing numbers, tPMET rates decrease. That is the tPMET rates decreased after 30 pulses for 4T1-luc and  $\leq 10$  pulses for H9c2. Thus, for the maximum increase in tPMET above control, nsPEFs required more than a >2-fold increase in charging in the 4T1-luc breast

cancer cells than the H9c2 heart cells. Since these PMRS oxidoreductases are heterogeneous and cell type-specific and are known to be different among cancer cells, these differently measured enzyme rates for the two cell types are likely due to different PMRS enzyme systems. Nevertheless, both cell types exhibit biphasic tPMET rates in response to PFL, otherwise, the cells from non-cancerous versus cancerous origins respond differently. This biphasic effect on tPMET is typical of a hormetic effect, which is beneficial and stress-adaptive under lower conditions, yet greater conditions induce harmful effects [90]. Upregulation of tPMET has been reported to help cells under mitochondrial stress or distress [91].



**Figure 7.** tPMET rates of H9c2 non-cancer cardiac myoblasts and 4T1-luc mammary cancer cells. The linear portions of the PMET rates are shown for (a) H9c2 non-cancer cardiac myoblasts and (b) 4T1-luc mammary cancer cells with linear rates determined between times 10 – 30 mins after nsPEF. Typical tPMET rates are shown on the left, while the linear rates corresponding to each

pulsing condition are indicated on the left side in proximity to their respective conditions. The conditions are arranged in descending order, with the highest rates presented first. (\*significantly different than control, n=5, p < 0.05, One-way ANOVA) [31].

#### **2.4.6 PFL induce different effects on tPMET activity and cell viability in cancerous and non-cancerous cells**

Differences in these tPMET activities and their meaning in cell function can be informative when comparing the tPMET rates with cell viability for nsPEFs conditions. Figure 8 shows the tPMET rates and cell viability as a percent of control, for H9c2 cells and 4T1-luc cells, respectively. Notice that H9c2 cells have elevated tPMET activity up to 5 pulses but then begin to exhibit reduced tPMET activity. In contrast, 4T1 cells have elevated tPMET activities up to 20 pulses before beginning to lose tPMET activity. While 4T1-luc cells show an enhanced tPMET activity above control as high as 20 pulses H9c2 cells have lost 80-90% of their tPMET capacity at that 4T1-luc activity peak, yet both cell lines have just begun to lose viability at 20 pulses. 4T1-luc cells continue increasing tPMET activity under conditions while cells will have begun to die as seen 24h later.

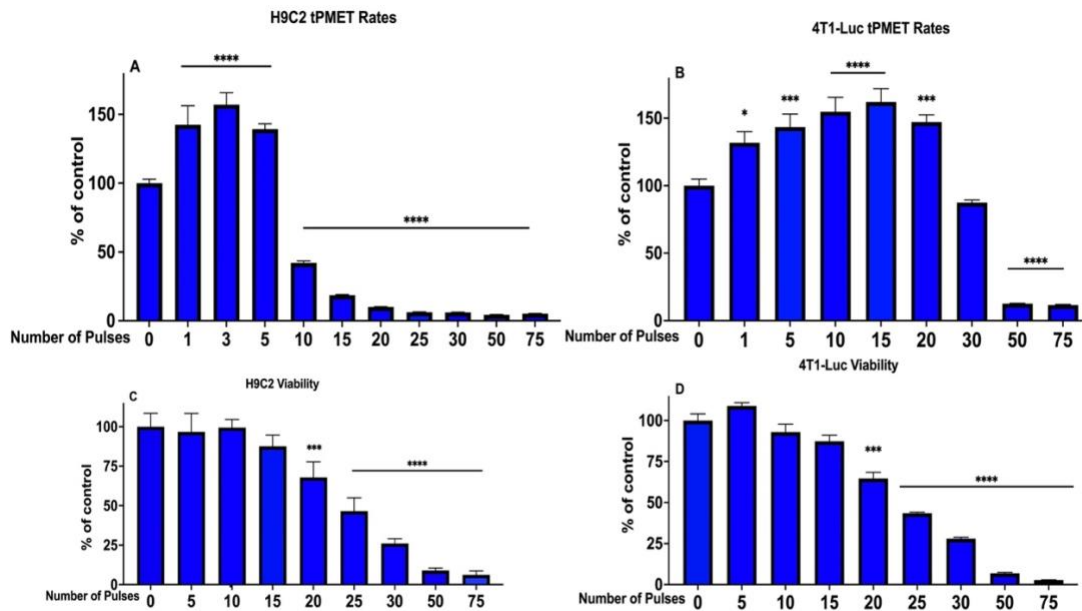


**Figure 8.** Relationships between H9c2 cells and 4T1-luc cells among tPMET rates, and viability. Linear rates of tPMET were determined in Figure 1 and shown as percent of control (A and B), and cell viability (C and D) for H9c2 cells and 4T1-luc cells, respectively. Vs/cm are shown for the various pulse numbers or Vs/cm. (\* significantly different than control, n=5 for Linear rates of tPMET, and n=3 for viability  $p < 0.05$ , One-way ANOVA) [31].

In H9c2 cells, as the nsPEF charging increases above 5 pulses, the tPMET activity falls quickly while cell viability falls more slowly and is significantly less than the control at 20 pulses. In contrast, in 4T1-luc cells, cell viability falls rather slowly with at 20 pulses, while tPMET activity is still above the control value until it is significantly below the control value at 30 pulses. This suggests that tPMET activity helps maintain 4T1-luc cell viability, while it is much less effective to maintain viability in H9c2 cells. This correlation between tPMET activity and viability is more typical of proliferating cells dependent on glycolysis because NAD<sup>+</sup> is reduced in glycolysis and the PPP produces NADH. The PMRS supports viability by restoring

NAD<sup>+</sup>, which is needed to continue glycolysis to enhance metabolic flux in proliferating cells. H9c2 heart cells depend more on OxPhos for their ATP and function. With the decrease of tPMET activity, NAD(P)H and other reductive equivalents will increase, producing reductive stress and elevated ROS levels [31].

Under these nsPEF conditions of 5 pulses the tPMET activity in H9c2 cells is just at its activation peak and is decreasing at 10 pulses and has decreased to less than half of the control rate value. Yet both are conditions that do not show a significant loss of viability 24h later. This is typical of the beginning of a mitochondrial failure where there is an increase in tPMET activity to maintain an equilibrium in redox homeostasis.

Because PFL show a biphasic effect on tPMET, it mimics a hormesis effect as defined as a process in which a low dose of an agent or environmental factor that is damaging at a high dose induces an adaptive or beneficial effect to a cell or organism [90]. Although it is not clear what the mechanism for the increase in tPMET is, it is beneficial for cells at low doses and damaging at high doses [31].

#### **2.4.7 Determining best timing after nsPEF to measure $\Delta\Psi_m$ and ROS production**

Figure 9 shows the Microscopy strategy to determine best timing in terms of reduction in  $\Delta\Psi_m$  and increase in ROS after nsPEF. A microscopy strategy involving 10 pulses was implemented to capture the dynamic alterations in cellular responses. To assess mitochondrial membrane potential, cells were stained with 0.5  $\mu\text{M}$  TMRE, while cytosolic ROS levels were measured using 10  $\mu\text{M}$  H2DCFDA. Confocal microscopy images were acquired with a 60X magnification objective, and subsequent analysis of fluorescent intensity was conducted using ImageJ software. The choice of a 20-minute interval post-nsPEF was deemed appropriate for

Flow Cytometry analysis, providing valuable insights into the cellular responses triggered by nsPEF exposure.

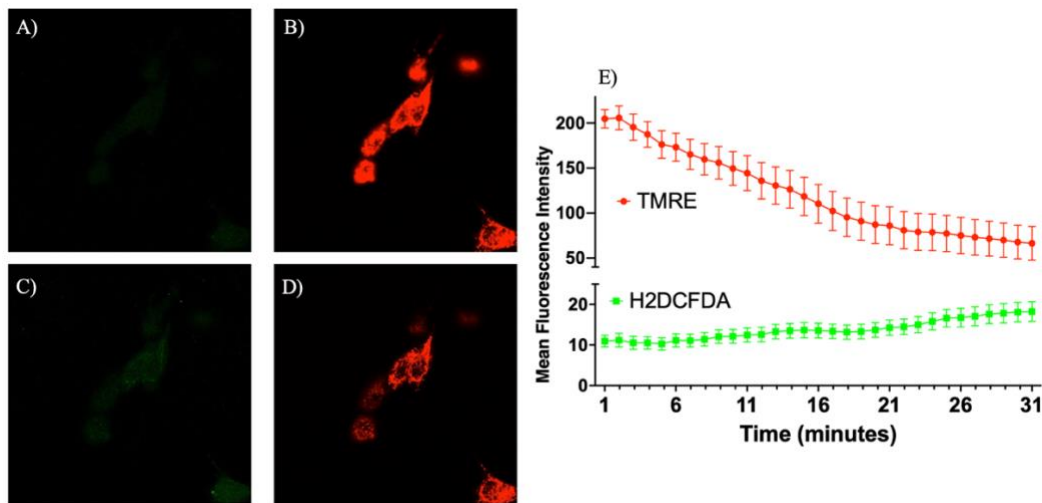


**Figure 9.** A 20-minute interval is an appropriate duration for capturing alterations in mitochondrial membrane potential and the presence of reactive oxygen species. Assessment of Mitochondrial Membrane Potential and Cytosolic ROS Levels in H9C2 Cells Following nsPEF Exposure. Confocal microscopy images of H9C2 cells stained with 0.5  $\mu$ M TMRE to measure mitochondrial membrane potential and 10  $\mu$ M H2DCFDA to assess cytosolic ROS levels. Cells were incubated for 10 minutes prior to nsPEF exposure. Quantification of mitochondrial membrane potential and cytosolic ROS levels in H9C2 cells subjected to nsPEFs (200 ns, 20 kV/cm, 1 Hz, 10 pulses) with a 60X magnification objective. Fluorescent intensity was analyzed using ImageJ software.

It is important to note that due to the limitations imposed by the microscope setup, a specific setting was adopted for the nsPEF exposure. The choice of this particular pulser and setting provided valuable insights into the experimental conditions, shedding light on the technical constraints associated with the microscopic analysis. Importantly, this section not only contributed to the understanding of the cellular responses under nsPEF but also served as a guide

for establishing a more accurate timing for subsequent measurements on the Flow Cytometry machine. By acknowledging and addressing the intricacies of the experimental setup, the methodology ensured a comprehensive and precise approach to evaluating changes in mitochondrial membrane potential and cytosolic ROS levels, enhancing the overall reliability and relevance of the study's findings.

#### **2.4.8 Differential loss of $\Delta\Psi_m$ with increases in mROS production with the PFL and the BL pulsers**

Figure 10 shows nsPEF-induced mitochondrial ROS (mROS) production determined by MitoSox (solid lines) and change in the  $\Delta\Psi_m$  (dotted lines) as pulse numbers are increased at 40 kV/cm. In contrast to the differential loss of  $\Delta\Psi_m$  as the PFL (blue lines) and BL pulse (green lines) numbers increased, there was no difference in the production of ROS between the two pulsers. For the PFL, 75% of cells were mROS positive and only about 25% of cells had a loss in  $\Delta\Psi_m$ . In contrast, essentially all the cells were mROS positive before there is a significant loss in loss in BL  $\Delta\Psi_m$ . The losses in  $\Delta\Psi_m$  were nearly parallel with 50% of cells showing a loss in  $\Delta\Psi_m$  for the PFL and BL at about 12 pulses 20 pulses. Thus, the PFL was more sensitive than BL for loss of  $\Delta\Psi_m$  but there were no differences between the two pulsers in pulse number for mROS production. The difference in the response thresholds of  $\Delta\Psi_m$  and ROS indicates that the ROS mechanism is not directly linked to the  $\Delta\Psi_m$  mechanism. This disparity in response solely attributable to the pulse condition is noteworthy.

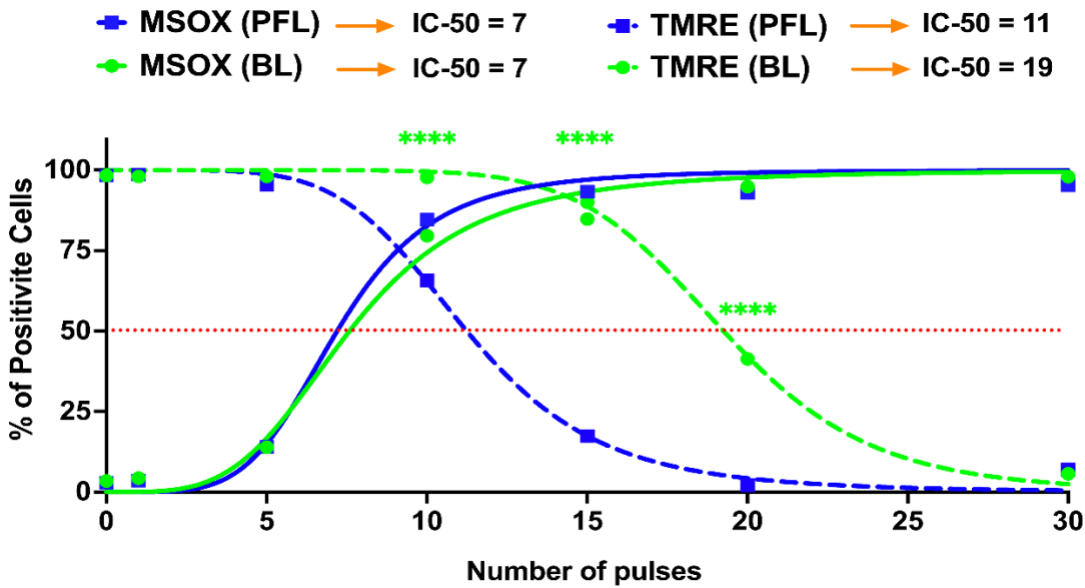


**Figure 10.** nsPEF effects of BL and PFL pulsers on the reactive oxygen species and mitochondria membrane potential at 20 min after pulsing. B16F10 cells were exposed to different pulsing numbers with BL or PFL (green and blue color code respectively) with a fixed electric field of 40 kV/cm. Dotted lines represent the TMRE and solid lines represent the MSOX. The IC-50 is mentioned at the top. Significant differences were observed between these two pulsers in regard to a decrease in mitochondrial membrane potential (at 10, 15, and 20 pulses), indicated by the (\*\*\*\* with  $p < 0.0001$ ) [45].

#### 2.4.9 PFL but Not BL Caused a Decrease in Maximal OCR and Spare Respiratory Capacity (SRC)

Figure 11 shows the metabolic effects of PFL and BL nsPEFs on oxygen consumption rate (OCR) using the Seahorse. Cells were treated with nsPEFs and then incubated until they were attached, as required for analyses. A look at responses that were measured after 5 pulses within the first 30 min after pulsing indicates that there was no ROS production or loss of  $\Delta\Psi_m$  (Figure 10). no PI uptake or no loss in tPMET (Figure 5), and no loss in viability after 24 h post

pulse (Figure 6). However, for the PFL, there was an increase in tPMET. Seahorse results show that there was no significant decrease in basal OCR 15 h after nsPEFs with either pulser. However, after FCCP (uncoupling agent) treatment, the PFL treatment resulted in a significant decrease in maximal OCR and a decrease in spare respiratory capacity (SRC) determined by FCCP OCR minus basal OCR. BL pulses led to a slight but insignificant increase in SRC. The SRC reflects the mitochondria's ability to fulfill additional energy requirements beyond the basal level in response to acute cellular stress. Thus, PFL pulsers show differences in responses to maximal OCR and SRC that are not present in the BL pulser and not present in basal conditions for either pulser occur 15 h after nsPEF treatment.

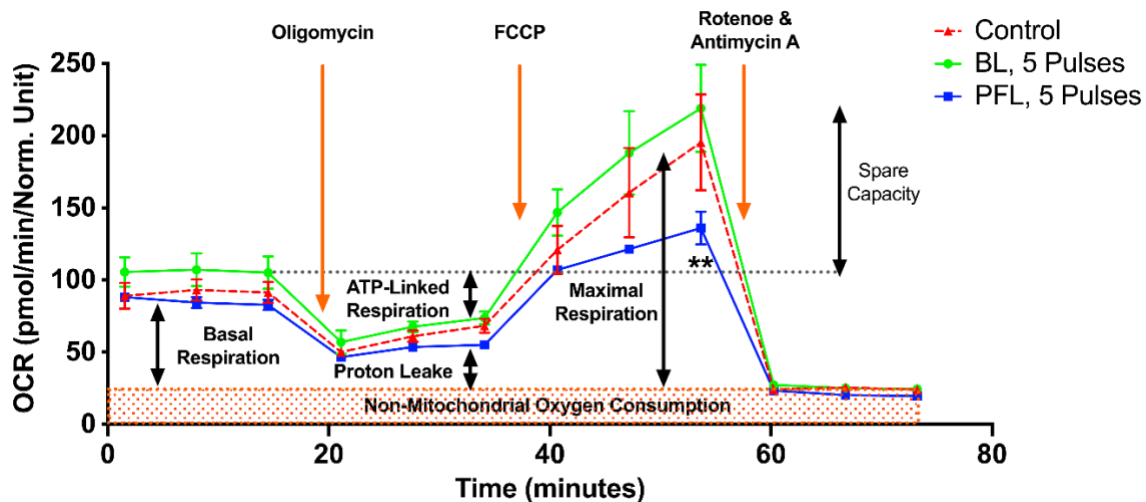


**Figure 11.** nsPEF effects of BL and PFL pulsers on mitochondrial oxidative metabolism in B16F10 melanoma cell lines. The oxygen consumption rate (OCR) of cells was measured 15 h after pulsing with 5 pulses. The x-axis represents time (up to 75 min), which aligns with the recommended test profile in the Seahorse assay for measuring mitochondrial respiration. The electric field was maintained at 40 kV/cm for both pulsers. The cells were maintained at 37 °C

during the 15 h while they adhered. The different states of mitochondrial respiration are indicated: basal respiration (Basal), proton leak (respiration after oligomycin exposure), maximal respiratory capacity (respiration after FCCP, MRC), and non-mitochondrial respiration (after rotenone and antimycin A) (NM). \*  $p < 0.05$  compared to control. Cells treated with PFL pulses showed a lower SRC compared to the control group (\*\*  $p < 0.002$ ) [45].

#### **2.4.10 Effect of an antioxidant Trolox on nsPEFs-induced loss of $\Delta\Psi_m$ and increases in ROS**

As shown in Figure 12, the dissipation of the  $\Delta\Psi_m$  and increase in mROS are inversely proportional with increased pulsed number. Thus, it is not possible to determine if an increase in ROS causes a decrease in  $\Delta\Psi_m$  or if a decrease in  $\Delta\Psi_m$  causes an increase in ROS. In any event, correlation does not imply causation. Therefore, a closer look was necessary to determine the effects of these two variables. Figure 12 shows studies with mitochondrial ROS (mROS) determined with MitoSox and the  $\Delta\Psi_m$  determined with TMRE in the presence and absence of the antioxidant Trolox. The increasing charging effects of nsPEF were achieved by increasing the pulse number with PFL pulser (40 kV/cm electric fields).

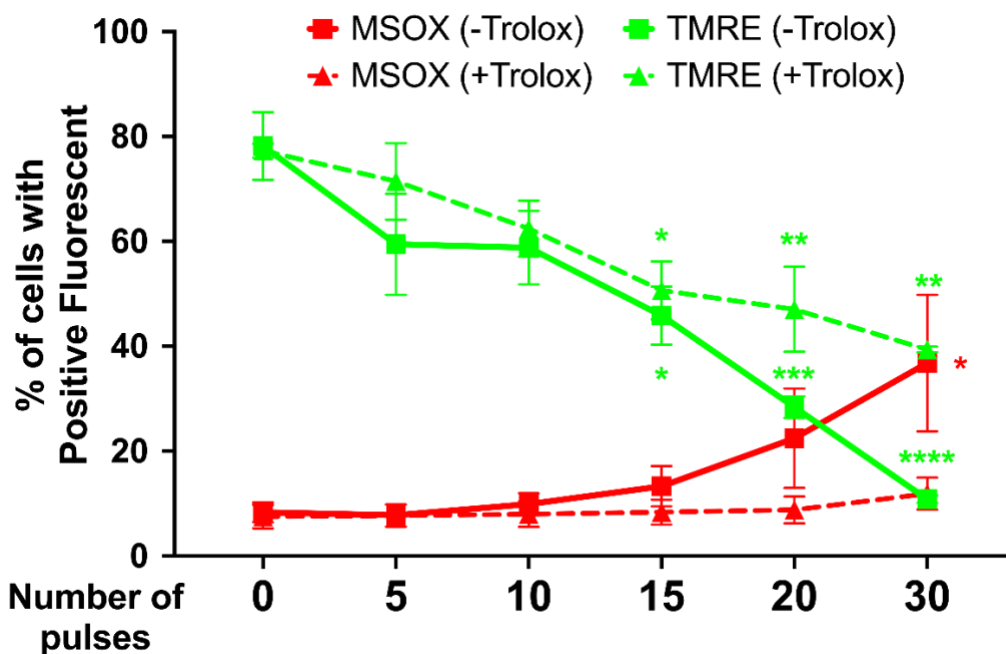


**Figure 12.** The independence of mitochondrial membrane potential and ROS dynamics in response to nsPEF exposure. Flow Cytometric Analysis of Mitochondrial Membrane Potential and Mitochondrial ROS Levels in H9C2 Cells Exposed to nsPEFs, with and without Trolox Antioxidant Treatment. Flow cytometry analysis of H9C2 cells stained with 0.3  $\mu$ M TMRE to measure mitochondrial membrane potential and 2  $\mu$ M MitoSOX to assess mitochondrial ROS levels. Quantification of MMP and mitochondrial ROS levels in H9C2 cells following exposure to nsPEFs (40 kV/cm, 60 ns, 1 Hz), with or without Trolox antioxidant treatment. Cells were incubated with Trolox for 35 minutes, and data were collected 20 minutes post-pulsing (optimized time based on microscopy experiments). Experiments were performed in triplicate, and statistical significance was determined by two-way ANOVA analyzed with GraphPad Prism software (\* $p < 0.05$ , \*\* $p < 0.01$ , \*\*\* $p < 0.001$  \*\*\*\* $p < 0.0001$ ).

The nsPEF threshold for a significant loss of  $\Delta\Psi_m$  was 15 pulses, and there was no significant effect of Trolox to inhibit that loss. There was also no significant increase in mROS at

that nsPEF charging level. The threshold for an increase in mROS was 30 pulses when  $\Delta\Psi_m$  had already decreased. Both responses were sensitive to Trolox at 30 pulses. These studies suggest that the decreases in  $\Delta\Psi_m$  are independent of increases in mROS, but that the increase in ROS occurred later and could be related to the decreases in  $\Delta\Psi_m$ .

#### **2.4.11 NsPEFs and Rotenone act synergistically for ROS production indicating distinct sites of action in the ETC**

Since rotenone and nsPEF act at complex I, it was of interest to determine their effects on ROS production. NsPEFs induced ROS and since rotenone is known to act at Complex I it was of interest to determine if any further information about their mechanisms of action could be gleaned if they were tested alone and in combination for ROS production. Figure 13 shows that rotenone and nsPEFs act synergistically to increase ROS in H9c2 cells. As the charging effect of nsPEFs was increased from 5 to 20 pulses, there was an increasing in the synergism quotient (sum of effects alone over combined effects) from 1.6 to as high as 2.36. Since rotenone is known to act at subunit ND1 at the transition of electrons from FeS complex to Ubiquitone, nsPEF are expected to act at another site in complex I and/or elsewhere.

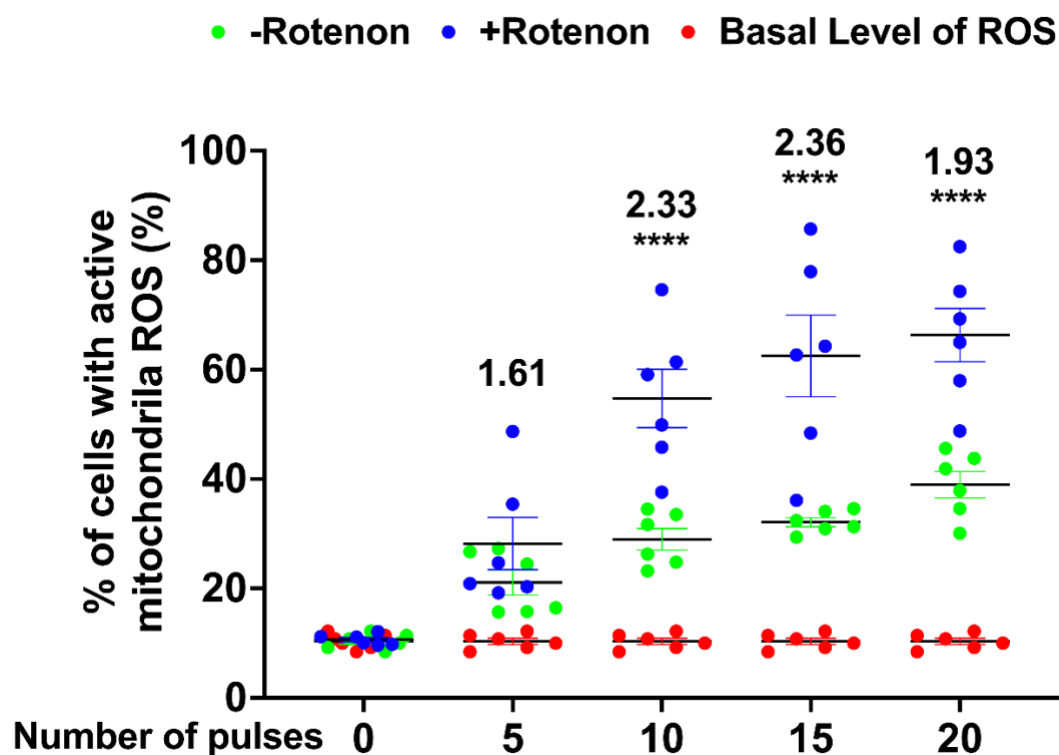


**Figure 13.** Synergistic ROS Generation by Rotenone and nsPEFs Reveals Distinct Sites of Action in Mitochondrial Electron Transport Chain Complex I. Flow cytometry analysis of H9C2 melanoma cells exposed to 2  $\mu$ M Mitosox, either alone or in combination with 30  $\mu$ M Rotenone, with different pulsing conditions (40 kV/cm, 60 ns, 1 Hz). Cells were analyzed 20 minutes after treatment. Differential impact of nsPEFs (40 kV/cm, 1 Hz, 60 ns duration) and Rotenone on ROS production in H9C2 melanoma cells. While nsPEFs and Rotenone individually elevate ROS levels, their combined application results in a synergistic ROS increase, suggesting independent actions at different sites within Mitochondrial Electron Transport Chain Complex I. Each data point represents percent of cells with active mitochondrial ROS from flow cytometry analysis, and error bars indicate standard deviation. Experiments were performed in triplicate, and statistical significance was determined by two-way ANOVA analyzed with GraphPad Prism software (\*\*\*\* $p < 0.0001$ ).

## 2.5 Discussion

These studies show that nanosecond pulses generated by commonly used pulse generators (PFL and BL) with the same pulse duration and essentially the same electric field and frequency distributions can result in different cell responses owing to distinct post-pulse waveforms determined by their dissimilar circuit topology. These subtle post-pulse waveform differences, which have been overlooked, can have a significant impact on functional outcomes. Specifically, the PFL post-pulse waveform was unipolar, while the BL pulse was bipolar. For instance, at 4 kV, the PFL pulse exhibited a small post-pulse waveform (5% of the main pulse, same polarity) lasting approximately 2  $\mu$ s. Conversely, the BL pulse had an even smaller post-pulse waveform (1-2% of the main pulse, opposite polarity) but lasted longer ( $\sim$ 50  $\mu$ s). These post-pulses were a result of their electrical configurations being unique. In the PFL configuration, the load (cells in cuvette) was isolated from the charging circuit by a switch. After the switch closed, allowing the 100 ns pulse current flow, there was a brief charging current from the high voltage power supply. However, this current stopped quickly as the switch recovered and isolated the load from the charging circuit. The recovery process occurred on a scale of 2  $\mu$ s, much shorter than that of a conventional spark gap switch [49]. This could be attributed to the small energy involved (100 mJ) and the short pulse duration (100 ns), whereas a conventional spark gap switch can handle  $>10$  J and conduct for  $>1$  ms. In our case, the discharge mode might involve a streamer-arc channel without significant heating of the ambient air, allowing for a rapid switch recovery. On the other hand, in the BL configuration, the load was continuously connected to the BL and remained in the charging loop regardless of the switch state. A small charging current was present throughout the charging time until the BL was fully charged before the next pulse (Figure 1a).

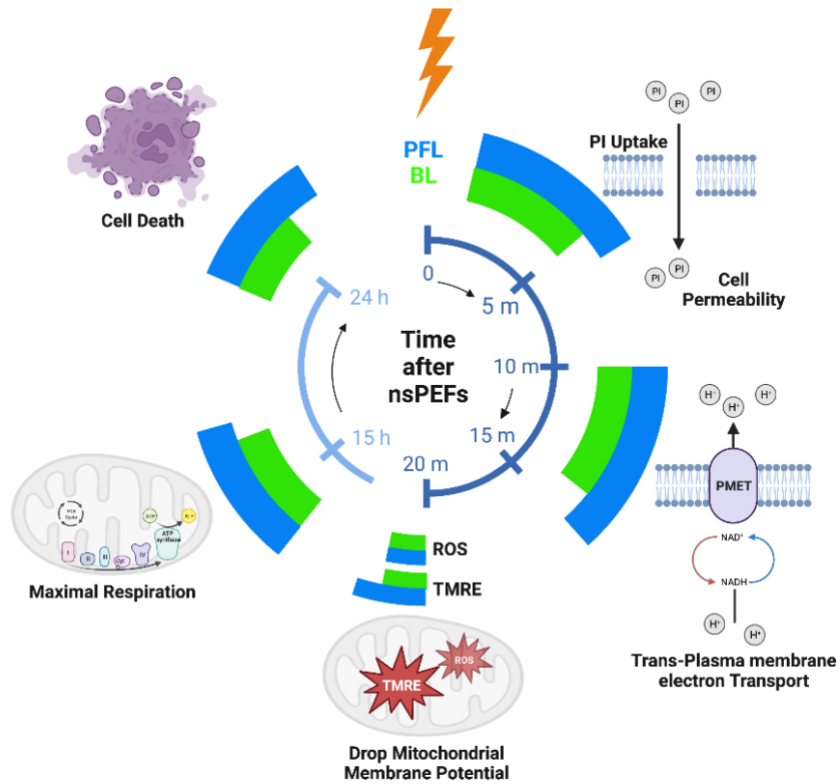


**Figure 14.** The timeline of the cell responses to PFL and BL pulses at different time intervals: 10-50 mins, 15 hours, and 24 hours after pulsing. The magnitude of cell responses is represented by the extension of azimuthal angles (larger angle meaning larger response). Created with BioRender.com [45].

The distinction in cell responses to PFL pulses and BL pulses, as summarized in Figure 14, can be attributed to the differences in their post-pulse condition. During the main pulse interval, the frequency contents, charges, and energy of both types of pulses were almost identical, with some cases where the BL pulses exceeded the PFL pulses. However, in the post-pulse interval, compared to the BL post-pulses, the PFL post-pulses demonstrated a longer duration effect on the OMP and had a lesser impact on the IMP established by the main pulse, (Figure 4). Given that the MP created by the main pulse leads to membrane pore formation,

Ca<sup>++</sup> influx, and other effects, it would be expected to elicit a stronger cell response for holding longer. Therefore, it is not surprising that the PFL pulses generally demonstrated greater potency than the BL pulses.

The main pulse waveforms of PFL and BL, which are nearly identical in charge and spectrum, can induce similar membrane and intracellular effects. For example, the charging of the cell's outer membrane can lead to an amplified electric field across it, resulting in pore formation and increased membrane permeability. However, the subsequent post-pulse current can modify the membrane potential by neutralizing the charges that have accumulated across the membrane. This effect is particularly pronounced in the case of BL pulses, which have an opposite post-pulse current. The charge of the main pulse was estimated as  $-40 \mu\text{C}$  ( $-4\text{kV} \times 100\text{ns}/10\Omega$ ), which is close to the measured value of  $-50\mu\text{C}$  presented in Fig.1c. On the other hand, the charge flowing during the post-pulse can be calculated by integrating over the post-pulse waveform to be  $75 \mu\text{C}$ . This accounts for the same magnitude of the charge of the main pulse charge, which would have reduced the membrane charging established by the main pulse, and it would certainly cause a significant change in both the OMP and the IMP, as indicated in Fig.4. In contrast, in the case of PFL pulses, the post-pulse current does not significantly alter the membrane potentials initiated by the main pulse. However, it is possible that the potential could be slightly larger due to the same polarity of the post-pulse, which serves to maintain the charging of the membranes.

However, in addition to plasma membrane electroporation as PI influx, nsPEFs also shows a unique electric field modulation of a well-known but seldomly discussed activity of the plasma membrane redox system (PMRS) function of tPMET, which plays a crucial role in safeguarding cells against intracellular oxidative stress, maintains redox balance, and regenerates

NAD<sup>+</sup> for glycolysis[88]. Notably, in contrast to the BL pulser showing only a decrease in nsPEF-induced tPMET, the effect of the PFL induced a biphasic effect with an increase in tPMET at lower electric field conditions before any PI influx appeared and an inhibition of tPMET at higher electric fields where PI influx demonstrated PM EP. So, the presence of PM pores was coincident with the loss of tPMET for both PFL and BL. Although coincidence is not an indication of the cause, it does raise the question of the relationship between nsPEF-induced PM permeabilization (pore formation) and tPMET. Nevertheless, the increase in tPMET appears to be independent of PI permeability. However, it is possible that molecules smaller than PI, such as Ca<sup>2+</sup> could gain entry at lower nsPEF conditions through pores smaller than PI [9]. Overall, for effects on the PM, the PFL has a greater sensitivity or lower pulse number threshold for all three PM effects on the PI influx, gain and loss of tPMET activity.

Having seen these differences between the PFL and the BL pulsers, it was of interest to see the effects on cell viability. While effects depend on different factors, in all studies of nsPEFs no cell line or tumor type has shown resistances to nsPEF elimination. Two models have shown vaccine effects as vaccinations[20, 92, 93], meaning that tumor-free animals are resistant to regrowing the treated cancer again. In the viability studies, like that seen for the PM responses, the PFL had a lower IC<sub>50</sub> value for viability than the BL pulser, as shown by requiring fewer pulses and requiring a lower electric field. This is interesting because all the nsPEF pulsers in those studies were BL constructions. Although the construction of a PFL for studies is less practical than the BL construction because of half-charging voltage output, it would be interesting to determine if a PFL pulser would require lower electric fields or fewer pulses for tumor elimination and be more effective for inducing immunity and vaccination.

Having shown that nsPEFs cause a dissipation of the mitochondrial membrane potential ( $\Delta\Psi_m$ )[9], we were curious to determine what caused this loss of  $\Delta\Psi_m$ . One obvious possibility was that like nsPEF effects on the plasma membrane, they could also permeabilize the inner mitochondrial membrane (IMM). However, another way that the nsPEFs could cause a loss of the  $\Delta\Psi_m$ , is through opening the mitochondrial permeability transition pore (mPTP). When we saw that the nsPEF-induced loss of  $\Delta\Psi_m$  was enhanced by  $Ca^{2+}$ [9], we considered that membrane permeabilization does not require  $Ca^{2+}$  and further that  $Ca^{2+}$  effects are essentially always mediated through a protein. Therefore, we hypothesized that nsPEF-induced loss of  $\Delta\Psi_m$  was not due to permeabilization of the IMM but more likely due to opening the mPTP, a hypothesis yet to be proved. Although the identity of the mPTP has been controversial, it has recently been proposed that the mPTP is a dimer of the F<sub>0</sub>F<sub>1</sub> ATP synthase [94, 95] and that  $Ca^{2+}$  binding to F-ATP synthase  $\beta$  subunit triggers the mitochondrial permeability transition[96]. This is consistent with the role of  $Ca^{2+}$  to enhance the dissipation of the  $\Delta\Psi_m$ .

ROS is a well-known activator of the mPTP and disturbances in  $Ca^{2+}$  and oxidative stress are tightly coupled for opening the mPTP. nsPEF induces the production of ROS with no distinctions between the PFL and the BL pulsers. These observations that nsPEF-induced ROS and that the elevation of ROS was enhanced in the presence of  $Ca^{2+}$  have heightened our attention to determining the roles of nsPEF-induced ROS in mPTP opening. Although there is no established direct role of ROS in opening the mPTP, ROS has effects that indirectly influence opening the mPTP. Many factors determine the probability for opening the mPTP including  $Ca^{2+}$ ,  $\Delta\Psi_m$ , and the redox state of mitochondrial components, which can be influenced by ROS[97]. Many SH reagents were among the strongest stimulators of permeability transition, so it was proposed that thiol groups on some protein(s) played roles in opening the mPTP [98]. It

was proposed that the mPTP is modulated by the redox state of pyridine nucleotides and glutathione at two independent sites, one of which could be the adenine nucleotide translocase (ANT)[99]. Although the protein structure of the mPTP is still not defined, cyclophilin D (CypD) is a well-characterized regulator of the mPTP. CypD has also been shown to be redox regulated by forming an intramolecular disulfide with a conformational change playing a major role in cell necrosis by opening the mPTP acting as a redox-sensor protein in mitochondria [100].

In many of our studies, we have monitored the dissipation of the  $\Delta\Psi_m$  in response to nsPEFs in the presence of  $Ca^{2+}$  and ROS indicators, and antioxidants to determine roles for  $Ca^{2+}$  and ROS in  $\Delta\Psi_m$ . Fig. 7 is one of those studies using TMRE to determine changes in the  $\Delta\Psi_m$  and MitoSox (MSOX) to monitor mitochondrial ROS (mROS) changes in response to the PFL and BL pulsers. Interestingly the results indicate that ROS plays different roles for the loss of  $\Delta\Psi_m$  depending on the pulser. The pulse number-dependent increase in ROS is essentially the same with both pulsers showing a significant increase in mROS between 5 and 10 pulses and a maximum at 15 pulses. In contrast, the loss of  $\Delta\Psi_m$  is different between the two pulsers.

So, the relationships between mROS and loss of  $\Delta\Psi_m$  are dissimilar between the two pulsers. What is similar between the two pulsers with the other cell responses is that compared to BL responses, PFL responses are more sensitive for dissipation of  $\Delta\Psi_m$ , loss of cell viability, PI permeability, activation of tPMET activity, and loss of tPMET activity. In contrast to all these cell responses, nsPEF-induced ROS production is the same for both PFL and BL pulsers. This suggests that the nsPEF-induced loss of  $\Delta\Psi_m$  is relatively independent of the production of ROS.

In another approach for analyzing these pulsers on biological responses, we evaluated metabolic responses using the Seahorse to determine nsPEF effects on oxygen consumption rate

(OCR) in control (sham-treated) and nsPEF-treated cells with 5 pulses from each of the PFL and BL pulsers. The 5-pulse condition did not cause any cell death, PI permeabilization, increase in ROS, loss of  $\Delta\Psi_m$ , or loss of tPMET activity with either pulser. However, the 5-pulse treatment did induce an increase in tPMET activity with the PFL but not the BL pulser. It should be noted that except for cell death, all these cell responses were determined within  $\leq 30$  min after treatment. Yet 15 h after treatment there were no significant differences in basal OCR with either pulser. With the increase in OCR after the addition of the FCCP uncoupling agent, the BL OCR was not significantly different than the control while the PFL treatment exhibited a significant decrease in OCR compared to the control and the BL response. The spare respiratory capacity (SRC) of the cells (FCCP minus basal OCR), was lightly increased with the BL pulser but significantly decreased in the PFL, which was due to the attenuated FCCP response and independent of the basal OCR. This suggests that there was a time-dependent deterioration of the status of the mitochondria presumably in response to cellular stress and the ability to fulfill additional energy requirements beyond the basal level in response to acute cellular stress. While there was not a significant increase in ROS in the 5-pulse condition, ROS likely increased during the 15 h time it took the nsPEF-treated cells to bind to the Seahorse plate for OCR analysis. Given that the increased ROS response was the same for both pulsers and only the response to the PFL showed a decreased SRC, any hypothesized increase in cellular ROS would be expected in the response to the PFL and not the BL. However, other stress response signaling pathways could have been activated that were not analyzed such as activation of the mitogen-activated protein kinase (MAPK) pathway and the nuclear factor kappa-light-chain-enhancer of activated NF- $\kappa$ B pathway, which could also have been activated during the 15 h post nsPEF exposure to the PFL pulser [101]. These MAPK-NF $\kappa$ B stress pathways could have caused a deterioration of

mitochondrial SRC, but this would have occurred in the PFL but not the BL pulser. Given that the PFL induced more sensitive responses than the BL, this could have resulted in a selective response of these stress pathways from the PFL, like that for the increase in tPMET. However, these are speculations since we did not analyze these enzymatic stress responses. Nevertheless, the differences in the metabolic response to the PFL and BL pulses provide another example of selectivity for a biological response from different nsPEF post-pulse waveforms.

We previously published a conformation that a fast or short pulse rise time of the primary pulse was an important feature for inducing intracellular effects[9]. We were not cognizant at that time about roles for a post pulse, yet both fast and slow rise time pulsers were based on PFL design. Those studies showed that faster rise times vs. slower rise times were more effects to dissipate the  $\Delta\Psi_m$  and induce cell death while effects for  $Ca^{2+}$  or PI influx through the plasma membrane were not dependent on the pulse rise time. The present studies show yet a different way that nsPEF waveforms can have different and selective effects on cell responses. As indicated here, these different or selective effects have nothing to do with the primary pulse like the rise time studies just discussed but are related to the effects the post-pulse waveforms have on the primary pulse.

Regardless of the different primary pulse waveforms based on their rise times or the post-pulse waveforms based on dissimilar circuit topology, these results show that dissimilar nsPEF waveforms can have distinctive and possible selective biological outcomes that can determine cell fate. Given that nsPEFs produce ROS and ROS are endogenous signaling molecules, it is most likely that nsPEF waveforms at the lower pulse conditions will have a greater impact on physiological functions while higher pulse conditions will be more typical of pathological

conditions or for regulated cell death mechanisms. It is also possible that these nsPEF waveforms will initiate other non-ROS cellular responses.

Furthermore, in Figure 11, the impact of 5 pulses on mitochondrial oxygen consumption is shown. The PFL pulser showed a significant decrease in spare respiratory capacity (SRC) by reducing maximal respiration without affecting the basal respiratory level. This observation indicates a disruption in the ETC and/or proton transport across the inner mitochondrial membrane [102]. These findings are consistent with the notion that glycolysis-derived pyruvate oxidation is involved in maintaining SRC levels, which supports the stimulating effect observed on tPMET (Figure 5). In contrast, the BL pulser led to high SRC levels, a characteristic often associated with cancer cells that are resistant to targeted agents. This can be attributed to the fact that the low pulse number (5 pulses) in this experiment was insufficient to cause significant pore formation and promote the loss of the  $\Delta\Psi_m$ .

There have been previous studies that involved the deliberate introduction of post-pulses to investigate cell responses. One phenomenon that has been observed is NBC [29, 103, 104], where a reversed-polarity nanosecond pulse can reduce the cell responses caused by a preceding ns pulse. The underlying mechanisms for NBC are still not fully understood and may involve assisted membrane discharge, a two-step process of charge transfer, an alternating reduction and oxidation mechanism, as well as cation diffusion reversal. These mechanisms are more pronounced when the second pulse is of similar magnitude as the first pulse. In another study [105], a double pulse strategy has been used for electroporation, where a high voltage short pulse is used for electroporation and a low voltage long pulse facilitates drug delivery through electrophoresis. Bipolar pulses with high frequency characteristics have also been employed for irreversible electroporation (HFIRE) [106, 107], with the reversed polarity pulses used to

suppress or remove muscle twitching by exploiting different time constants between electroporation and muscle excitation [108]. In these studies, the post-pulse to main pulse ratios were much larger compared to our study. For example, in BPC, the best cancellation efficiency was observed when the reversed pulse magnitude was 50% of the first pulse. In HFIRE, the first pulse was delivered at a higher amplitude than subsequent pulses, but it was common for the second pulse to be equal to the first phase. In the double pulse strategy, the second pulse was also 10% to 100% of the first pulse. In our study, the magnitude of the post-pulse was less than 5% of the main pulse and determined by dissimilar circuit topology differing between the two designs, yet it still resulted in disparate cell responses. This suggests that a mechanism like electrophoresis may be involved in cells responding to the post-pulse. Further investigation into the mechanisms, specifically in the realms of electrokinetics and bioelectrochemistry, may help elucidate the underlying processes that have often been overlooked in pulse engineering.

## **2.6 Conclusions**

In the studies here, two different 100 ns pulses generators were used providing 100 ns pulse durations and electric fields of 40 kV/cm primary pulses with similar voltage and frequency wave distributions. One was a PFL with a post-pulse waveform having the same polarity as the primary pulse and the other was a BL pulses with a post-pulse waveform having an opposite polarity as the primary pulse. The cell responses obtained from these distinct pulse generators were determined from their post-pulse waveforms, not their primary waveforms.

Cells exhibited greater sensitivity to the PFL than the BL pulser with lower pulse numbers or electric field intensities for inducing cell membrane permeability, dissipation of  $\Delta\Psi_m$ , a decrease in mitochondrial SRC, a biphasic effect on tPMET, and eventual cell death. This biphasic behavior holds significant implications for enhancing the efficacy of ablation

procedures and potentially facilitating cellular differentiation in cancer therapy, ultimately leading to the prospect of in-situ vaccination. Interestingly, both pulse types demonstrate a similar dependence on pulse number in terms of ROS production. Despite the post-pulse having a magnitude of less than 5% of the main pulse and lasting for a longer duration (50  $\mu$ s), its low intensity is still expected to decrease the membrane potential caused by the main pulse. To the best of our knowledge, this is the first time that charging current, which is reflected as a post-pulse, has been reported to have such a significant effect on cellular response. This work highlights the importance of considering the charging characteristics in pulse generator design and when comparing cell responses under similar pulse conditions.

## CHAPTER 3:

### **Enhancement of nano-second Pulse Electric Fields (nsPEFs) on Treatment of Murine Melanoma with Multiwalled Carbon Nanotubes (CNTs)**

#### **3.1 Introduction**

Melanoma, a form of skin cancer, ranks as the sixth most prevalent malignancy and accounts for approximately 1.7% (or 232,100 cases) of all cancer instances worldwide. The incidence of melanoma is increasing in developed nations, primarily those with predominantly fair-skinned populations. In North America in 2012, there were 13.8 cases of cutaneous melanoma per 100,000 person-years when age-standardized to the world standard population. This disease results in 55,500 deaths annually, comprising about 0.7% of all cancer-related fatalities [109].

The treatment strategy for melanoma patients encompasses a range of approaches, including surgery, chemotherapy, radiation therapy, immunotherapy, and targeted-based therapy. The choice of therapy, whether single or a combination, depends on various factors such as the patient's condition, the stage of the tumor, and its location. However, despite the availability of diverse treatment options and extensive clinical trials spanning four decades, the overall treatment approach has proven to be insufficient and, unfortunately, largely ineffective [110].

Addressing the challenges in cancer therapy demands innovative methods, and pulsed power technology has garnered attention for its distinctive effects on tumor

growth and its potential to induce immunity in rodent models, including rat liver and mouse mammary cancer [33-35]. This raises the possibility of nsPEFs as a form of immunotherapy, subject to further exploration and development. By employing high power and low energy, nanosecond pulses can breach the outer plasma membrane of cells while simultaneously impacting vital intracellular structures and functions [31]. This distinctive mechanism holds promise for pioneering immunotherapeutic interventions [12]. NsPEFs have demonstrated a multifaceted impact on cancer. They are not only effective in ablating various types of tumors, whether they are in their original locations (orthotopic) or have spread to other sites (ectopic) in rodents and humans [111], but they also induce immunogenic cell death [34, 71], activate T-cell-dependent immune responses, stimulate innate immunity, reverse immunosuppression, and have the potential to convert tumors into in-situ vaccines[35]. This highlights the exciting potential of nsPEFs in the field of cancer therapy and immunotherapy. However, it is important to note that not all tumor models respond equally to nsPEFs regarding immune induction and in-situ vaccination. The mouse B16f10 melanoma model, for instance, presents unique challenges in this context [112].

The limited efficacy of anticancer treatments may be attributed to the restricted coverage of the electric field. Notably, the PFL pulse generator exhibited superior efficacy in ablating B16-F10 melanoma cells in an in vitro setting, while also demonstrating a better result in tumor ablation and effect intracellular effect [45]. Guo et al. used the PFL (5–10 pulses, 60 ns, 50 kV/cm and 1 Hz) to stimulation of bone marrow-derived DCs (BMDCs). Supplementary data showed the activation of dendritic cells (DCs) in vitro after exposure to nanosecond pulsed electric fields (nsPEF), with

upregulation of MHC-II (IA/IE) and co-stimulatory molecules, CD86 and CD40, observed two days after DCs were co-cultured with NPS-treated 4T1 cells [34]. However, it is important to acknowledge a limitation in the application of the PFL pulse generator for in vivo studies, as it necessitates higher voltage levels when compared to the BL pulse generator. This increased voltage requirement raises clinical concerns that warrant careful consideration.

Multi-walled carbon nanotubes (MWCNTs), a novel type of carbon material, have demonstrated field emission capabilities, which have opened up a wide range of potential applications due to their high aspect ratio and excellent conductivity [41]. CNTs possess unique electronic properties that enable them to amplify the electric field near their tips, generating localized high-field regions [113]. Additionally, the rotational motion and torque ( $\tau$ ) induced by CNTs can enhance the impact of nanosecond pulsed electric fields (nsPEF) by aiding the penetration of the nanotube through the plasma membrane [114]. When combined with low-intensity electric pulses, CNTs result in a stronger electro-response [115]. Furthermore, carbon nanotubes have exhibited the ability to target cancer cells both passively and actively, leading to substantial uptake in tumors [116].

Given these promising properties, MWCNTs were employed to enhance the effects of nsPEF in a B16F10 melanoma cancer model. The objective of this study was to investigate the combined effects of multiwalled carbon nanotubes when used in conjunction with nsPEF treatment for melanoma. The study employed the B16F10 melanoma cell line as an in vitro and in vivo model. The ultimate goal is to expand the scope of these findings and create potential applications for the Pulse Forming Line (PFL) pulse generator in future in vivo studies. The aim is to reduce the required electric field

strength through the incorporation of MWCNTs and develop innovative and effective strategies for melanoma immune therapy, with the ultimate objective of in-situ vaccination (ISV). Ultimately, this research may pave the way for the translation of this combined approach into preclinical and clinical settings, potentially revolutionizing the management of this devastating disease.

## **3.2 Backgrounds and significance**

### **3.2.1 Carbon nanotubes (CNTs)**

Carbon nanotubes (CNTs) are synthetic allotropes of carbon. Allotropy refers to the ability of chemical elements to exist in multiple structural forms. For carbon, three naturally occurring allotropes are known, including diamond, graphite (comprising several layers of graphene), and amorphous carbon (a non-crystalline form of carbon) [117]. In addition to these natural forms, several synthetic carbon allotropes have been discovered. These synthetic carbon allotropes include fullerene (a structure resembling a sphere made of carbon atoms) [118], graphene (a single layer of graphite) [119] and carbon nanotubes (cylinders made by rolling up graphene layer(s)) [120].

Morphologically, carbon nanotubes can be described as cylinders that are nanometers in width and vary from nanometers to micrometers in length. They are composed of graphene sheets rolled up into the form of single or multiple concentric layers. When formed from a single layer, they are known as single-walled carbon nanotubes (SWNTs), while those composed of multiple concentric layers are referred to as multi-walled carbon nanotubes (MWNTs) [121].

### 3.2.2 Cellular Uptake Mechanisms of CNTs

Pristine or unmodified CNTs are inherently hydrophobic, which means they have low solubility and a tendency to aggregate in aqueous environments. The aggregation of CNTs is primarily driven by non-covalent interactions between the nanotubes, such as  $\pi$ - $\pi$  stacking involving the aromatic rings of adjacent nanotubes. Therefore, it became crucial to develop chemical strategies to enhance the biocompatibility of CNTs by improving their dispersion and solubility in physiological fluids. The chemical approaches used to functionalize CNTs can be categorized into two main types: covalent and non-covalent functionalization [122, 123].

CNTs have demonstrated a remarkable ability to penetrate various types of cells [124-126]. It is well-documented that the efficiency and uptake pathway of CNTs heavily depend on their morphology and surface chemistry. For instance, in a study conducted by Cherukuri and colleagues, they employed the intrinsic near-infrared fluorescence of SWNTs to investigate their cellular uptake. They found that the uptake of pristine SWNTs, which were dispersed in Pluronic surfactant, by mouse macrophage cells in vitro was significantly reduced when the cells were incubated at 27°C compared to 37°C. This observation suggested an endocytosis-dependent mechanism for the uptake of SWNTs [127].

Conversely, other studies have suggested that the cellular uptake of CNTs primarily occurs through passive diffusion across the cell membrane. Pantarotto et al. conducted research showing that amine-functionalized SWNTs enhanced the internalization of fluorescently labeled peptides by human 3T6 fibroblasts when incubated at 37°C [128]. This was determined through epifluorescence microscopy,

which also revealed the presence of SWNTs in the cell nucleus. Importantly, inhibiting the cell's metabolic functions by incubating it at 4°C or treating it with sodium azide did not impact the cellular uptake of SWNTs, suggesting an energy-independent mechanism for cell entry. The ability of CNTs to penetrate the cell membrane, resembling nano-needles, could be explained by a theoretical nanosyringe mechanism simulated by Lopez et al. for nanotube insertion into the lipid bilayer [44]. Molecular dynamics studies by Lopez and colleagues demonstrated that a hydrophobic nanotube with hydrophilic tips initially adsorbs horizontally onto a model membrane. Subsequently, the nanotube spontaneously changes its orientation from horizontal to vertical alignment, forming a transmembrane pore-like orientation through the bilayer. After insertion into the membrane bilayer, translocation to intracellular compartments can occur, as reported by Pantarotto et al.

In another study, further investigation of the energy-independent uptake of functionalized MWNTs was conducted. Confocal microscopy images revealed the internalization of fluorescently labeled and amine-functionalized MWNTs by fungal and yeast cells [129]. Notably, these prokaryotic cells, which typically lack the ability to perform active processes like endocytosis, internalized the functionalized MWNTs. This highlighted the use of mechanisms other than endocytosis for cell entry. Additionally, when Jurkat leukemic T cells were incubated with functionalized MWNTs at 4°C in the presence of sodium azide, the cellular uptake of MWNTs was not inhibited, confirming the involvement of a passive cellular uptake mechanism. The varying mechanisms of CNTs' cellular uptake reported by different authors could be attributed to the properties of the CNTs used in these studies, including their degree of individualization and

dispersibility in the cell culture media, which is highly dependent on the CNTs' functionalization density.

Mu et al. conducted a study to investigate the uptake of functionalized MWNTs by HEK293 epithelial cells using transmission electron microscopy (TEM) [130]. Their research revealed that single MWNTs were observed penetrating the cell membrane. Meanwhile, bundles of MWNTs were found intracellularly, surrounded by endosomal membranes. The TEM images also showed single MWNTs being released from MWNT bundles entrapped in endosomes, with these individual nanotubes penetrating the endosomal membrane to enter the cytosol.

In summary, these studies suggest that CNTs can access intracellular compartments through more than one mechanism of cell entry. This diversity may be attributed to the length-to-width ratio of the CNTs, allowing these nanoneedle-shaped structures to passively penetrate the cell membrane using the hypothesized and experimentally demonstrated nanosyringe mechanism, in addition to active endocytosis mechanisms. However, it's worth noting that the disruption of endosomal membranes associated with CNTs' escape from endosomes could potentially induce cell damage. Such membrane disruption might activate the NLRP3 inflammasome, leading to pyroptotic cell death [131, 132].

### **3.2.3 Effect of chemical functionalization on CNTs**

Residual transition metal catalysts like iron, cobalt, or nickel present in pristine CNTs can catalyze the intracellular generation of free radicals, resulting in oxidative stress and cytotoxic effects. For example, exposure of HEK293 human kidney embryo cells to pristine SWNTs induced cell apoptosis and reduced cell proliferation [133].

Similarly, incubating human epithelial cells with pristine MWNTs significantly decreased cell viability [134]. However, chemically functionalized CNTs exhibit improved biocompatibility profiles compared to their pristine counterparts. This enhancement can be attributed to the chemical reactions applied to pristine CNTs, followed by thorough washing in organic solvents using bath sonication, which aids in the removal of metal catalysts adsorbed onto the CNT walls. Moreover, chemical reactions, such as bath sonication-assisted acid oxidation, create surface defects on the CNTs, helping to eliminate trapped metal catalysts [135].

Coccini et al. demonstrated that acid-oxidized MWNTs contained lower metal content and had milder effects on cell viability compared to pristine MWNTs when incubated with epithelial A549 cells at a concentration of 1  $\mu\text{g/ml}$  [136]. However, increasing the concentration of oxidized MWNTs in the culture medium led to a significant decrease in A549 cell viability. Vuković et al. reported that treating fibroblast L929 cells with pristine MWNTs at concentrations ranging from 3 to 12.5  $\mu\text{g/ml}$  significantly reduced cell proliferation, while incubation with carboxylic or amine-functionalized MWNTs did not exhibit this effect [137]. Nevertheless, the proliferation of L929 cells incubated with functionalized MWNTs at higher concentrations (25 to 100  $\mu\text{g/ml}$ ) was significantly lower than that of untreated cells. When human epidermal keratinocytes were exposed to acid-functionalized SWNTs, a dose-dependent reduction in cell viability was observed, accompanied by increased production of the pro-inflammatory cytokine IL-8 [138]. This observation might be attributed to the rupture of CNT-containing endosomes, leading to NLRP3 inflammasome activation and pyroptosis [131, 132].

It can be suggested that while chemical functionalization can enhance CNT purity and biocompatibility, the increased individualization of CNTs could lead to higher cellular uptake, potentially causing cytotoxic effects at elevated dosages. Similarly, Li et al. demonstrated that as the positive charge of chemically functionalized MWNTs was increased through surface chemistry manipulation, their cellular uptake by THP-1 cells (monocytic cell line) and BEAS-2B cells (bronchial epithelial cell line) was enhanced, resulting in the production of pro-inflammatory cytokines [139].

### **3.2.4 Biocompatibility of CNTs with immune cells**

The cytotoxic effects of CNTs on immune cells have been investigated in several studies. When human monocyte-derived macrophages were incubated with carboxylated SWNTs, it was observed that these nanotubes formed fewer intracellular aggregates and had lower effects on cell viability compared to pristine SWNTs [140]. Treatment of murine RAW 264.7 macrophages with pristine SWNTs resulted in significant depletion of glutathione, an oxidative stress biomarker, in contrast to carboxylated SWNTs treatment [141]. Additionally, the higher iron content in pristine SWNTs led to a significant increase in the formation of intracellular reactive oxygen species when incubated with rat NR8383 macrophages [142]. The length of CNTs was also found to influence biocompatibility, as longer pristine MWNTs (~13  $\mu\text{m}$ ) induced higher production of the inflammatory cytokine IL-1 $\beta$  in LPS-primed human primary macrophages compared to shorter MWNTs (1-10  $\mu\text{m}$ ) [132, 143].

Wang et al. investigated the effects of carboxylated-MWNTs on human monocyte-derived DCs and found that the treatment did not significantly decrease cell viability or increase the expression of CD80 or CD86 co-stimulatory molecules,

suggesting a lack of adjuvanticity of MWNTs [144]. However, cytokine production by MWNT-treated DCs was not assessed in this study. Dumortier et al. cultured mice-derived B or T lymphocytes in the presence of SWNTs functionalized using 1,3-dipolar cycloaddition reaction, which did not induce cell death, provoke cell proliferation, or stimulate IFN- $\gamma$  production [145]. Yet, SWNTs functionalized via acid oxidation and amide coupling reactions, showing lower aqueous dispersibility, stimulated the production of TNF- $\alpha$  and IL-6 by macrophages in vitro.

While the study highlighted the impact of surface chemistry and aqueous dispersibility of SWNTs on cytokine production by immune cells in vitro, it would be valuable to investigate the effects of different-sized SWNTs as well. Pescatori et al. reported that incubating carboxylated or amine-functionalized MWNTs with Jurkat T cell line or THP-1 monocytic cell line did not induce cell apoptosis [146]. However, the uptake of functionalized MWNTs by THP-1 monocytic cells, but not Jurkat T cells, led to increased production of pro-inflammatory cytokines IL-6 and TNF- $\alpha$ . On the other hand, Medepalli et al. found that DNA-functionalized SWNTs did not alter the cell phenotypes or activation marker expression when incubated with human blood-derived monocytes or lymphocytes. The observed discrepancies could be attributed to variations in CNT functionalization density, used doses, and incubation time. These studies suggest that increased purity and functionalization of CNTs may enhance their cytocompatibility, but it's important to consider that functionalized CNTs can still induce dose-dependent cytotoxic effects [147].

### 3.2.5 CNTs' biodistribution

Biodistribution and clearance of the CNTs are considered among the main obstacles' clinical application of CNTs is facing. The utilization of CNTs for the biomedical applications demanded studying their biodistribution to determine their organ accumulation and toxicity following systemic administration. Yang et al. have demonstrated that pristine SWNTs intravenously injected to KM mice were distributed mainly to liver, spleen and lung 24 hr post injection [148]. The pristine SWNTs were retained in these organs at high levels over a period of 28 days post injection. In addition, the pristine SWNTs were un-detectable in the urine or feces samples collected from injected mice, which further indicated the retention and accumulation of the injected pristine SWNTs in the mentioned organs.

The functionalization density of MWNTs affected their biodistribution and excretion following intravenous injection in BALB/c mice [149]. On comparing three types of In-radiolabeled MWNTs that were amine-functionalized to varying degree, the highest bladder accumulation and lowest liver retention detected at 0.5 hr and 24 hr post injection, respectively, were demonstrated by the MWNT that possessed the highest content of amine moieties. Thus, it was suggested that increasing the amine-functionalization density of MWNTs assisted their individualization, hence glomerular filtration, and renal clearance. However, other factors that are, theoretically, expected to affect the MWNTs biodistribution such as frequency of administration and injected doses were not studied.

Liu et al. used Raman spectroscopy to qualitatively and quantitatively assess the long-term fate of SWNTs functionalized with polyethylene glycol (PEG) of varying

chain length intravenously administered to BALB/c mice [150]. Raman spectroscopic analysis of ex vivo tissues isolated 1 day post-injection of 20  $\mu\text{g}$  SWNTs/mouse showed retention of SWNTs-PEG mainly in liver and spleen. The retained SWNTs-PEG, especially if functionalized with a long PEG chain, were almost cleared from the liver and spleen 3 months after injection with no apparent toxic effects detected in histology specimens and blood chemistry. Administration of higher doses (100  $\mu\text{g}$ /mouse), presumably due to improvement in signal-to-noise-ratio, provided evidence of SWNTs presence in the bladder and feces at 24 hr post-injection suggesting elimination via the renal and biliary routes. On the other hand, the biodistribution and clearance of the injected 100  $\mu\text{g}$  SWNTs over longer period of time, e.g., 1 and 3 months, were not evaluated.

Schipper et al. have reported that on monitoring the blood count of nude mice over a period of 4 months after the intravenous injection of PEG-functionalized SWNTs, no significant differences were detected between the naïve and SWNT-injected mice groups [151]. Histological analysis of tissues from the organs excised 4 months post SWNT injection showed the presence of dark aggregates that were confirmed by Raman spectroscopy to be SWNTs in the liver and spleen macrophages with no obvious pathological features. This observation comes despite the fact that mice were injected with SWNTs two times (on day 0 and 7), the injected dose of SWNTs was 17  $\mu\text{g}$ /mouse. It is quite probably that higher doses of SWNTs as nanocarriers will be required and this could be addressed in future work using a similar model.

Guo et al. studied the biodistribution and excretion of radiolabeled glucosamine functionalized MWNTs following intraperitoneal administration to mice [151]. Tracing

the radioactivity 1 hr post injection revealed the distribution of MWNTs–glucosamine to the main organs and almost complete clearance after 24 hr with less than 70% of the total initial radioactivity excreted in urine and feces. However, free radiolabeled glucosamine released from the functionalized MWNTs in vivo could provide misleading data about the MWNTs biodistribution, thus a more reliable method, e.g., detection of MWNTs Raman signals, could have been applied to further support the presented conclusion.

Meng et al. investigated the organ toxicity and immunological reactions induced following subcutaneous administration of 1 mg of carboxylated MWNTs to BALB/c mice [152]. Histological analysis of heart, liver, kidney and spleen excised from the mice over a period of 2 to 90 days post MWNTs injection revealed normal histology with no apparent accumulation of MWNTs. However, histological examination of axillary lymph nodes excised 30 days post injection showed accumulation of MWNTs that increased and then decreased 60 and 90 days, respectively. Nevertheless, the administered MWNTs were not eliminated, and the study did not investigate the fate of the accumulated MWNTs. Levels of pro-inflammatory cytokines such as TNF- $\alpha$  and IL-17 were detected at a higher level in the sera of the MWNT-injected mice compared to naïve mice 2 days post injection, however, the cytokine levels returned to normal 7 days post injection [152].

### **3.2.6 Significance**

This research encompasses a significant innovation that contribute to the advancement of melanoma therapy and address critical concerns associated with nanosecond pulsed electric field (nsPEF) clinical treatments.

The incorporation of MWCNTs into the nsPEF treatment represents a novel and innovative in vivo approach. MWCNTs possess unique properties, one is that allow them to amplify the electric field near their tips, creating localized high-field zones. By utilizing MWCNTs, the electric field strength required for effective tumor ablation can be reduced, addressing the safety concerns associated with nsPEF clinical treatments.

### **3.3 Materials and Methods**

#### **3.3.1 SEM and TEM**

A scanning electron microscope (SEM, JEOL JSM-7500F, 5.0 kV accelerating voltage and 2 mm working distance) was used to observe the surface morphology of MWCNT. The powder was simply poured on carbon tape. Compressed air spray is used to remove the excess of powder.

Transmission electron microscopy (TEM) measurements were performed with a Tecnai 10 Philips microscope at 80 kV. Prior to the analyses, the MWCNTs were dispersed in ethanol by sonication and a drop of the suspension was deposited on a TEM copper grid with formvar film.

Carbon fiber thicknesses were measured by ImageJ software (developed by Wayne Rasband and provided in the public domain by National Institutes of Health, Bethesda, MD; available at <http://rsb.info.nih.gov/ij/index.html>).

#### **3.3.2 Thermogravimetric Analysis (TGA)**

TGA was performed on a TA Q500 (TA Instruments) from room temperature to 800°C with a heating rate of 5°C/min. The sample size was 33.946 mg, and the analysis

was performed in air, and a balance gas of argon, with flow rates of 60 ml/min and 40 ml/min respectively.

### 3.3.3 Cell culture

The murine melanoma cell lines B16F10 (ATCC® CRL-6475TM) was used in this study. The cells were grown in a humidified incubator at 37°C with 5% CO<sub>2</sub> in the Dulbecco's Modified Eagle Medium (DMEM) produced by ATCC (30-2002), added 10% fetal bovine serum (FBS) (ATCC, 30-2020) and 1% of penicillin-streptomycin (Sigma-Aldrich). After the cells reached a confluency of 80%, they were subcultured in 0.25% Trypsin, 0.1% EDTA enzymes (Corning™, MT25053CI).

### 3.3.4 Pulsed electric field exposure methods

In the in vitro experiments, cell samples were exposed to nsPEF in 1 mm gap electroporation cuvettes (BioSmith, San Diego, CA) at room temperature. Cells were resuspended at  $1 \times 10^6$  cell/ml and 100  $\mu$ l samples of this suspension were loaded in the electroporation cuvettes and subjected to either nsPEF or sham exposure. Trains of trapezoidal 60-ns pulses were delivered to cuvettes from Pulse Forming Line (PFL) pulser. Pulses were applied at 30, 40, and 50 kV/cm with different pulsing number, adjusted to 1Hz. The number of required pulses then calculated as charging effect to compare which can mentioned below [153]:

Equation 1: Charging Effect 
$$\text{Charging effect (V.s/cm)} = E \times \tau \times \sqrt{n}$$

E is the electric field (kV/cm),  $\tau$  is pulse duration (s), and n is the number of pulses.

To treat B16F10 tumors in vivo, mice were anesthetized by inhalation of 3% isoflurane in oxygen (Patterson Veterinary, Devens, MA). Trapezoidal pulses of 200-ns

duration were produced by a custom pulse generation system with an output impedance of 100  $\Omega$ , adjustable pulse amplitude (up to 15 kV), duration (200 to 1000 ns) and frequency (1–100 Hz; Pulse Biosciences, Inc., Hayward, CA). Pulses of 200-ns duration (500 or 1000 pulses, 3 Hz, 50 kV/cm) were applied using an electrode that sandwiched the tumor between two flat round polished stainless-steel plates with a spacing of 6 or 8 mm between the two plates. The electric field was calculated as:  $E = V/d$  where  $V$  is the applied voltage and  $d$  is the distance between the two plate electrodes. Sterile lubricant (KY Lubricating Jelly) was used to ensure an efficient electrical continuity. Animals in the sham control group underwent anesthesia but no nsPEF delivery.

### **3.3.5 Determination of Toxicity of MWCNTs**

Carboxylic acid functionalized multi-walled carbon nanotubes are purchased from the Nanocyl (NC3101, Belgium). The outer diameter and length of the MWCNTs are approximately 9.5 nm and 1.5  $\mu\text{m}$ , respectively, an extent of COOH functionalization less than 4%. A dispersed MWCNTs solution is obtained by sonication and centrifugation, and MWCNTs are dispersed in B16F10 culture media. Using different volumes of MWCNT dispersion in fresh medium, the final concentration of MWCNTs is adjusted to 0, 200, 400, and 600 mg/mL. The cells are resuspended in the above medium containing different concentrations of MWCNTs.

### **3.3.6 Cell viability analysis**

Cell Counting Kit 8 (CCK-8, Dojindo, Kumamoto, Japan) was used to measure cell viability. B16F10 cells were grown to 80% confluency then the cell concentration is adjusted to  $1 \times 10^6$  cells/mL for nsPEF. After pulsing, 15,000 cells were seeded into 96-

well plates (Corning Incorporated, Corning, NY, USA). Cells were cultured for 24 h, then 10  $\mu$ l CCK-8 solution was added to each well, after another 1.5 h, the optical density was measured at an absorbent of 450 nm using a microplate reader (ELx800; BioTek Instruments, Inc., VT, USA). OD value was divided by control value to calculate relative cell survival rate (values were subtracted from background).

### **3.3.7 Apoptosis**

To detect apoptosis, B16/F10 cells ( $5 \times 10^3$  per well of a 384-well plate) were plated, and the Caspase-Glo 3/7 Assay system (Promega, Madison, WI, G8091) was used for analysis in accordance with the manufacturer's instructions 4 and 24 hours post pulsing. The background luminescence associated with the cell culture (with and without MWCNT) and assay reagent (blank reaction) was subtracted from experimental values. As a positive control for apoptosis induction, cells were treated 1–10  $\mu$ m staurosporine. Means of triplicates were used to represent caspase 3/7 activity for the given cells. Each experiment was performed three times with similar results.

### **3.3.8 Conductivity**

Media with and without CNT were analyzed using the network analyzer (E5071C ENA Series, Agilent Technologies). The analyzer measured conductivity  $\sigma'$  ( $S.m^{-1}$ ) at frequencies between 0.1 to 20MHz.

### **3.3.9 Murine tumor model and treatment procedure**

The bred in-house female and male C57BL6/J mice (5–10 weeks of age) were sourced from a separate protocol moved to this protocol, in accordance with the regulations and oversight provided by the Institutional Animal Care and Use Committee

(IACUC). Mice were injected subcutaneously with  $5 \times 10^5$  B16-F10 cells in 50  $\mu$ L Dulbecco's phosphate buffered saline (PBS) in the left flank. The size of primary tumor was assessed by calipers. Mice were weighed before and post-treatment and twice weekly. Tumors were allowed to grow to a diameter of approximately 6-8 mm before treatment. Groups include MWCNT received a total volume of 200  $\mu$ g in 50 ml of PBS with 25G needle through intratumorally injection before pulsing. Tumor growth was measured at 24 h post treatment and twice weekly using a digital caliper, and volumes ( $v$ ) were calculated using the standard formula  $v = ab^2\pi/6$ , where  $a$  is the longest diameter, and  $b$  is the next longest diameter perpendicular to  $a$  [38].

To measure the vaccine effect on survived animals, 7 weeks post treatment were injected in the right dorsolateral flank with  $2.5 \times 10^5$  B16F10 cells in 50  $\mu$ l PBS. An age-matched naïve group of mice was used as control for tumor growth. Animals were monitored for up to 50 days post challenge. Mice were euthanized at the end of the follow-up period or at specified time points described in experimental designs or when they met the criteria described at experimental endpoints in the approved IACUC protocol [38].

### **3.3.10 Statistics analysis**

All experiments were conducted at least three times and data were expressed as Mean  $\pm$  Standard Error of the Mean (S.E.M.). GraphPad Prism version 9 (GraphPad Software, San Diego, California USA) was used to conduct statistical analyses one-way or two-way analysis of variance (one-way or two-way ANOVA), and P-values (were considered significant when  $p \leq 0.05$ ). Also, GraphPad Prism was used to generate

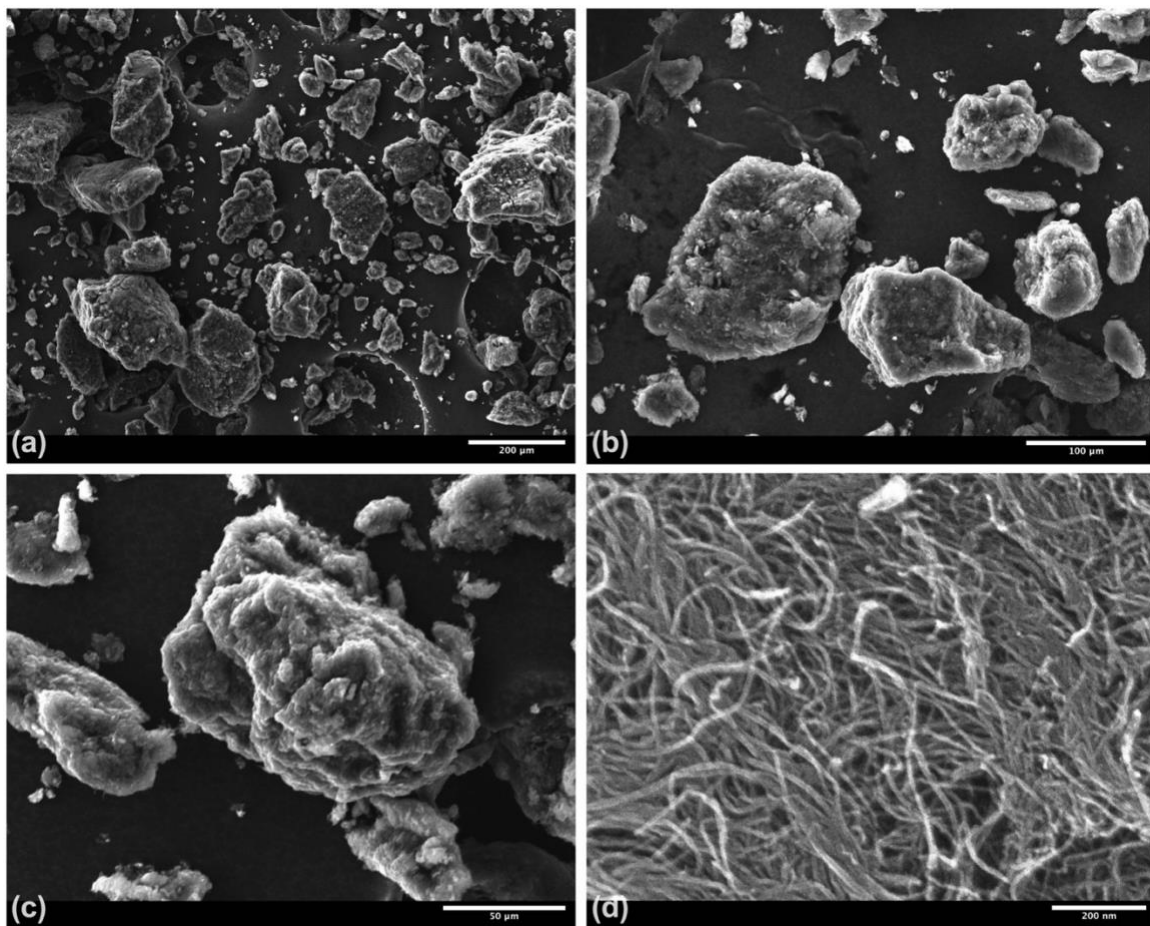
Kaplan–Meier curves and curves were compared using the Log-rank (Mantel Cox) and Gehan-Breslow-Wilcoxon tests for in vivo section.

## **3.4 Results and Discussion**

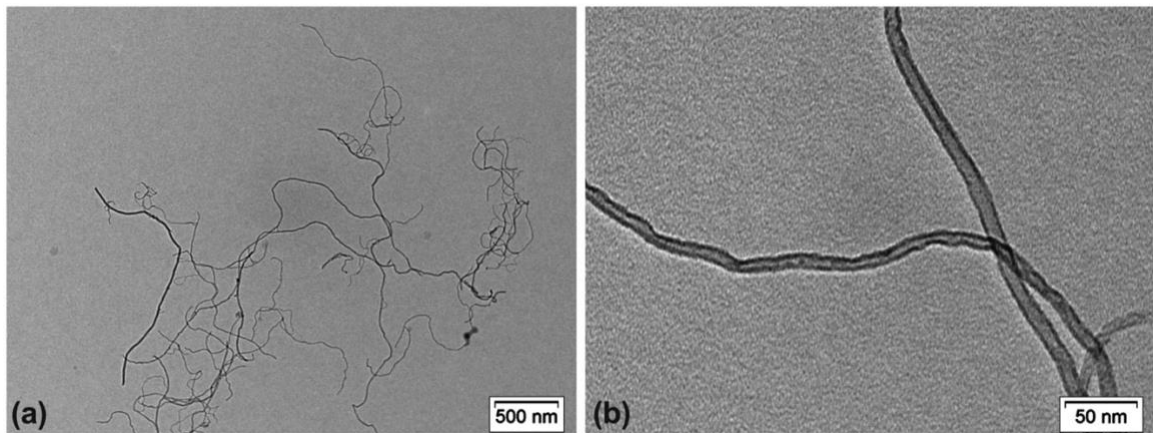
### **3.4.1 Material Characterization**

#### *SEM and TEM showed the MWCNT have a high aspect ratio*

The microstructure and morphology of nanocyl NC3101 was investigated by employing advanced techniques such as Scanning Electron Microscopy (SEM) and Transmission Electron Microscopy (TEM) analysis. TEM analysis unveiled intricate details, showcasing individual nanofibers and offering profound insights into their structural integrity. Notably, these nanofibers displayed a remarkable level of uniformity in their diameter distribution, with an average diameter measuring approximately 9.5 nm and an impressive length of about 1.5  $\mu\text{m}$ , resulting in a notably high aspect ratio. Moreover, TEM examination revealed an absence of defects in the MWCNT, a critical factor in preserving the electrical properties of the CNT.



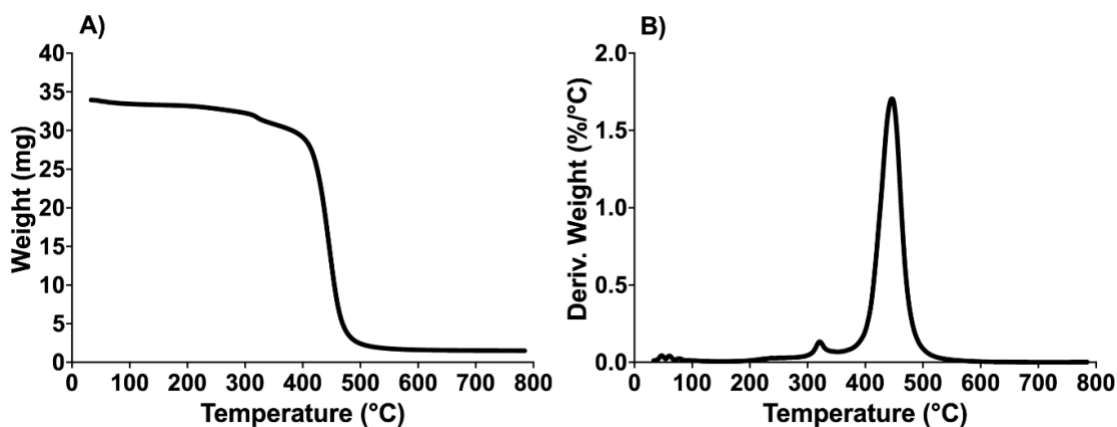
**Figure 15.** SEM images of the surface morphology of MWCNT which poured on carbon tape. (a) 200  $\mu\text{m}$ , (b) 100  $\mu\text{m}$ , and (c) 50  $\mu\text{m}$  showcasing the overall nanotube morphology. (d) High-magnification (200 nm) which providing detailed insights into the nanotube structure. Images provided by Nanocyl.



**Figure 16.** MTEM images of the MWCNT on grid with formvar film. (a) Low magnification (500 nm) providing an overview of the nanotube arrangement and average length (1.5  $\mu\text{m}$ ). (b) High-magnification (50 nm) offering a closer examination of the nanotube's diameter (<10 nm). Images provided by Nanocyl.

***Thermogravimetric Analysis (TGA) showed the MWCNT have a good purity***

TGA was used to analyze the nanotube powder for the percentage of carbon purity, metal oxide, and surface modification (carbocyclic group). According to Figure 17a, difference in residual mass was identified at 650  $^{\circ}\text{C}$ . At this temperature, most carbon-based materials have decomposed, and the residual mass is attributed to the metal catalyst particles that remain. At 650  $^{\circ}\text{C}$ , the residual masses were 4.7%.



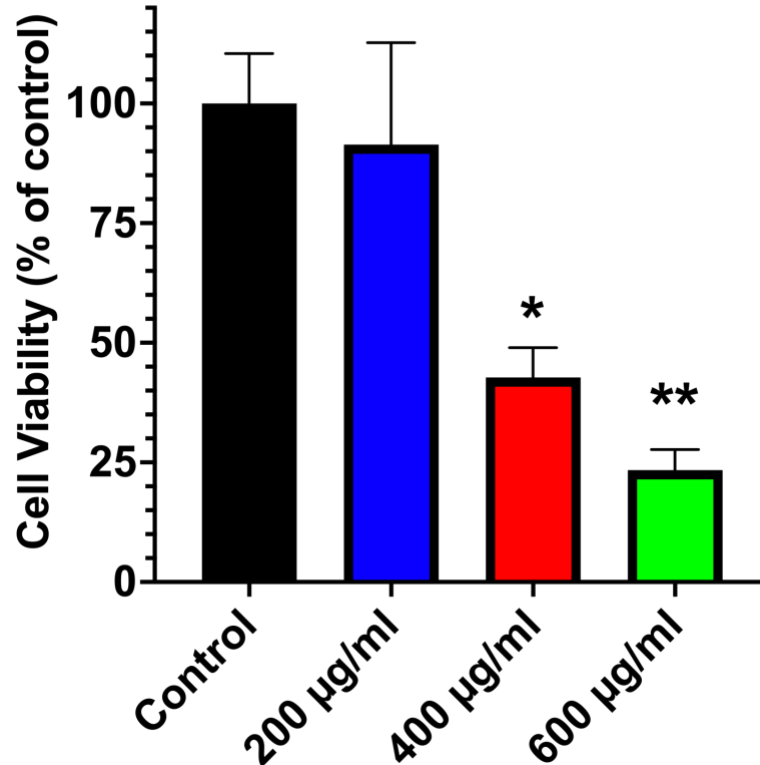
**Figure 17.** Thermogravimetric analysis (TGA) of MWCNT from room temperature to 800 °C with a heating rate of 5 °C/min. (a) Weight percent versus temperature curve which showed the residual masses were 4.7% at 650 °C, and (b) Derivative weight percent versus temperature curve which showed the thermal stability of the MWCNT ( $445.4 \pm 2.7$  °C) and the carboxylated group (first small pick). Data provided by Nanocycl.

Figure 17b shows the derivative weight curve with respect to temperature for the mass-loss curves. The derivative curve determined the oxidation temperature of the MWCNT, as well as defining the mass-loss event as multiple decomposition event, evidenced by the presence of multiple decomposition peaks. The temperature corresponding to the highest peak on this derivative weight curve is identified as the primary oxidation temperature, serving as a key indicator of the thermal stability of the MWCNT, and it was determined to be  $445.4 \pm 2.7$  °C.

### **3.4.2 In Vitro**

#### **3.4.3 *Dose-dependent relationship between the concentration of MWCNT and viability***

A toxicity assessment was done prior to introduce MWCNTs into nsPEF for cancer ablation study. A reasonable concentration of MWCNTs that is minimally toxic is determined by growing B16F10 cells at different MWCNT concentrations. Figure 18 illustrated that at a concentration of 400  $\mu\text{g}/\text{mL}$ , the viability of the cells significantly drops to 42%, with further reductions observed as the concentration of MWCNTs increases. In contrast, the cell viability does not change significantly for MWCNT concentrations less than 200  $\mu\text{g}/\text{mL}$ , suggesting that this concentration range does not impact cell viability. Considering these findings, a concentration of 200  $\mu\text{g}/\text{mL}$  is established for subsequent in vitro nanosecond pulse treatments involving MWCNTs.



**Figure 18.** Effects of different concentrations of MWCNTs on cell viability test (CCK-8 assay) after 24 hours. The final concentration of MWCNTs is adjusted to 0, 200, 400, and 600 µg /mL. Cell viability showed a dose-dependent relationship with the concentration of MWCNT, wherein increasing the MWCNT concentration led to a decrease in cell viability. Notably, at a concentration of 200 µg/mL, no significant impact on cell viability was observed after 24 hours, prompting its selection for subsequent experiments (\*P < .05, \*\*P < .01).

The dose-dependent nature of MWCNT cytotoxicity is revealed through toxicity experiments involving various concentrations. Higher concentrations of MWCNTs result in increased toxicity, demonstrating a correlation between concentration and cytotoxicity. These MWCNTs exhibit a propensity to aggregate within the cell membrane's lipid

bilayer and traverse the membrane owing to the fluidity of lipid bilayers. Furthermore, elevated MWCNT concentrations have the potential to compromise the integrity of the cell membrane, ultimately leading to cell rupture and death [154].

### 3.4.4 Enhancement of nsPEF in combination with MWCNT on Cell Viability

To examine the impact of MWCNTs in combination with nsPEF on B16F10 cells, a concentration of 200  $\mu\text{g/mL}$  was selected as the maximum non-toxic value. Changes in field strength and pulse number were used to study the effects of MWCNTs on nsPEF at this concentration. Figure 19 shows the effect of the above parameters on B16F10 cell viability.

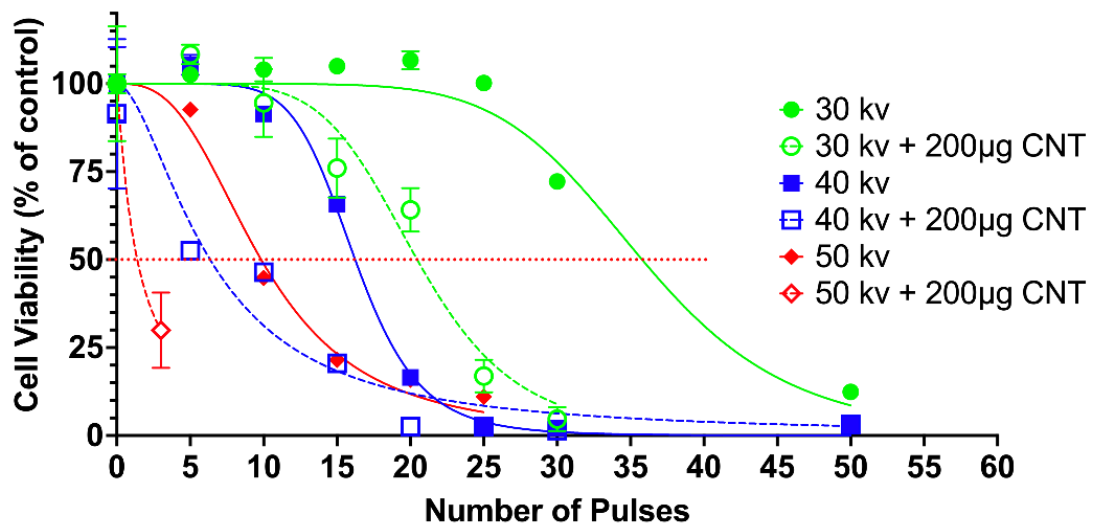


**Figure 19.** Effects of different electric fields in present and absent of MWCNTs (200  $\mu\text{g/ml}$ ) on cell viability test (CCK-8 assay) after 24 hours. B16F10 at a concentration of  $1 \times 10^6$  cell/ml were exposed to nsPEF (60 ns, 1 Hz, at 30, 40, and 50 kV/cm with different pulsing number) in 1 mm gap electroporation cuvettes (100  $\mu\text{l}$ ). The IC-50 for cell viability is reduced significantly when the MWCNTs present in media (\*P < .05, \*\*P < .01).

For measuring the required number of pulses to induce the half-maximal inhibitory concentration (IC-50) we used non-linear regression. Table 1 showed the charging effect for induction of the IC-50 for different electric fields. Compared with the condition without MWCNTs, the addition of MWCNTs significantly reduces the cell viability and needed less charging effect to reach the IC-50. As a result, the nsPEF threshold is reduced by the presence of MWCNT [115, 155].

**Table 1.** Calculated nsPEFs, IC-50 in present (Right) and absent (Left) of MWCNT.

The IC-50 values represent the charging effect of nsPEFs required to inhibit cellular activity by 50% under each respective condition.

| Voltages | - MWCNT          |                 | + MWCNT          |                 |
|----------|------------------|-----------------|------------------|-----------------|
|          | Number of pulses | Charging effect | Number of pulses | Charging effect |
| 30 kV    | 35               | .01             | 20               | .008            |
| 40 kV    | 16               | 0.0096          | 6                | .0058           |
| 50 kV    | 10               | 0.0094          | 2                | .0042           |

### 3.4.5 MWCNT increased the conductivity

A conductivity measurement was carried out in the presence and absence of MWCNT due to the unique electrical properties of CNTs and their good metallicity [156] (Figure 20). The conductivity of the suspension was estimated by the voltage across the suspension and current flowing through the suspension, and the conductivities of the suspension in the presence and absence of MWCNTs were 1.2 and 1.15 S/m, respectively.

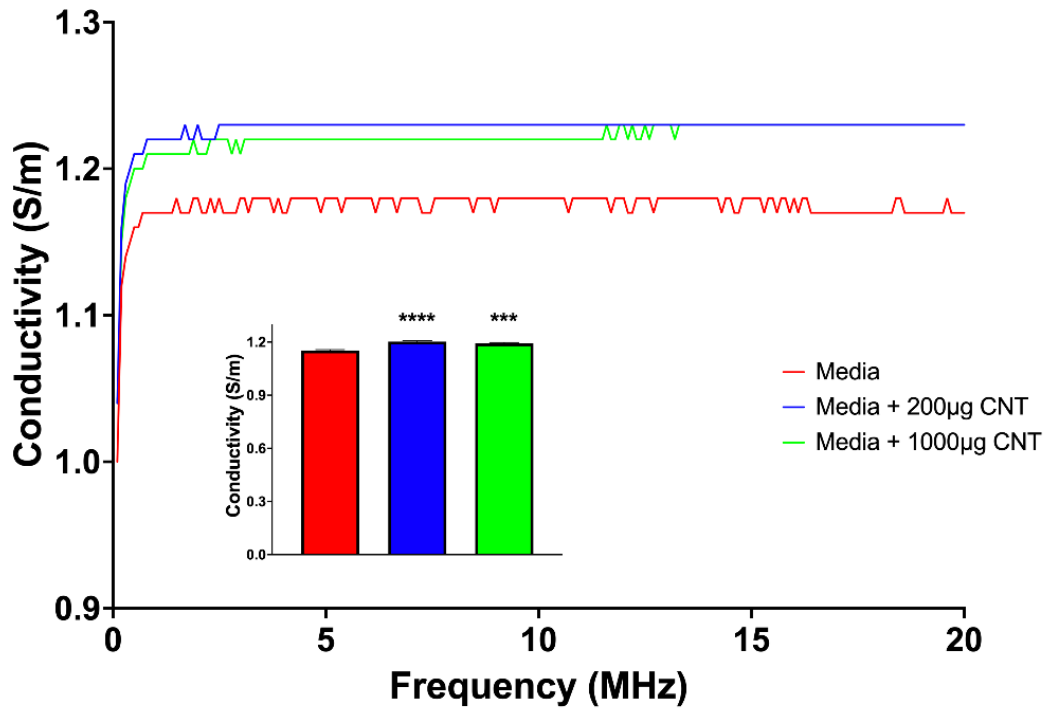


**Figure 20.** Conductivity of cell culture media before and after adding different concentration of MWCNT.

The addition of MWCNTs to the media not only increases its conductivity but also offers additional benefits. Due to the high aspect ratio and excellent electrical conductivity of CNTs, they can enhance the local field strength [42]. When a CNT is inserted into a region of uniform electric field with an amplitude of  $E_0$ , it generates a phenomenon known as the "lightning rod" effect, where an intensified electric field is formed at the tip of the CNT. The amount of electric field enhancement at the CNT tip can be estimated using the following equation CNT [43]:

Equation 2: The electric field strength at the tip of the CNT

$$E_{Tip}/E_0 = \alpha L/D$$

The electric field strength at the tip of the CNT ( $E_{\text{Tip}}$ ) is determined by a constant  $\alpha$ , where  $L$  represents the length and  $D$  denotes the outer diameter of the CNT. Given the high aspect ratio ( $L/D$ ) of our MWCNTs, they possess the ability to effectively concentrate the electric field. This concentrated field strength plays a crucial role in promoting cell death and its associated effects.

Moreover, other studies showed that CNTs in the presence of electric or electromagnetic fields can induce mechanical damage through direct physical contact with the cell membrane [114, 157, 158]. The rotational motion and torque ( $\tau$ ) induced by CNT can enhance the effect of nsPEF by facilitating the penetration of the nanotube through the membrane [114, 158]. A stronger electro-response is obtained when CNTs are combined with low-intensity electric pulses [115]. Due to their substantial specific surface area and strong surface electrostatic interaction, CNTs tend to adsorb randomly around the cell membrane prior to the application of an electric field. Some CNTs may also bind to cell membrane phospholipids [114]. There is no effect of CNTs on cell morphology at this time. However, when the electric field is applied, the CNTs respond by undergoing movement and rotation, aligning with the direction of the electric field. As the CNTs rotate, the force exerted at their tips mechanically deforms and perforates the cell membrane [157, 158].

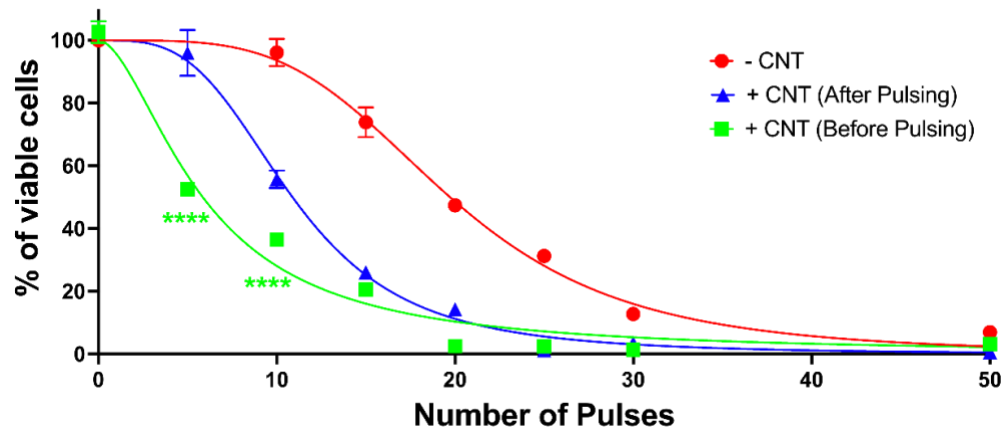


**Figure 21.** MWCNT effect on cell viability (CCK-8 assay) after 24 hours, when added before and after pulsing. The IC-50 for cell viability is reduced significantly when the MWCNTs (200  $\mu\text{g/ml}$ ) present in media during the pulsing in compared to the time adding after pulsing (\*\*\*\*P < .0001).

Considering the significant reduction in the charging effect observed with the presence of CNT in conjunction with nsPEF, our study aimed to delve deeper into the underlying mechanisms responsible for this phenomenon. To this end, we devised an experiment to investigate whether the observed effect was solely attributed to the enhancement of electrical properties by the CNT or if other factors were at play. In this experimental setup, we subjected B16F10 cells to nsPEF and introduced CNT both before and immediately after pulsing (as illustrated in Figure 21). Notably, our results revealed persistent significant differences between these two conditions, thereby underscoring the electrical enhancement imparted by CNT in the context of low-intensity electric pulses. Furthermore, we observed discrepancies between the group without CNT and the group where CNT was introduced post-pulsing. This intriguing finding suggests

the involvement of multiple mechanisms, with post-pulsing cells appearing more susceptible to the enhancing effects of CNT, potentially influencing cell death outcomes.

### 3.4.6 Lack of Apoptotic Induction on B16F10 Cells by MWCNT, nsPEFs, or Their Combination

Several cell lines have been shown to undergo apoptosis in response to CNT [159] or nsPEF [10], or their combinations [160]. To determine whether B16F10 cells undergo apoptosis, we decided to investigate the process further. B16F10 cells were exposed to increasing numbers of pulses (60 ns, 40 kV/cm, 1 Hz) and caspase 3/7 activity were measured at 4 and 24 h post treatment in presence and absence of MWCNT (Figure 22). Staurosporine was used as a positive control (Figure 22.b). Results showed that in B16F10 nsPEF or MWCNT or their combination did not induce caspase activation although the pulse treatment severely impaired cell viability (Figure 19) [39].

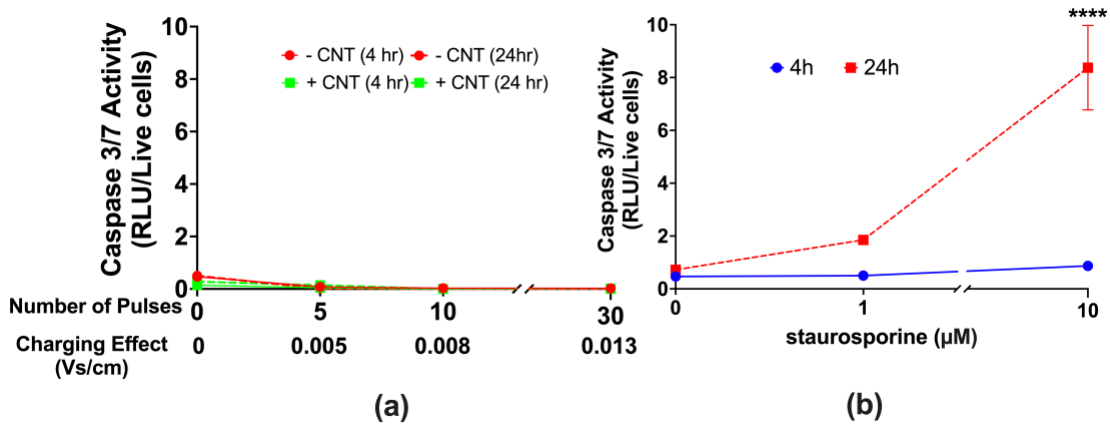


**Figure 22.** nsPEF not triggers apoptotic cell death in B16F10 cells in present or absence of MWCNT. (A) B16F10 cells were either exposed in cuvettes ( $\pm$  MWCNT) to increasing

numbers of 60-ns pulses (4 kV/cm, 1 Hz) or (B) treated with staurosporine. Caspase 3/7 activation (Caspase-Glo 3/7 assay) were measured at 4 and 24 hours post treatment.

### 3.4.7 In Vivo

### 3.4.8 MWCNTs Demonstrate No Impact on Tumor Growth Rate

To study the effect of CNT on enhancement of nsPEF to ablate the melanoma, the C57BL/6 syngeneic B16F10 melanoma cell line was used. This model has been extensively used to study nsPEF ablation [161] but the protective antitumor response triggered by the pulse treatment has not yet been reached. In preliminary experiments we investigated the effect of MWCNT on the tumor growth rate (Figure 23.b).

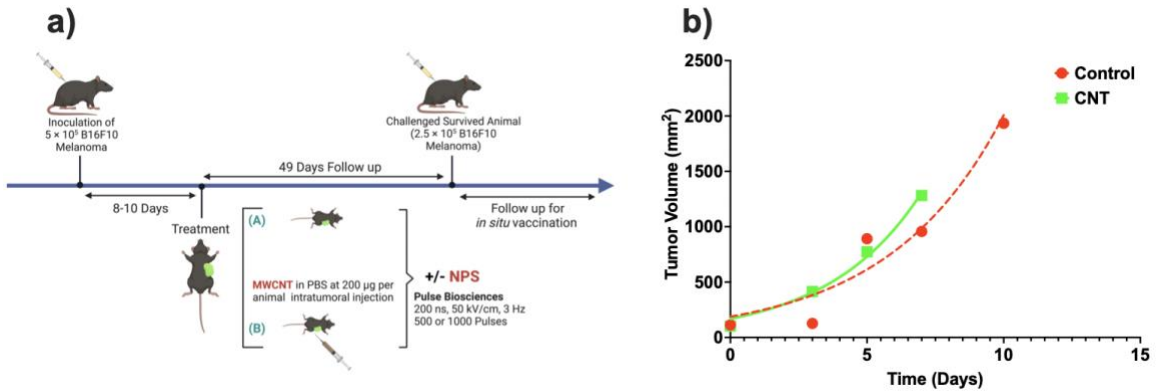


**Figure 23.** A) Schematic of in vivo experiment. Primary tumors were initiated in C57BL/6/J mice via inoculation of the left flank with  $5 \times 10^5$  B16-F10 cells approximately 8-10 days before the day of treatment (day 0). The day before treatment, the tumors were measured, and mice were divided into treatment groups such that the average tumor volumes were evenly distributed (Created with BioRender.com). B) B16-F10 model primary tumor growth curves. The treatment group included an intertumoral injection of MWCNT in compared to control (n=3).

Intratumorally injection of MWCNT at a safe concentration of 200  $\mu\text{g}$  per animal was performed, as determined by in vitro data [152]. Notably, MWCNT did not exert any influence on the rate of tumor growth, which remained consistent with the control group. Animals were euthanized prior to day 10 in accordance with the tumor size limitation outlined in the approved IACUC protocol. The next step is to comprehensively evaluate the potential of MWCNTs combined with nsPEF in the elimination of melanoma cancer.

#### **3.4.9 Efficient Pulsing with MWCNT: Achieving a 50% Reduction in Pulsing Requirements for Tumor Elimination**

The purpose of this section was to evaluate the effects of nsPEF alone and in combination with MWCNT. In previous studies, pulses of 50 kV/cm, 3 Hz, 300 ns with 1000 pulses effectively eliminated cancer cells in melanoma and breast cancer models [18]. Therefore, we employed the same pulsing condition as a positive control for nsPEF to ablate B16F10 cancer cells in the C57BL6/J mouse model. A half-pulse number, 500 pulses, was used to assess the effectiveness of MWCNT groups in tumor ablation. The treatment efficacy of nsPEF was evaluated based on C57BL6/J mice survival in the B16-F10 model.

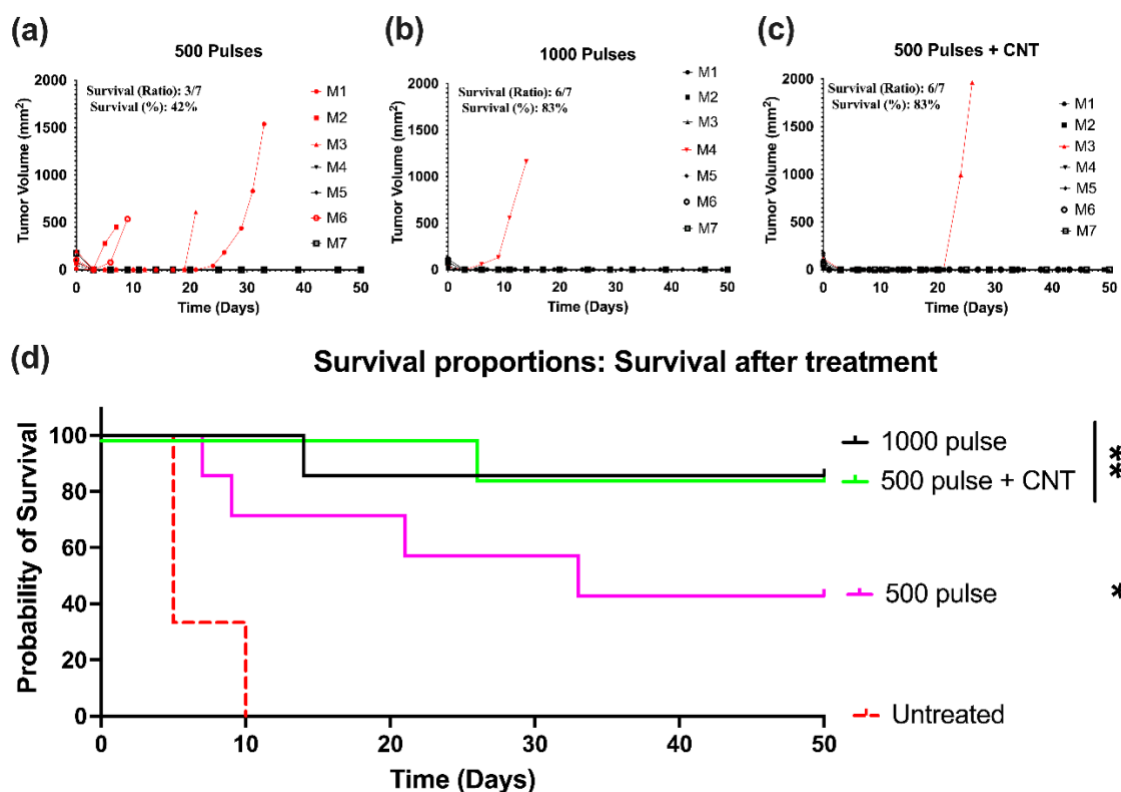


**Figure 24.** B16-F10 model primary tumor growth curves for nsPEF groups. The treatment groups included a (a) 500 pulses, (b) 1000 pulses, and (c) 500 Pulses with MWCNT (received a total volume of 200  $\mu\text{g}$  in 50 ml of PBS with 25G needle before pulsing) ( $n=7$ ). Tumors that regressed are displayed in the black monochromatic scheme, while those that progressed after treatment are shown in red. (d) B16-F10 model Kaplan-Meier survival curves. The log-rank (Mantel-Cox) and Gehan-Breslow-Wilcoxon tests were performed using GraphPad Software. The family-wise significance level of 5%, using the Bonferroni-corrected threshold method for p-values, indicated significance between groups (\*),  $p < 0.05$ .

Figure 24 shows that 1000 pulses successfully ablated the tumor, resulting in 6 out of 7 mice's survival. However, when the pulse number was reduced to 500, only 3 out

of 7 mice survived due to the insufficient electric field required for ablation. The survival rate when 500 pulses were combined with MWCNT was similar to that of 1000 pulses (6 out of 7). As discussed in the in vitro section, MWCNT possess properties that enhance the nsPEF. Consequently, the combination of nsPEF with MWCNT can facilitate tumor ablation with safe electric fields and improved electric field distributions [157].

#### **3.4.10 Lacking ISV after challenge**

To assess the immune response among the experimental groups, C57BL6/J mice that had successfully cleared the primary tumor were subjected to a challenge.

Approximately 7 weeks after treatment, the mice were subcutaneously inoculated with  $2.5 \times 10^5$  B16-F10 cells (half of the primary tumor) on the opposite (right) flank.

Concurrently, a group of age-matched C57BL6/J mice served as untreated controls to ensure cellular viability and for comparison purposes. Tumor growth curves were plotted from the day of the challenge (Figure 25).

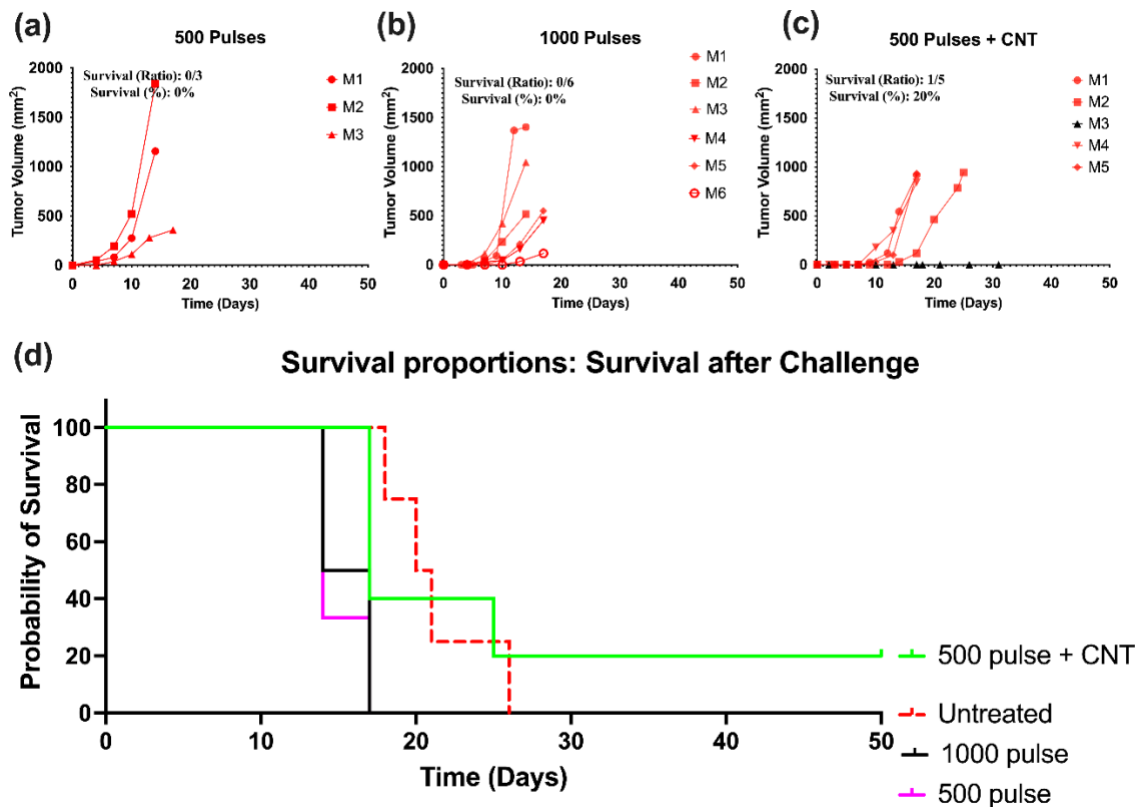


**Figure 25.** B16-F10 model challenged tumor growth curves for nsPEF groups. After clearing the primary tumor, C57BL6/J mice were challenged by subcutaneously inoculating them with  $2.5 \times 10^5$  B16-F10 cells on the opposite flank approximately 7 weeks after treatment. The treatment groups included survived animals from the primary tumor (a) 500 pulses, (b) 1000 pulses, and (c) 500 Pulses with MWCNT. Tumors that regressed are displayed in the black monochromatic scheme, while those that progressed after challenge are shown in red. (d) B16-F10 model Kaplan-Meier survival curves after challenge. The log-rank (Mantel-Cox) and Gehan-Breslow-Wilcoxon tests were performed using GraphPad Software.

As shown, all untreated mice developed tumors within 3 weeks. Similarly, the groups treated with 1000 pulses, 500 pulses, and 500 pulses with MWCNT exhibited

comparable tumor development rates to the untreated controls. Tumor rejection was observed in 0% (0/6), 0% (0/3), and 20% (1/5) of the challenged mice, respectively among these groups. Consequently, no vaccine effect was observed in these experimental treatment groups.

### **3.5 Conclusion**

In conclusion, our study focused on the combination of nsPEF with MWCNT to enhance tumor ablation. Through our research, we discovered that the utilization of nsPEF, and MWCNT in combination yielded promising results. This combination approach demonstrated improved tumor ablation efficacy by reducing the required charging effect C57BL6/J mice model. These findings suggest that the integration of nsPEF, and MWCNT holds significant potential in advancing cancer therapy and promoting tumor clearance. Further investigations and clinical studies are warranted to validate and expand upon these encouraging results, ultimately paving the way for more effective and targeted cancer treatment strategies.

## CHAPTER 4:

### Discussions

#### 4.1 In vitro studies of cell responses to nanosecond pulsed electric fields

The first chapter shows that nanosecond pulses generated by commonly used pulse generators (PFL and BL) with the same pulse duration and essentially the same electric field and frequency distributions can result in different cell responses owing to distinct post-pulse waveforms determined by their dissimilar circuit topology. These subtle post-pulse waveform differences, which have been overlooked, can have a significant impact on functional outcomes. Specifically, the PFL post-pulse waveform was unipolar, while the BL pulse was bipolar. For instance, at 4 kV, the PFL pulse exhibited a small post-pulse waveform (5% of the main pulse, same polarity) lasting approximately 2  $\mu$ s. Conversely, the BL pulse had an even smaller post-pulse waveform (1-2% of the main pulse, opposite polarity) but lasted longer ( $\sim$ 50  $\mu$ s). These post-pulses were a result of their electrical configurations being unique. In the PFL configuration, the load (cells in cuvette) was isolated from the charging circuit by a switch. After the switch closed, allowing the 100 ns pulse current flow, there was a brief charging current from the high voltage power supply. However, this current stopped quickly as the switch recovered and isolated the load from the charging circuit. The recovery process occurred on a scale of 2  $\mu$ s, much shorter than that of a conventional spark gap switch [49]. This could be attributed to the small energy involved (100 mJ) and the short pulse duration

(100 ns), whereas a conventional spark gap switch can handle >10 J and conduct for >1 ms. In our case, the discharge mode might involve a streamer-arc channel without significant heating of the ambient air, allowing for a rapid switch recovery. On the other hand, in the BL configuration, the load was continuously connected to the BL and remained in the charging loop regardless of the switch state. A small charging current was present throughout the charging time until the BL was fully charged before the next pulse (Figure 1a).

The time distinction in cell responses to PFL pulses and BL pulses, as summarized in Figure 14, can be attributed to the differences in their post-pulse condition. During the main pulse interval, the frequency contents, charges, and energy of both types of pulses were almost identical, with some cases where the BL pulses exceeded the PFL pulses. In overall, cells exhibited greater sensitivity to the PFL than the BL pulser with lower pulse numbers or electric field intensities for inducing cell membrane permeability, dissipation of  $\Delta\Psi_m$ , a decrease in mitochondrial SRC, a biphasic effect on tPMET, and eventual cell death. These differences in the cell responses to these waveforms have potentially unique application for inducing non-lethal effects that can specifically affect cell physiological fate as well as pathological outcomes. Also, the biphasic behavior holds significant implications for enhancing the efficacy of ablation procedures and potentially facilitating cellular differentiation in cancer therapy, ultimately leading to the prospect of in-situ vaccination. Interestingly, both pulse types demonstrate a similar dependence on pulse number in terms of ROS production. Despite the post-pulse having a magnitude of less than 5% of the main pulse and lasting for a longer duration (50  $\mu$ s), its low intensity is still expected to decrease the membrane

potential caused by the main pulse. To the best of our knowledge, this is the first time that charging current, which is reflected as a post-pulse, has been reported to have such a significant effect on cellular response. This work highlights the importance of considering the charging characteristics in pulse generator design and when comparing cell responses under similar pulse conditions.

#### **4.2 In vivo studies with nanosecond pulsed electric fields**

Second chapter shows that the combination of nanosecond pulses with CNT can enhance the nsPEF and improved tumor ablation efficacy by reducing the required pulsing condition on C57BL6/J mice model by at least two times as shown by reducing the charging requirement for ablation from 5.0 to 2.5 Vs/cm to. These results hold the promise that by reducing the pulsing conditions, it can facilitate the use of PFL in in vivo studies, despite its half-charging voltage output. The combination with carbon nanotubes addresses and resolves this limitation effectively.

To examine the impact of MWCNTs in combination with nsPEF on B16F10 cells, a concentration of 200  $\mu\text{g/mL}$  was selected as the maximum non-toxic value for in vitro. The dose-dependent nature of MWCNT cytotoxicity is revealed through toxicity experiments involving various concentrations (Figure 18). The CNT utilized in this study are carboxylated (Figure 17), which exhibits superior biocompatibility compared to pristine CNTs. Kagan et al. showed that when human monocyte-derived macrophages were incubated with carboxylated CNTs, these nanotubes formed fewer intracellular aggregates and had lower effects on cell viability compared to pristine SWNTs [140]. Also, treatment of murine RAW 264.7 macrophages with pristine CNTs resulted in significant depletion of glutathione, an oxidative stress biomarker, in contrast to

carboxylated CNTs treatment [141]. It is important to note that variations in CNT functionalization density, used doses, and incubation time can yield different results. However, it is evident that an increase in the purity and functionalization of CNTs may enhance their cytocompatibility. It is crucial to consider that despite functionalized CNTs showing improved cytocompatibility, they can still induce dose-dependent cytotoxic effects [147]. Nevertheless, in both *in vitro* and *in vivo* studies, the use of 200  $\mu\text{g}$  carboxylated multi-walled carbon nanotubes (MWCNT) did not exhibit a significant effect on cell viability (*in vitro*) and did not impede tumor growth compared to the control group (*in vivo*). Meng et al. investigated the organ toxicity and immunological reactions induced following subcutaneous administration of 1 mg of carboxylated MWNTs to BALB/c mice [152]. Histological analysis of heart, liver, kidney and spleen excised from the mice over a period of 2 to 90 days post MWNTs injection revealed normal histology with no apparent accumulation of MWNTs.

The combination of nsPEFs with MWCNT resulted in an enhancement of cell death. Figure 20 shows the addition of MWCNTs significantly reduces the cell viability and required lower charging conditions to reach the IC-50. As a result, the nsPEF threshold is reduced by the presence of MWCNT at least twofold [115, 155]. Similarly, Figure 24 illustrated the consistent trend in the *in vivo* model. The 1000 pulses (10 Vs/cm) successfully ablated the tumor, resulting in 6 out of 7 (86%) mouse survival mice. However, when the pulse number was reduced to 500 pulses (5 Vs/cm), only 3 out of 7 (43%) mice survived due to the insufficient charging required for ablation. only 3 out of 7 (43%) mice survived due to the insufficient charging required for ablation. The survival rate when 500 pulses were combined with MWCNT was the same as that of 1000 pulses

(6 out of 7, 86%), which showed the combination of nsPEFs with MWCNT resulted in an enhancement of tumor ablation due to the CNT properties. One contributing factor is the unique electrical properties of MWCNT, characterized by their favorable metallicity, as evidenced by conductivity measurements [156] (Figure 20). The conductivities of the suspension in the presence and absence of MWCNTs were 1.2 and 1.15 S/m, respectively.

The addition of MWCNTs to the media not only increases its conductivity but also offers additional benefits. Due to the high aspect ratio which showed on TEM (Figure 26) and excellent electrical conductivity of CNTs, they can enhance the local field strength [42]. When a CNT is inserted into a region of uniform electric field, it generates a phenomenon known as the "lightning rod" effect, where an intensified electric field is formed at the tip of the CNT. The amount of electric field enhancement at the CNT tip is proportional to its aspect ratio ( $L/D$ ) [43]. This concentrated field strength is hypothesized to have a crucial role in promoting cell death.

Additionally, the ability of CNTs to penetrate the cell membrane, resembling nano-needles, could be explained by a theoretical nanosyringe mechanism simulated by Lopez et al. for nanotube insertion into the lipid bilayer [44]. Molecular dynamics studies by Lopez and colleagues demonstrated that a hydrophobic nanotube with hydrophilic tips initially adsorbs horizontally onto a model membrane. Subsequently, the nanotube spontaneously changes its orientation from horizontal to vertical alignment, forming a transmembrane pore-like orientation through the bilayer. This hypothesis suggests that it may also enhance the poration of the cell membrane followed by nsPEF. Moreover, other studies showed that CNTs in the presence of electric or electromagnetic fields can induce

mechanical damage through direct physical contact with the cell membrane [114, 157, 158]. The rotational motion and torque ( $\tau$ ) induced by CNT can enhance the effect of nsPEF by facilitating the penetration of the nanotube through the membrane [114, 158]. A stronger electro-response is obtained when CNTs are combined with low-intensity electric pulses [115]. Due to their substantial specific surface area and strong surface electrostatic interaction, CNTs tend to adsorb randomly around the cell membrane prior to the application of an electric field. Some CNTs may also bind to cell membrane phospholipids [114]. There is no effect of CNTs on cell morphology at this time. However, when the electric field is applied, the CNTs respond by undergoing movement and rotation, aligning with the direction of the electric field. As the CNTs rotate, the force exerted at their tips mechanically deforms and perforates cell membranes [157, 158].

Despite the enhancement in tumor ablation achieved through this combination, it did not manifest an increase in vaccine effect or in situ vaccination following treatment. Figure 25 showed that all tumor-free mice developed tumors within 3 weeks, when the rodents were re-injected with tumor cells. Similarly, the groups treated with 1000 pulses, 500 pulses, and 500 pulses with MWCNT exhibited comparable tumor development rates to the untreated controls. Tumor rejection was observed in 0% (0/6), 0% (0/3), and 20% (1/5) of the challenged mice, respectively among these groups. Consequently, no vaccine effect was observed in these experimental treatment groups in the ectopic mouse melanoma model, consistent with findings by Rossi et al [39], where only a few animals exhibited tumor rejection as a vaccine effect. A notable challenge identified in these cases was the persistent presence of immunosuppression in the TME [38], as highlighted by Guo et al [36].

It seems that there are two distinct thresholds or types of targets that need activation to achieve tumor-free animals on one hand and tumor-free animals with an in situ vaccination effect on the other. The hypothesis suggests that the vaccine effect is attributed to an "optimal" form of nsPEF-induced regulated cell death (RCD), specifically one that is considered immunogenic. This type of RCD allows dendritic cells (DCs) to effectively detect cancer antigens and present them to T-cells through cross-presentation, as reviewed by Galluzzi et al [40]. nsPEFs were demonstrated to induce intrinsic apoptosis in Jurkat cells, as evidenced by caspase-3/9 activation, along with cytochrome c release into the cytoplasm, as reported by Beebe et al [162]. Ren et al. reported in APAF1 knockdown Jurkat cells that nsPEFs induced caspase-dependent apoptosis at lower electric fields, while at higher electric fields, it led to caspase-independent regulated cell death (RCD) [163]. Figure 22 shows that in B16F10 nsPEF or MWCNT or their combination did not induce caspase activation although the pulse treatment severely impaired cell viability (Figure 19), which agrees with Pescatori et al. They reported that incubating carboxylated or amine-functionalized MWNTs with Jurkat T cell line or THP-1 monocytic cell line did not induce cell apoptosis [146]. Interestingly, nsPEFs do not induce apoptosis in two cell types known for inducing tumor elimination with vaccine effects and in situ vaccinations [2]. The cell death mechanism(s) in these to models of in situ vaccination are not yet known, although 4T1-luc cells were shown to be immunogenic in response to nsPEFs [34].

Given that the PFL induces distinct cellular responses I first chapter, exploring its potential for in vivo studies becomes a valuable avenue for further investigation. In our in vivo studies, nanosecond pulses include around 100 ns durations, 1000 pulses at 50

kV/cm (5 Vs/cm), can be safely eliminated a melanoma tumor. These conditions render the PFL less practical due to its half-charging voltage output, thereby raising safety concerns. Consequently, to overcome this limitation, we used our standard BL pulser, and integrated it with CNTs. This combination enhances the nsPEF and offers potential benefits for future studies by enabling the use of lower nsPEF conditions while harnessing the advantages of the PFL pulser.

## CHAPTER 5:

### Conclusions

The main objective of this thesis is to explore the effects of nsPEFs on cells and tumor tissues. The strategies employed include in vitro exposure of B16f10 melanoma cells to two different pulse generators that exhibit different post-pulse waveforms that differentially affected cell responses such that the PFL generator waveform induced cell responses at lower thresholds for most importantly reducing cell viability, dissipating the  $\Delta\Psi_m$ , and diminishing the mitochondrial spare respiratory capacity than the BL generator waveform. The differences in the cell responses to these different waveforms have potentially unique application for inducing non-lethal effects, that can specifically affect cell physiological fate. This can be seen for enhanced electron transport in response to the PFL that is absent with the BL.

These studies also show that a PFL generator could possibly produce more effective tumor elimination that could more readily lead to effective immune responses and in situ vaccination to B16f10 melanoma tumors, which is absent in the present in vivo BL pulse generators in this melanoma model. This may also translate to other cancer models where immunity and in situ vaccination are absent such as in the mouse Pan02 pancreatic model. Nevertheless, to enhance tumor elimination, it demonstrated my hypothesis that CNT reduced the charging effect to eliminate 85-90% of B16f10 tumors by at least two-fold by one or more mechanisms. While in vitro results do not always translate to in vivo tumor models, it is noteworthy that CNT decreased the charging requirement for cell death and tumor elimination by

two-fold in vitro and in vivo. This two-fold decrease in charging requirement may be helpful with a PFL generator in vivo requiring twice the voltage.

Overall, the results gained from in vitro and in vivo nsPEF treatment of B16f10 melanoma cells and tumors provided new insight in 1) possibilities for nsPEF waveforms to induce selective physiological cell responses related to electron transport, metabolism, differentiation, proliferation, and other redox cell processes, 2) possibilities to reduce the charging requirement for tumor elimination with the addition of CNT to nsPEF treatment of tumors and 3) the possible application of a more effect pulse generator with PFL configuration for tumor elimination and possibly immunity.

## REFERENCES

- [1] Wootton, D., *The invention of science: A new history of the scientific revolution*. 2015: Penguin UK.
- [2] Beebe, S.J., *Nanosecond Pulsed Electric Fields (nsPEFs) Enhance Pulsed Power Applications for Biology and Medicine Nanosecond Pulsed Electric Fields-Enhances Pulsed Power*. J Tumor Med Prev, 2023.
- [3] Schoenbach, K.H., S.J. Beebe, and E.S. Buescher, *Intracellular effect of ultrashort electrical pulses*. Bioelectromagnetics: Journal of the Bioelectromagnetics Society, The Society for Physical Regulation in Biology and Medicine, The European Bioelectromagnetics Association, 2001. **22**(6): p. 440-448.
- [4] Gowrishankar, T.R., et al., *Microdosimetry for conventional and supra-electroporation in cells with organelles*. Biochemical and biophysical research communications, 2006. **341**(4): p. 1266-1276.
- [5] Beebe, S.J., et al., *Ultrashort electric pulse effects in biology and medicine*. 2021: Springer.
- [6] Joshi, R.P., A.L. Garner, and R. Sundararajan, *Review of Developments in Bioelectrics as an Application of Pulsed Power Technology*. IEEE Transactions on Plasma Science, 2023: p. 1-36.
- [7] Batista Napotnik, T., T. Polajžer, and D. Miklavčič, *Cell death due to electroporation – A review*. Bioelectrochemistry, 2021. **141**: p. 107871.
- [8] Pakhomov, A.G., et al., *Long-lasting plasma membrane permeabilization in mammalian cells by nanosecond pulsed electric field (nsPEF)*. Bioelectromagnetics: Journal of the Bioelectromagnetics Society, The Society for Physical Regulation in Biology and Medicine, The European Bioelectromagnetics Association, 2007. **28**(8): p. 655-663.
- [9] Beebe, S.J., et al., *Transient features in nanosecond pulsed electric fields differentially modulate mitochondria and viability*. PLoS One, 2012. **7**(12): p. e51349.
- [10] Ford, W.E., et al., *Nanosecond pulsed electric fields stimulate apoptosis without release of pro-apoptotic factors from mitochondria in B16f10 melanoma*. Archives of biochemistry and biophysics, 2010. **497**(1-2): p. 82-89.
- [11] Stacey, M., et al., *Differential effects in cells exposed to ultra-short, high intensity electric fields: cell survival, DNA damage, and cell cycle analysis*. Mutation Research/Genetic Toxicology and Environmental Mutagenesis, 2003. **542**(1-2): p. 65-75.
- [12] Beebe, S.J. and K.H. Schoenbach, *Nanosecond pulsed electric fields: a new stimulus to activate intracellular signaling*. 2005, Hindawi. p. 297-300.
- [13] Casciati, A., et al., *Effects of Ultra-Short Pulsed Electric Field Exposure on Glioblastoma Cells*. Int J Mol Sci, 2022. **23**(6).
- [14] Beebe, S.J., et al., *Nanosecond pulsed electric field (nsPEF) effects on cells and tissues: apoptosis induction and tumor growth inhibition*. IEEE Transactions on plasma science, 2002. **30**(1): p. 286-292.
- [15] McDaniel, A., et al., *Nano-pulse stimulation™ therapy (NPS™) is superior to cryoablation in clearing murine melanoma tumors*. Front Oncol, 2022. **12**: p. 948472.

- [16] Xie, F., et al., *Ablation of myocardial tissue with nanosecond pulsed electric fields*. PLoS One, 2015. **10**(12): p. e0144833.
- [17] Zemlin, C., F. Xie, and S. Xiao, *Optimal Parameters for the Ablation of Myocardial Tissue With Pulsed Electric Fields*. 2013, Am Heart Assoc.
- [18] Chen, R., et al., *A protective effect after clearance of orthotopic rat hepatocellular carcinoma by nanosecond pulsed electric fields*. European Journal of Cancer, 2014. **50**(15): p. 2705-2713.
- [19] Nuccitelli, R., et al., *Non-thermal nanoelectroablation of UV-induced murine melanomas stimulates an immune response*. Pigment cell & melanoma research, 2012. **25**(5): p. 618-629.
- [20] Guo S, J.Y., Burcus NI, Lassiter BP, Tanaz R, Heller R, Beebe SJ, *Nano-pulse stimulation induces potent immune responses, eradicating local breast cancer while reducing distant metastases*. Int J Cancer., 2018. **142**: p. 629-640.
- [21] Guo, S., et al., *Nano-Pulse Stimulation for the Treatment of Pancreatic Cancer and the Changes in Immune Profile*. Cancers (Basel), 2018. **10**(7).
- [22] Kotnik, T., et al., *Role of pulse shape in cell membrane electropermeabilization*. Biochimica et Biophysica Acta (BBA)-Biomembranes, 2003. **1614**(2): p. 193-200.
- [23] Semenov, I., et al., *Recruitment of the intracellular Ca<sup>2+</sup> by ultrashort electric stimuli: the impact of pulse duration*. Cell Calcium, 2013. **54**(3): p. 145-150.
- [24] Teissie, J. and M.-P. Rols, *An experimental evaluation of the critical potential difference inducing cell membrane electropermeabilization*. Biophysical journal, 1993. **65**(1): p. 409-413.
- [25] Tekle, E., R.D. Astumian, and P.B. Chock, *Electroporation by using bipolar oscillating electric field: an improved method for DNA transfection of NIH 3T3 cells*. Proceedings of the National Academy of Sciences, 1991. **88**(10): p. 4230-4234.
- [26] Novickij, V., et al., *Does the shape of the electric pulse matter in electroporation?* Front Oncol, 2022. **12**: p. 958128.
- [27] Beebe, S.J., N.M. Sain, and W. Ren, *Induction of cell death mechanisms and apoptosis by nanosecond pulsed electric fields (nsPEFs)*. Cells, 2013. **2**(1): p. 136-162.
- [28] Ibey, B.L., et al., *Bipolar nanosecond electric pulses are less efficient at electropermeabilization and killing cells than monopolar pulses*. Biochemical and biophysical research communications, 2014. **443**(2): p. 568-573.
- [29] Pakhomov, A.G., et al., *Cancellation of cellular responses to nanoelectroporation by reversing the stimulus polarity*. Cellular and molecular life sciences, 2014. **71**: p. 4431-4441.
- [30] Kolb, J.F., S. Kono, and K.H. Schoenbach, *Nanosecond pulsed electric field generators for the study of subcellular effects*. Bioelectromagnetics, 2006. **27**(3): p. 172-87.
- [31] Asadipour, K., et al., *Nanosecond Pulsed Electric Fields (nsPEFs) Modulate Electron Transport in the Plasma Membrane and the Mitochondria*. Bioelectrochemistry, 2024. **155**: p. 108568.
- [32] D'Autréaux, B. and M.B. Toledano, *ROS as signalling molecules: mechanisms that generate specificity in ROS homeostasis*. Nature reviews Molecular cell biology, 2007. **8**(10): p. 813-824.
- [33] Lassiter, B.P., S. Guo, and S.J. Beebe, *Nano-pulse stimulation ablates orthotopic rat hepatocellular carcinoma and induces innate and adaptive memory immune mechanisms that prevent recurrence*. Cancers, 2018. **10**(3): p. 69.
- [34] Guo, S., et al., *Nano-pulse stimulation induces potent immune responses, eradicating local breast cancer while reducing distant metastases*. International journal of cancer, 2018. **142**(3): p. 629-640.

- [35] Beebe, S.J., B.P. Lassiter, and S. Guo, *Nanopulse stimulation (NPS) induces tumor ablation and immunity in orthotopic 4T1 mouse breast cancer: A review*. *Cancers*, 2018. **10**(4): p. 97.
- [36] Guo, S., et al., *Nano-pulse stimulation for the treatment of pancreatic cancer and the changes in immune profile*. *Cancers*, 2018. **10**(7): p. 217.
- [37] Nanajian, A., *The Impact of Nanopulse Treatment on the Tumor Microenvironment in Breast Cancer: Overturning the Treg Immunosuppressive Dominance*. 2021, Old Dominion University.
- [38] Ruedlinger, B.L., *The Investigations of NPS Modulated Immunity and Immunometabolism*. 2021, Old Dominion University.
- [39] Rossi, A., et al., *Mechanisms and immunogenicity of nsPEF-induced cell death in B16F10 melanoma tumors*. *Scientific Reports*, 2019. **9**(1): p. 431.
- [40] Galluzzi, L., et al., *Immunogenic cell death in cancer and infectious disease*. *Nature Reviews Immunology*, 2017. **17**(2): p. 97-111.
- [41] Li, H.J., et al., *Multichannel ballistic transport in multiwall carbon nanotubes*. *Physical review letters*, 2005. **95**(8): p. 086601.
- [42] Ba, L., et al., *Probing local electric field distribution of nanotube arrays using electrostatic force microscopy*. *Journal of Applied Physics*, 2003. **93**(12): p. 9977-9982.
- [43] Yantzi, J. and J.T. Yeow. *Carbon nanotube enhanced pulsed electric field electroporation for biomedical applications*. in *IEEE International Conference Mechatronics and Automation, 2005*. 2005. IEEE.
- [44] Lopez, C.F., et al., *Understanding nature's design for a nanosyringe*. *Proceedings of the National Academy of Sciences*, 2004. **101**(13): p. 4431-4434.
- [45] Asadipour, K., et al., *Ultra-Low Intensity Post-Pulse Affects Cellular Responses Caused by Nanosecond Pulsed Electric Fields*. *Bioengineering*, 2023. **10**(9): p. 1069.
- [46] Romeo, S., et al., *Modified Blumlein pulse-forming networks for bioelectrical applications*. *The Journal of Membrane Biology*, 2010. **236**: p. 55-60.
- [47] Sun, Y., et al., *Compact, nanosecond, high repetition rate, pulse generator for bioelectric studies*. *IEEE Transactions on Dielectrics and Electrical Insulation*, 2007. **14**(4): p. 863-870.
- [48] Kanaan, M., et al., *Characterization of a 50-  $\Omega$  exposure setup for high-voltage nanosecond pulsed electric field bioexperiments*. *IEEE Trans Biomed Eng*, 2011. **58**(1): p. 207-14.
- [49] Xiao, S., et al., *Nanosecond bipolar pulse generators for bioelectrics*. *Bioelectrochemistry*, 2018. **123**: p. 77-87.
- [50] Ma, J., et al. *High Voltage Nanosecond Pulse Generator based on Inductive Energy Storage With Adjustable Pulse Width*. in *2022 IEEE International Conference on High Voltage Engineering and Applications (ICHVE)*. 2022.
- [51] Butkus, P., et al. *Concepts and Capabilities of In-House Built Nanosecond Pulsed Electric Field (nsPEF) Generators for Electroporation: State of Art*. *Applied Sciences*, 2020. **10**, DOI: 10.3390/app10124244.
- [52] Merla, C., et al., *A 10- $\Omega$  High-Voltage Nanosecond Pulse Generator*. *IEEE Transactions on Microwave Theory and Techniques*, 2010. **58**(12): p. 4079-4085.
- [53] Kandratsyev, A., et al. *Four Channel 6.5 kV, 65 A, 100 ns–100  $\mu$ s Generator with Advanced Control of Pulse and Burst Protocols for Biomedical and Biotechnological Applications*. *Applied Sciences*, 2021. **11**, DOI: 10.3390/app112411782.
- [54] Garner, A.L., et al., *Design, characterization and experimental validation of a compact, flexible pulsed power architecture for ex vivo platelet activation*. *PLOS ONE*, 2017. **12**(7): p. e0181214.

- [55] Urabe, G., et al., *1.2 MV/cm pulsed electric fields promote transthyretin aggregate degradation*. Sci Rep, 2020. **10**(1): p. 12003.
- [56] Yao, C., et al., *A Novel Configuration of Modular Bipolar Pulse Generator Topology Based on Marx Generator With Double Power Charging*. IEEE Transactions on Plasma Science, 2016. **44**(10): p. 1872-1878.
- [57] Yao, C., et al., *FPGA-Controlled All-Solid-State Nanosecond Pulse Generator for Biological Applications*. IEEE Transactions on Plasma Science, 2012. **40**(10): p. 2366-2372.
- [58] Bagalkot, T.R., N. Leblanc, and G.L. Craviso, *Stimulation or Cancellation of Ca<sup>2+</sup> Influx by Bipolar Nanosecond Pulsed Electric Fields in Adrenal Chromaffin Cells Can Be Achieved by Tuning Pulse Waveform*. Scientific Reports, 2019. **9**(1): p. 11545.
- [59] Valdez, C.M., et al., *Asymmetrical bipolar nanosecond electric pulse widths modify bipolar cancellation*. Scientific Reports, 2017. **7**(1): p. 16372.
- [60] Hieda, I. and K.C. Nam, *Electric field measurement of the living human body for biomedical applications: Phase measurement of the electric field intensity*. International Journal of Antennas and Propagation, 2013. **2013**.
- [61] Lin, J.C., *Electromagnetic fields in biological systems*. 2012: Taylor & Francis.
- [62] Foulds, I. and A. Barker, *Human skin battery potentials and their possible role in wound healing*. British Journal of Dermatology, 1983. **109**(5): p. 515-522.
- [63] Pettine, K.A., R.M. Salib, and S.G. Walker, *External electrical stimulation and bracing for treatment of spondylolysis: a case report*. Spine, 1993. **18**(4): p. 436-439.
- [64] Hou, Z., D. Fu, and Q.-H. Qin, *An exponential law for stretching–relaxation properties of bone piezovoltages*. International journal of solids and structures, 2011. **48**(3-4): p. 603-610.
- [65] Love, M.R., et al., *Effects of electrical stimulation on cell proliferation and apoptosis*. Journal of cellular physiology, 2018. **233**(3): p. 1860-1876.
- [66] Szewczyk, P.K., et al., *Surface-potential-controlled cell proliferation and collagen mineralization on electrospun polyvinylidene fluoride (PVDF) fiber scaffolds for bone regeneration*. ACS Biomaterials Science & Engineering, 2018. **5**(2): p. 582-593.
- [67] Miller, J.F., W.J. Dower, and L.S. Tompkins, *High-voltage electroporation of bacteria: genetic transformation of Campylobacter jejuni with plasmid DNA*. Proceedings of the National Academy of Sciences, 1988. **85**(3): p. 856-860.
- [68] Das, R., et al., *Electrical stimulation for immune modulation in cancer treatments*. Frontiers in Bioengineering and Biotechnology, 2022. **9**: p. 795300.
- [69] Schoenbach, K.H., et al., *The effect of pulsed electric fields on biological cells: Experiments and applications*. IEEE transactions on plasma science, 1997. **25**(2): p. 284-292.
- [70] Kolb, J.F., S. Kono, and K.H. Schoenbach, *Nanosecond pulsed electric field generators for the study of subcellular effects*. Bioelectromagnetics, 2006. **27**(3): p. 172-187.
- [71] Nuccitelli, R., et al., *Nano-Pulse Stimulation is a physical modality that can trigger immunogenic tumor cell death*. Journal for immunotherapy of cancer, 2017. **5**(1): p. 1-13.
- [72] Chen, X., et al., *Long term survival of mice with hepatocellular carcinoma after pulse power ablation with nanosecond pulsed electric fields*. Technology in cancer research & treatment, 2012. **11**(1): p. 83-93.
- [73] Beebe, S.J., *Considering effects of nanosecond pulsed electric fields on proteins*. Bioelectrochemistry, 2015. **103**: p. 52-59.
- [74] Weaver, J.C. and Y.A. Chizmadzhev, *Theory of electroporation: a review*. Bioelectrochemistry and bioenergetics, 1996. **41**(2): p. 135-160.
- [75] Arena, C. and R. Davalos, *Advances in therapeutic electroporation to mitigate muscle contractions*. J Membr Sci Technol, 2012. **2**(10.4172): p. 2155-9589.1000.

- [76] Jiang, C., R.V. Davalos, and J.C. Bischof, *A review of basic to clinical studies of irreversible electroporation therapy*. IEEE Transactions on biomedical Engineering, 2014. **62**(1): p. 4-20.
- [77] Ball, C., K.R. Thomson, and H. Kavnoudias, *Irreversible electroporation: a new challenge in “out of operating theater” anesthesia*. Anesthesia & Analgesia, 2010. **110**(5): p. 1305-1309.
- [78] Županič, A., S. Ribarič, and D. Miklavčič, *Increasing the repetition frequency of electric pulse delivery reduces unpleasant sensations that occur in electrochemotherapy*. Neoplasma, 2007. **54**(3): p. 246-250.
- [79] Golberg, A. and B. Rubinsky, *Towards electroporation based treatment planning considering electric field induced muscle contractions*. Technology in cancer research & treatment, 2012. **11**(2): p. 189-201.
- [80] Yao, C., et al., *Bipolar microsecond pulses and insulated needle electrodes for reducing muscle contractions during irreversible electroporation*. IEEE Transactions on Biomedical Engineering, 2017. **64**(12): p. 2924-2937.
- [81] Dong, S., et al., *First human trial of high-frequency irreversible electroporation therapy for prostate cancer*. Technology in cancer research & treatment, 2018. **17**: p. 1533033818789692.
- [82] Latouche, E.L., et al., *High-frequency irreversible electroporation for intracranial meningioma: a feasibility study in a spontaneous canine tumor model*. Technology in cancer research & treatment, 2018. **17**: p. 1533033818785285.
- [83] Davalos, R.V., L. Mir, and B. Rubinsky, *Tissue ablation with irreversible electroporation*. Annals of biomedical engineering, 2005. **33**: p. 223-231.
- [84] Son, R.S., et al., *Basic features of a cell electroporation model: illustrative behavior for two very different pulses*. The Journal of membrane biology, 2014. **247**(12): p. 1209-1228.
- [85] Sözer, E.B., et al., *Analysis of electrostimulation and electroporation by high repetition rate bursts of nanosecond stimuli*. Bioelectrochemistry, 2021. **140**: p. 107811.
- [86] Berridge, M. and A. Tan, *Trans-plasma membrane electron transport: a cellular assay for NADH-and NADPH-oxidase based on extracellular, superoxide-mediated reduction of the sulfonated tetrazolium salt WST-1*. Protoplasma, 1998. **205**: p. 74-82.
- [87] Herst, P.M. and M.V. Berridge, *Plasma membrane electron transport: a new target for cancer drug development*. Current molecular medicine, 2006. **6**(8): p. 895-904.
- [88] Ly, J.D. and A. Lawen, *Transplasma membrane electron transport: enzymes involved and biological function*. Redox Rep, 2003. **8**(1): p. 3-21.
- [89] Pakhomov, A.G., et al., *Lipid nanopores can form a stable, ion channel-like conduction pathway in cell membrane*. Biochem Biophys Res Commun, 2009. **385**(2): p. 181-6.
- [90] Mattson, M.P., *Hormesis defined*. Ageing research reviews, 2008. **7**(1): p. 1-7.
- [91] Lawen, A., et al., *The universality of bioenergetic disease: the role of mitochondrial mutation and the putative inter-relationship between mitochondria and plasma membrane NADH oxidoreductase*. Molecular Aspects of Medicine, 1994. **15**: p. s13-s27.
- [92] Beebe, S.J., B.P. Lassiter, and S. Guo, *Nanopulse Stimulation (NPS) Induces Tumor Ablation and Immunity in Orthotopic 4T1 Mouse Breast Cancer: A Review*. Cancers (Basel), 2018. **10**(4).
- [93] Lassiter, B.P., S. Guo, and S.J. Beebe, *Nano-Pulse Stimulation Ablates Orthotopic Rat Hepatocellular Carcinoma and Induces Innate and Adaptive Memory Immune Mechanisms that Prevent Recurrence*. Cancers (Basel), 2018. **10**(3).
- [94] Bernardi, P., et al., *The Mitochondrial Permeability Transition Pore: Channel Formation by F-ATP Synthase, Integration in Signal Transduction, and Role in Pathophysiology*. Physiological Reviews, 2015. **95**(4): p. 1111-1155.

- [95] Bonora, M. and P. Pinton, *The Mitochondrial Permeability Transition Pore and Cancer: Molecular Mechanisms Involved in Cell Death*. *Frontiers in Oncology*, 2014. **4**.
- [96] Giorgio, V., et al., *Ca(2+) binding to F-ATP synthase  $\beta$  subunit triggers the mitochondrial permeability transition*. *EMBO Rep*, 2017. **18**(7): p. 1065-1076.
- [97] Handy, D.E. and J. Loscalzo, *Redox regulation of mitochondrial function*. *Antioxid Redox Signal*, 2012. **16**(11): p. 1323-67.
- [98] Zoratti, M. and I. Szabò, *The mitochondrial permeability transition*. *Biochim Biophys Acta*, 1995. **1241**(2): p. 139-76.
- [99] Chernyak, B.V., *Redox regulation of the mitochondrial permeability transition pore*. *Biosci Rep*, 1997. **17**(3): p. 293-302.
- [100] Linard, D., et al., *Redox characterization of human cyclophilin D: identification of a new mammalian mitochondrial redox sensor?* *Arch Biochem Biophys*, 2009. **491**(1-2): p. 39-45.
- [101] Liu, S., et al., *p38MAPK inhibition attenuates LPS-induced acute lung injury involvement of NF-kappaB pathway*. *Eur J Pharmacol*, 2008. **584**(1): p. 159-65.
- [102] Marchetti, P., et al., *Mitochondrial spare respiratory capacity: mechanisms, regulation, and significance in non-transformed and cancer cells*. *The FASEB Journal*, 2020. **34**(10): p. 13106-13124.
- [103] Casciola, M., et al., *Cancellation of nerve excitation by the reversal of nanosecond stimulus polarity and its relevance to the gating time of sodium channels*. *Cellular and Molecular Life Sciences*, 2019. **76**: p. 4539-4550.
- [104] Valdez, C.M., et al., *Asymmetrical bipolar nanosecond electric pulse widths modify bipolar cancellation*. *Scientific Reports*, 2017. **7**(1): p. 16372.
- [105] Sadik, M.M., et al., *Scaling relationship and optimization of double-pulse electroporation*. *Biophysical journal*, 2014. **106**(4): p. 801-812.
- [106] Arena, C.B., et al., *Theoretical considerations of tissue electroporation with high-frequency bipolar pulses*. *IEEE Transactions on Biomedical Engineering*, 2010. **58**(5): p. 1474-1482.
- [107] Sano, M.B., et al., *Optimization of a single insertion electrode array for the creation of clinically relevant ablations using high-frequency irreversible electroporation*. *Computers in Biology and Medicine*, 2018. **95**: p. 107-117.
- [108] Boye, C., et al., *Gene electrotransfer of FGF2 enhances collagen scaffold biocompatibility*. *Bioelectrochemistry*, 2022. **144**: p. 107980.
- [109] Schadendorf, D., et al., *Melanoma*. *The Lancet*, 2018. **392**(10151): p. 971-984.
- [110] Abd-Allah, G.M., et al., *miRNAs as potential game-changers in melanoma: a comprehensive review*. *Pathology-Research and Practice*, 2023: p. 154424.
- [111] Beebe, S.A., S.J. Beebe, and D.K. Ivy, *Communication: Principles for a lifetime*. 2016: Pearson.
- [112] Asadipour, K. and S.J. Beebe, *Intratumoral Immunotherapy with NanoPulse Stimulation and anti-PD-L1-Functionalized Carbon Nanotubes in B16f10 Melanoma*. 2021.
- [113] Rojas-Chapana, J.A., et al., *Enhanced introduction of gold nanoparticles into vital acidithiobacillus ferrooxidans by carbon nanotube-based microwave electroporation*. *Nano Letters*, 2004. **4**(5): p. 985-988.
- [114] Raffa, V., et al., *Carbon nanotube-enhanced cell electropermeabilisation*. *Bioelectrochemistry*, 2010. **79**(1): p. 136-141.
- [115] Stacey, M., et al., *Nanosecond pulse electrical fields used in conjunction with multi-wall carbon nanotubes as a potential tumor treatment*. *Biomedical Materials*, 2011. **6**(1): p. 011002.
- [116] Smith, B.R., et al., *Selective uptake of single-walled carbon nanotubes by circulating monocytes for enhanced tumour delivery*. *Nature nanotechnology*, 2014. **9**(6): p. 481-487.

- [117] Hirsch, A., *The era of carbon allotropes*. Nature materials, 2010. **9**(11): p. 868-871.
- [118] Kroto, H.W., et al., *C 60: buckminsterfullerene*. nature, 1985. **318**(6042): p. 162-163.
- [119] Novoselov, K.S., et al., *Electric field effect in atomically thin carbon films*. science, 2004. **306**(5696): p. 666-669.
- [120] Iijima, S., *Helical microtubules of graphitic carbon*. nature, 1991. **354**(6348): p. 56-58.
- [121] Thostenson, E.T., Z. Ren, and T.-W. Chou, *Advances in the science and technology of carbon nanotubes and their composites: a review*. Composites science and technology, 2001. **61**(13): p. 1899-1912.
- [122] Singh, P., et al., *Organic functionalisation and characterisation of single-walled carbon nanotubes*. Chemical Society Reviews, 2009. **38**(8): p. 2214-2230.
- [123] Tasis, D., et al., *Chemistry of carbon nanotubes*. Chemical reviews, 2006. **106**(3): p. 1105-1136.
- [124] Kafa, H., et al., *Translocation of LRP1 targeted carbon nanotubes of different diameters across the blood-brain barrier in vitro and in vivo*. Journal of Controlled Release, 2016. **225**: p. 217-229.
- [125] Rubio, N., et al., *Multiphoton luminescence imaging of chemically functionalized multi-walled carbon nanotubes in cells and solid tumors*. Chemical Communications, 2015. **51**(45): p. 9366-9369.
- [126] Summers, H., et al., *Spatially-resolved profiling of carbon nanotube uptake across cell lines*. Nanoscale, 2017. **9**(20): p. 6800-6807.
- [127] Cherukuri, P., et al., *Near-infrared fluorescence microscopy of single-walled carbon nanotubes in phagocytic cells*. Journal of the American Chemical Society, 2004. **126**(48): p. 15638-15639.
- [128] Pantarotto, D., et al., *Translocation of bioactive peptides across cell membranes by carbon nanotubes*. Chemical Communications, 2004(1): p. 16-17.
- [129] Kostarelos, K., et al., *Cellular uptake of functionalized carbon nanotubes is independent of functional group and cell type*. Nature nanotechnology, 2007. **2**(2): p. 108-113.
- [130] Mu, Q., D.L. Broughton, and B. Yan, *Endosomal leakage and nuclear translocation of multiwalled carbon nanotubes: developing a model for cell uptake*. Nano letters, 2009. **9**(12): p. 4370-4375.
- [131] Tschopp, J. and K. Schroder, *NLRP3 inflammasome activation: The convergence of multiple signalling pathways on ROS production?* Nature reviews immunology, 2010. **10**(3): p. 210-215.
- [132] He, Y., H. Hara, and G. Núñez, *Mechanism and regulation of NLRP3 inflammasome activation*. Trends in biochemical sciences, 2016. **41**(12): p. 1012-1021.
- [133] Cui, D., et al., *Effect of single wall carbon nanotubes on human HEK293 cells*. Toxicology letters, 2005. **155**(1): p. 73-85.
- [134] Rotoli, B.M., et al., *Non-functionalized multi-walled carbon nanotubes alter the paracellular permeability of human airway epithelial cells*. Toxicology letters, 2008. **178**(2): p. 95-102.
- [135] Hou, P.-X., C. Liu, and H.-M. Cheng, *Purification of carbon nanotubes*. carbon, 2008. **46**(15): p. 2003-2025.
- [136] Coccini, T., et al., *Effects of water-soluble functionalized multi-walled carbon nanotubes examined by different cytotoxicity methods in human astrocyte D384 and lung A549 cells*. Toxicology, 2010. **269**(1): p. 41-53.
- [137] Vuković, G., et al., *Synthesis, characterization and cytotoxicity of surface amino-functionalized water-dispersible multi-walled carbon nanotubes*. Applied Surface Science, 2009. **255**(18): p. 8067-8075.

- [138] Zhang, L.W., et al., *Biological interactions of functionalized single-wall carbon nanotubes in human epidermal keratinocytes*. International Journal of Toxicology, 2007. **26**(2): p. 103-113.
- [139] Li, R., et al., *Surface charge and cellular processing of covalently functionalized multiwall carbon nanotubes determine pulmonary toxicity*. ACS nano, 2013. **7**(3): p. 2352-2368.
- [140] Porter, A.E., et al., *Uptake of noncytotoxic acid-treated single-walled carbon nanotubes into the cytoplasm of human macrophage cells*. ACS Nano, 2009. **3**(6): p. 1485-1492.
- [141] Kagan, V., et al., *Direct and indirect effects of single walled carbon nanotubes on RAW 264.7 macrophages: role of iron*. Toxicology letters, 2006. **165**(1): p. 88-100.
- [142] Pulskamp, K., S. Diabaté, and H.F. Krug, *Carbon nanotubes show no sign of acute toxicity but induce intracellular reactive oxygen species in dependence on contaminants*. Toxicology letters, 2007. **168**(1): p. 58-74.
- [143] Palomaki, J., et al., *Long, needle-like carbon nanotubes and asbestos activate the NLRP3 inflammasome through a similar mechanism*. ACS nano, 2011. **5**(9): p. 6861-6870.
- [144] Wang, J., et al., *Multi-walled carbon nanotubes do not impair immune functions of dendritic cells*. Carbon, 2009. **47**(7): p. 1752-1760.
- [145] Dumortier, H., et al., *Functionalized carbon nanotubes are non-cytotoxic and preserve the functionality of primary immune cells*. Nano letters, 2006. **6**(7): p. 1522-1528.
- [146] Pescatori, M., et al., *Functionalized carbon nanotubes as immunomodulator systems*. Biomaterials, 2013. **34**(18): p. 4395-4403.
- [147] Medepalli, K., et al., *Evaluation of the direct and indirect response of blood leukocytes to carbon nanotubes (CNTs)*. Nanomedicine: Nanotechnology, Biology and Medicine, 2011. **7**(6): p. 983-991.
- [148] Yang, S.-t., et al., *Biodistribution of pristine single-walled carbon nanotubes in vivo*. The Journal of Physical Chemistry C, 2007. **111**(48): p. 17761-17764.
- [149] Al-Jamal, K.T., et al., *Degree of chemical functionalization of carbon nanotubes determines tissue distribution and excretion profile*. Angewandte Chemie, 2012. **124**(26): p. 6495-6499.
- [150] Liu, Z., et al., *Circulation and long-term fate of functionalized, biocompatible single-walled carbon nanotubes in mice probed by Raman spectroscopy*. Proceedings of the National Academy of Sciences, 2008. **105**(5): p. 1410-1415.
- [151] Schipper, M.L., et al., *A pilot toxicology study of single-walled carbon nanotubes in a small sample of mice*. Nature nanotechnology, 2008. **3**(4): p. 216-221.
- [152] Meng, J., et al., *Immune responses of BALB/c mice to subcutaneously injected multi-walled carbon nanotubes*. Nanotoxicology, 2011. **5**(4): p. 583-591.
- [153] Schoenbach, K.H., et al., *A scaling law for membrane permeabilization with nanopulses*. IEEE Transactions on Dielectrics and Electrical Insulation, 2009. **16**(5): p. 1224-1235.
- [154] Hirano, S., S. Kanno, and A. Furuyama, *Multi-walled carbon nanotubes injure the plasma membrane of macrophages*. Toxicology and applied pharmacology, 2008. **232**(2): p. 244-251.
- [155] Mi, Y., et al., *Multi-parametric study of the viability of in vitro skin cancer cells exposed to nanosecond pulsed electric fields combined with multi-walled carbon nanotubes*. Technology in cancer research & treatment, 2019. **18**: p. 1533033819876918.
- [156] An, K.H., et al., *High-capacitance supercapacitor using a nanocomposite electrode of single-walled carbon nanotube and polypyrrole*. Journal of the Electrochemical Society, 2002. **149**(8): p. A1058.
- [157] Liu, D., et al., *Magnetoporation and magnetolysis of cancer cells via carbon nanotubes induced by rotating magnetic fields*. Nano letters, 2012. **12**(10): p. 5117-5121.

- [158] Koratkar, N., et al., *Mobility of carbon nanotubes in high electric fields*. Journal of Nanoscience and Nanotechnology, 2004. **4**(1-2): p. 69-71.
- [159] van Berlo, D., et al., *Apoptotic, inflammatory, and fibrogenic effects of two different types of multi-walled carbon nanotubes in mouse lung*. Archives of toxicology, 2014. **88**: p. 1725-1737.
- [160] Mao, Z., et al., *Carbon Nanotubes Enabling Highly Efficient Cell Apoptosis by Low-Intensity Nanosecond Electric Pulses via Perturbing Calcium Handling*. Small, 2020. **16**(1): p. 1904047.
- [161] Nuccitelli, R., et al., *Nanosecond pulsed electric fields cause melanomas to self-destruct*. Biochemical and biophysical research communications, 2006. **343**(2): p. 351-360.
- [162] Beebe, S.J., et al., *Nanosecond, high-intensity pulsed electric fields induce apoptosis in human cells*. The FASEB journal, 2003. **17**(11): p. 1-23.
- [163] Ren, W., N.M. Sain, and S.J. Beebe, *Nanosecond pulsed electric fields (nsPEFs) activate intrinsic caspase-dependent and caspase-independent cell death in Jurkat cells*. Biochemical and biophysical research communications, 2012. **421**(4): p. 808-812.

## APPENDIX

### PERMISSIONS FOR REPRINTING PUBLISHED MATERIALS

| Chapter<br>Number | Journal             | License<br>Number | Date<br>Acquired | Reference                 |
|-------------------|---------------------|-------------------|------------------|---------------------------|
| 2                 | Bioengineering      | Public Domain     | 2023             | Asadipour<br>et al., 2023 |
| 2                 | Bioelectrochemistry | Public Domain     | 2024             | Asadipour<br>et al., 2024 |
| 3                 | ODU Digital Commons | Public Domain     | 2021             | Asadipour<br>et al., 2021 |
| 3                 | ODU Digital Commons | Public Domain     | 2023             | Asadipour<br>et al., 2023 |

**VITA**  
**KAMAL ASADIPOUR**

Kasad001@odu.edu

The Frank Reidy Research Center for Bioelectronics Old Dominion University  
Norfolk, VA 23508

**EDUCATION**

---

|   |                                     |
|---|-------------------------------------|
| <b>Old Dominion University</b><br>PhD, Biomedical Engineering         | <b>Norfolk, VA</b><br>December 2023 |
| <b>Semnan University</b><br>Master of Science, Biomedical Engineering | <b>Iran</b><br>December 2016        |
| <b>Azad University</b><br>Bachelor of Science, Biomedical Engineering | <b>Iran</b><br>May 2013             |

**PUBLICATIONS**

---

Zeinali et al. (2014). Regeneration of full-thickness skin defects using umbilical cord blood stem cells loaded into modified porous scaffolds. *Asaio Journal*, 60(1), 106-114.

**Asadipour** et al. (2019). Characterization and biological properties of a novel synthesized silicon-substituted hydroxyapatite derived from eggshell. *The International Journal of Artificial Organs*, 42(2), 95-108.

Boye et al. (2022). Gene electrotransfer of FGF2 enhances collagen scaffold biocompatibility. *Bioelectrochemistry*, 144, 107980.

**Asadipour** et al (2023). Ultra-Low Intensity Post-Pulse Affects Cellular Responses Caused by Nanosecond Pulsed Electric Fields. *Bioengineering*, 10(9), 1069.

**Asadipour** et. Al (2024). Nanosecond Pulsed Electric Fields (nsPEFs) Modulate Electron Transport in the Plasma Membrane and the Mitochondria. *Bioelectrochemistry*, 155, 108568.

**AWARDS**

---

Karl H. & Gisela M. Schoenbach Fellowship Award, Frank Reidy Research Center for Bioelectronics, Old Dominion University, 2023 (\$4000)

ECE Graduate Teaching Assistant Award, Electrical and Computer Engineering Department, Old Dominion University, 2022.